

Diploma Thesis

Electron Beam Welding Alloy 625

Author

Christopher Wiednig

Field of Study

Mechanical Engineering and Economic Science – Production Engineering

Supervisor

Dr. Master Coline Béal

Assoc.Prof. Dipl.-Ing. Dr.techn. Norbert Enzinger

Head of Institute

Univ.-Prof. Dipl.-Ing. Dr.techn. Ch. Sommitsch

Institute for Materials Science and Welding
Graz University of Technology, Austria

Graz, March 2013

ACKNOWLEDGEMENT

An dieser Stelle möchte ich mich bei allen bedanken, die mich bei der Erstellung meiner Diplomarbeit unterstützt haben.

Allen voran beim Institutsvorstand Univ.-Prof. Dipl.-Ing. Dr.techn. Christof Sommitsch, der mir meine Diplomarbeit am Institut für Werkstoffkunde und Schweißtechnik ermöglicht hat. Des Weiteren möchte mich auch bei Dipl. Ing. Dr. Claus Lochbichler von der voestalpine Gießerei Traisen bedanken, welcher mir neben dem gesamten Roh- und Probenmaterial auch seine fachliche Unterstützung zukommen ließ.

Besonderer Dank geht an meine beiden Betreuer Assoc.Prof. Dipl.-Ing. Dr.techn. Norbert Enzinger und Dr. Master Coline Béal. Sie haben durch die hervorragende Betreuung und die vielen fachlichen Diskussionen einen wesentlichen Anteil zur Entstehung dieser Arbeit beigetragen.

Ebenfalls bedanken möchte ich mich beim Laborpersonal des Institutes für die Unterstützung bei meiner Labortätigkeit. Die entspannte Atmosphäre hat mir die unzähligen Stunden der Probenpräparation sehr verkürzt.

Ich möchte mich auch bei allen weiteren Mitarbeiter des Institutes bedanken, die Ihr Interesse an meiner Arbeit gezeigt haben und mir mit Rat und Tat während meiner Arbeit zur Seite standen.

Abschließend möchte ich mich bei den beiden Menschen bedanken die mir dieses Studium überhaupt ermöglicht haben, meinen Eltern. Ohne Ihre Unterstützung und den Rückhalt den Sie mir speziell in schwierigen Zeiten meines Studiums gegeben haben, wäre dieses nicht möglich gewesen.

Christopher Wiednig

STATUTORY DECLARATION

I declare that I have authored this thesis independently, that I have not used other than the declared sources / resources and that I have explicitly marked all material which has been quoted either literally or by content from the used sources.

Graz,

.....

Christopher Wiednig

ABSTRACT

At the beginning of the 21st century, the United Nation finally decided that the concentration of greenhouse gases in the atmosphere must be regulated, to slow down global warming.

Concerning the annually growing worldwide energy demand, improving the thermal efficiency of fossil running power plants is a necessary step. To achieve this, an increase of the steam pressure and temperature is needed. Modern power plants operate way above the critical pressure of steam (typically around $T=600^{\circ}\text{C}$ and $p=26.5\text{MPa}$), which is a huge challenge for the used materials; today in power plant construction, 9-12% chromium martensitic steels are widely used. If steam temperatures rise there is no way around nickel based super alloys. Due to the extraordinary high price of those nickel based alloys, they are only used where it is absolutely necessary; in the areas subjected to high temperatures. Engineers, now have to face the problems of combining these materials.

The scope of this thesis was to ascertain the weldability of cast nickel based alloy 625 with cast martensitic 9% chromium steel COST CB2, using electron beam welding.

The EBW process parameters and their effect on the welding were investigated for both materials. Similar (A625) and dissimilar joint welding experiments with thick walled parts (50mm), were executed. Investigations on the microstructure were done using the light optical microscope and the scanning electron microscope. Additionally, mechanical tests (hardness-, tensile-, Charpy- and side bend test) were carried out to examine the strength of the joint.

Finally, a welding experiment, according to the standard preliminary welding procedure specification was performed. The testing of this specimen was done according to ÖNORM EN ISO 15614-1 and ÖNORM EN ISO 15614-11.

The welding experiments and the performed investigations showed that the electron beam welding is well suited for joining A625 similar and A625/CB2 dissimilar thick walled parts. All the tests carried out according to the welding procedure specification were passed.

KURZFASSUNG

Zu Beginn des 21. Jahrhunderts beschlossen die Vereinten Nationen, dass die Konzentration von Treibhausgasen in der Atmosphäre reguliert werden muss um eine Verlangsamung der globalen Erwärmung zu bewirken.

Aufgrund des, jährlich steigenden, weltweiten Energiebedarfs, ist die Verbesserung des thermischen Wirkungsgrades fossiler Kraftwerke ein wichtiger Schritt dahin. Diese kann durch eine Erhöhung des Dampfdruckes und der Temperatur bewirkt werden. Da moderne Kraftwerke weit über dem kritischen Dampfdruck (typischerweise um $T=600^{\circ}\text{C}$ und $p=26.5\text{MPa}$) arbeiten, ist dies eine große Herausforderung für die verwendeten Materialien. Heute sind martensitische 9-12% Chrom Stähle im Kraftwerksbau weit verbreitet. Bei weiter gesteigerten Dampftemperaturen führt aber kein Weg an Nickel-Basis-Superlegierungen vorbei. Aufgrund des hohen Preises dieser Legierungen wird diese nur dort eingesetzt wo sie, aufgrund der dort vorherrschenden hohen Temperaturen, unbedingt notwendig sind. Ingenieure, müssen sich jetzt den Problemen der Verbindung dieser Materialien stellen.

In dieser Diplomarbeit wurde die Schweißeignung der Gusswerkstoffe aus Nickel-Basis-Legierung A625 mit martensitischem 9% Chromstahl COST CB2, mittels Elektronenstrahlschweißen untersucht.

Die benötigten Prozessparameter für das Elektronenstrahlschweißen der beiden Materialien wurde ermittelt, sowie der Effekt dieser Parameter auf die Schweißnaht. Es wurden artgleiche (A625) und artfremde Schweißungen dickwandiger Teile durchgeführt. Die Untersuchung der Mikrostruktur der Schweißnaht erfolgte mittels Lichtmikroskop und Rasterelektronenmikroskop. Zusätzlich wurden mechanische Tests (Härte-, Zug-, Kerbschlag- und Seitenbiegeprüfung) durchgeführt, um die Festigkeit und Zähigkeit der Verbindung zu untersuchen.

Letztlich wurde eine vollständige Verfahrensprüfung, in Anlehnung an die Norm für eine vorläufige Schweißanweisung (pWPS) ÖNORM EN ISO 15614-1 und ÖNORM EN ISO 15614-11 durchgeführt.

Die Experimente und die durchgeführten Untersuchungen zeigten, dass das Elektronenstrahlschweißen sich sehr gut zum Verbinden von A625 (artgleich) und A625/CB2 (artfremd) eignet. Alle Tests angelehnt an die pWPS Norm wurden bestanden.

TABLE OF CONTENT

ACKNOWLEDGEMENT	I
STATUTORY DECLARATION	II
ABSTRACT	III
KURZFASSUNG	IV
TABLE OF CONTENT	V
1 INTRODUCTION	1
1.1 BACKGROUND.....	1
1.2 GOALS.....	2
2 LITERATURE REVIEW	4
2.1 COST CB2 STEEL	4
2.2 NICKEL BASE ALLOY 625	5
2.3 ELECTRON BEAM WELDING.....	6
2.3.1 <i>History</i>	6
2.3.2 <i>Studies on EBW</i>	7
2.3.3 <i>Principle</i>	7
2.3.4 <i>Equipment</i>	9
2.3.5 <i>Beam Generation</i>	10
2.3.6 <i>Process Parameter</i>	13
2.3.7 <i>Deep Welding Effect</i>	17
2.3.8 <i>Seam Properties</i>	20
2.3.9 <i>Weld Preparation</i>	20
2.3.10 <i>Special Welding Procedures</i>	21
2.3.11 <i>Thick Walled Welding</i>	24
2.3.12 <i>Dissimilar Welding</i>	25
2.4 DESIGN OF EXPERIMENTS (DOE)	26
3 METHODS	31
3.1 MATERIALS.....	33
3.1.1 <i>CB2</i>	33
3.1.2 <i>A625</i>	34
3.2 EBW MACHINE	35
3.3 PARAMETER SELECTION	36
3.4 BLIND WELDING.....	36
3.4.1 <i>Pilot Study</i>	37
3.4.2 <i>Temperature Measurement</i>	37
3.4.3 <i>Blind Welding CB2</i>	38
3.4.4 <i>Blind Welding A625</i>	39
3.5 JOINT WELDING	40
3.5.1 <i>Test Set-Up</i>	40
3.5.2 <i>Similar Welding A625</i>	40
3.5.3 <i>Dissimilar Welding A625 / CB2</i>	41

3.5.4	<i>EN Standard Welding Procedure Specification (WPS)</i>	41
3.5.5	<i>Post Weld Heat Treatment</i>	42
3.6	INVESTIGATIONS	42
3.6.1	<i>Test Organisation</i>	42
3.6.2	<i>Testing Specimens</i>	43
3.6.3	<i>Macroscopy</i>	45
3.6.4	<i>Microscopy</i>	45
3.6.5	<i>EDX Analysis</i>	47
3.6.6	<i>Hardness Test</i>	47
3.6.7	<i>Tensile Test</i>	47
3.6.8	<i>Charpy-V Test</i>	48
3.6.9	<i>Side Bending Test</i>	49
4	RESULTS & DISCUSSION	51
4.1	BLIND WELDING.....	51
4.1.1	<i>Pilot Study</i>	51
4.1.2	<i>Temperature Measurement</i>	53
4.1.3	<i>Blind Welding CB2</i>	53
4.1.4	<i>Blind Welding A625</i>	62
4.2	JOINT WELDING	66
4.2.1	<i>Similar Welding A625</i>	66
4.2.2	<i>Dissimilar Welding A625 / CB2</i>	72
4.2.3	<i>Standard Welding Procedure Specification (WPS)</i>	82
5	SUMMARY & CONCLUSION	88
5.1	SUMMARY.....	88
5.2	CONCLUSION	89
6	OUTLOOK	90
7	LIST OF FIGURES	91
8	LIST OF TABLES	96
9	LIST OF EQUATIONS	97
10	REFERENCES	98

1 INTRODUCTION

The first section of this thesis focuses on the background of the topic and leads to the issues behind this work. Moreover, the purpose and the goals of this thesis are presented.

1.1 BACKGROUND

2010 mankind set a new inglorious record: Energy-related carbon-dioxide (CO₂) emissions have reached 30.6 gigatonnes, the highest value in history. This was a 5% leap from the former record year from 2008 [1].

On December 11th in Cancun, Mexico, at the 2010 United Nations Climate Change Conference, the Cancun Agreements were signed. These agreements are a set of major decisions to take care of the global climate change. One important goal is limiting the global average temperature increase to 2°C. Consequently the concentration of greenhouse gases in the atmosphere must be regulated to about 450ppm of CO₂-equivalent. To reach this goal, the worldwide energy-related emissions in 2020 must not be higher than 32 gigatonnes. Thus, the universal emission over the next ten years emission must rise less in total than they did between 2009 and 2010 [1].

Improving the thermal efficiency of fossil running power plants is a necessary step in this direction. A proper way to increase the efficiency is to raise the steam parameters, temperature and pressure. Figure 1 shows how the efficiency is affected by the steam parameters.

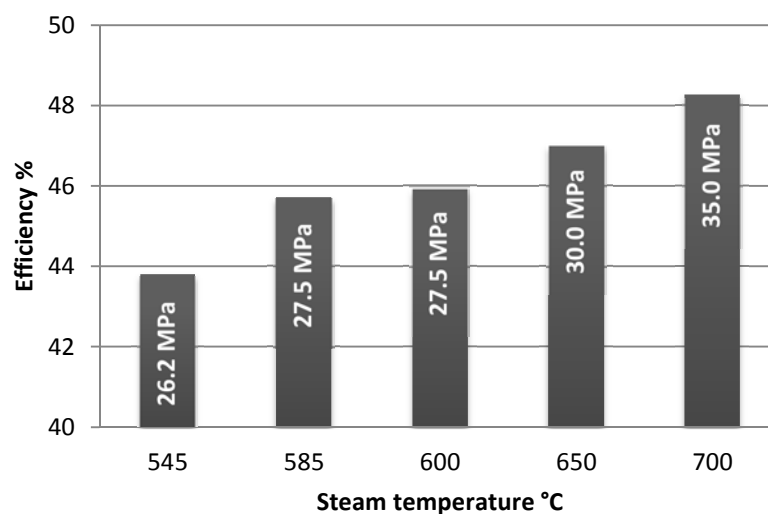


FIGURE 1: EFFICIENCY OVER TEMPERATURE [3]

Modern power plants operate above the critical pressure of steam ($T_c=374.12$ °C und $p_c=22.12$ MPa). The state of the art technology is called Ultra Supercritical (USC) steam power plant, with a live steam temperature of 600°C (28MPa) and reheat temperatures of 620°C. A further increase up to a live steam temperature of 700°C (35MPa) might be available around the year 2050 [2], [3]. By using additional optimization methods, a grade of efficiency over the 50% level can be achieved [4]. These high temperatures and high pressures present a massive challenge for the used materials. The key parameters in this issue are the oxidation and creep resistance.

Creep is the time dependent deformation of a material submitted to a constant load at a temperature above the recrystallization temperature [5]. Creep damage is irreversible and can lead to the fracture of the component.

$$T_{rc} = 0.4 \cdot T_m$$

Recrystallization temperature $[T_{Rxx}] = K$

Melting temperature $[T_m] = K$

EQUATION 1: RECRYSTALLISATION TEMPERATURE [6]

The required creep resistance for thermal power plants is defined with 100 MPa for at least 100,000 h. [6], [7].

Nowadays, in power plant construction, 9-12% chromium martensitic steels are widely used. These steels provide not only good tensile and creep strength, but also good corrosion resistance, high thermal conductivity and small thermal expansion [8]. 9-12% chromium steels can be used up to a temperature of 600°C. If steam temperatures rise, nickel base alloys are irreplaceable [9]. In addition to outstanding thermal-fatigue strength and good scaling resistance, nickel base alloys offer enhanced creep strength and oxidation resistance at high temperatures [10].

The main field of research in highly efficient thermal power plants is the material development and the application of these materials. Noteworthy current projects in this scope like the COMTE and the AD700 projects or the KW50+ and the MACPLUS project at the TU Graz [11].

1.2 GOALS

As mentioned before, there is no way around nickel super alloys in thermal power plant engineering, where temperatures are above 650°C. Because of the very high price of nickel based super-alloys, a considered use is recommended. Following the “right material for the right application” rule, designers have to combine the martensitic chromium steels and the nickel based alloys. Since welding is still the foremost way to join parts, welding technology faces a huge challenge which requires a lot of investigation in the area of dissimilar welding and thick walled welding. In Figure 2 a turbine design sample for a 700°C turbine [12], made out of martensitic chromium steel and nickel base alloy is shown.

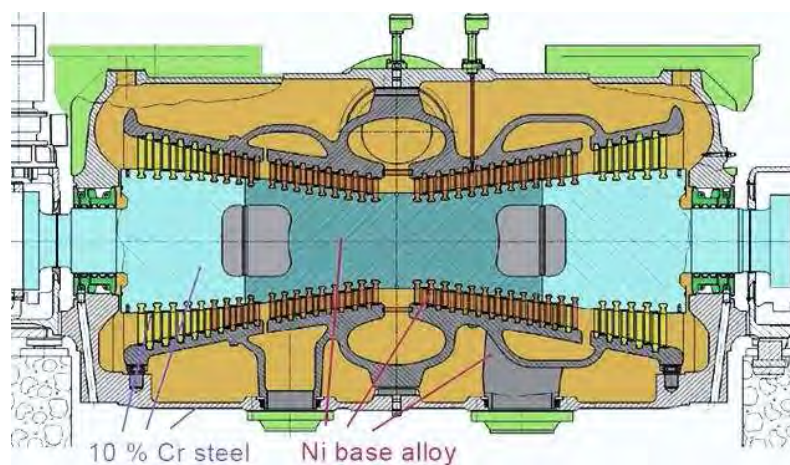


FIGURE 2: MATERIAL ARRANGEMENT FOR A 700°C TURBINE [12]

Electron beam Welding Alloy 625 is a continuation of the diploma thesis “*Dissimilar Schweißen von Guss-Stücken (Konstruktionsschweißungen) NIBAS 625 mit warmfestem Cr-Stahl COST CB2*“, written by Bernhard Berger [9]. He investigated joining between these two materials by manual arc welding (MAW) with rod electrodes, MIG welding and MAG welding. According to the European standard welding procedure qualification (WPQ), Bernhard Berger recommends the electrode welding. In this thesis, the joining by electron beam welding (EBW) of the nickel based alloy 625 and the martensitic 9% chromium steel COST CB2 is investigated. For this purpose, variation of EB welding parameters, metallography and mechanical testing are performed.

EBW is a not a very new technology, but its usage dropped after laser welding was invented and pushed. However, now this technology is coming back again (Ch. Sommitsch in [13]). It offers a lot of advantages, especially in seam geometry preparation and in welding time. In welded components beyond a thickness of 20mm, the slim geometry of the weld is impressive, as well as the welding time. Figure 3 shows a comparison between an EB seam and a stick-electrode weld seam [9] in a 50mm plate.



FIGURE 3: COMPARISON EBW TO MAW WITH ROD-ELECTRODE (50MM)

The main goal of this work is to find the required welding parameter for the COST CB2 steel and the nickel based alloy 625 and to set up a preliminary welding procedure specification (pWPS) according to the European standard EN ISO 15609-1. The final results of this thesis should be comparable with the results of Bernhard Berger to give a head to head comparison between the different welding technologies.

In cooperation with the *voest alpine Gießerei Traisen (VAGT)* and the *Institute for Materials Science and Welding (IWS)* of the *Graz University of Technology (TUG)*, this project was launched to make a feasibility study of similar (A625/A625) and dissimilar (A652/CB2) electron beam welding of thick walled parts (50mm). The material was supplied by the VAGT. Specimens were machined by the *Harald Umreich Ges.m.b.H.* and the VAGT; the electron beam welding, metallography and mechanical testing were carried out at the TUG.

2 LITERATURE REVIEW

This chapter provides a theoretical background. It is divided into the main areas this thesis is focused on. After an introduction about the investigated materials, the EBW process and its parameters are explained. Finally a short introduction of experimental design is given.

2.1 COST CB2 STEEL

Martensitic 9% chromium steels, as the COST CB2, belong to the most important materials used in steam and gas turbine technology. In addition to their combination of high strength and corrosion resistance, they also have a high thermal conductivity and a small thermal expansion. Other advantages are the economic benefits, such as the comparatively low cost, high availability, easy machining and good recyclability [8].

Steels based on 9 - 12% chromium are transformation hardened steels, which are tempered for service. The excellent combination of hardness and toughness is achieved through heat treatment. The latter contains solution annealing, quenching and tempering. A high density of dislocation and internal interfaces results from the martensitic transformation during cooling after the normalising treatment. During subsequent tempering, the carbon dissolved in the tetragonal distorted martensitic matrix precipitates as carbides ($M_{23}C_6$) or carbonitrides (MX) and the martensitic structure transforms into a ferritic structure. The resultant microstructure is a body-centered cubic matrix, with a dense distribution of different kinds of precipitates, a high density of internal boundaries and dislocations. The presence of different internal interfaces, such as prior austenite grain boundaries, block boundaries as well as precipitates, acting as barrier to dislocation motion contributes to the high hardening potential of such steels. Figure 4 schematically shows the microstructure of the CB2 in the “as received” condition [14].

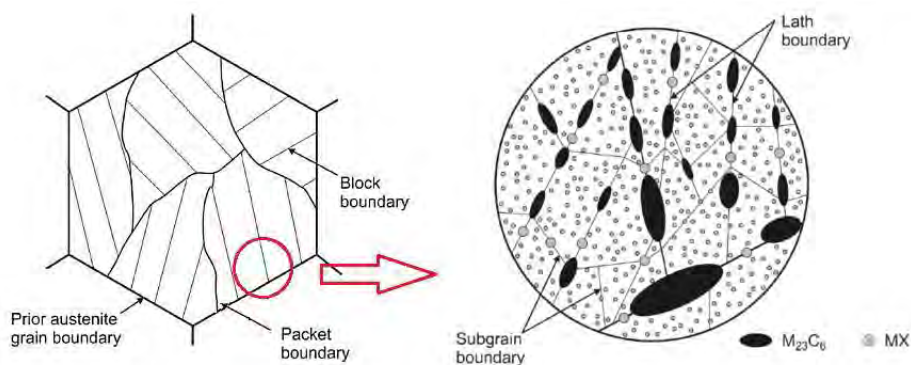


FIGURE 4: CB2 MICROSTRUCTURE [14]

2.1.1.1 $M_{23}C_6$ CARBIDES & MX CARBONITRIDES

These face-centered cubic $M_{23}C_6$ carbides, are the most common secondary phases in steels with high chromium content. They are generally located along boundaries. The MX carbon nitrides appear mostly as niobium-carbonitrides (Nb(C,N)) or vanadium-carbonitrides (V(C,N)). Due to their small size and their finely allocation the MX carbonitrides are mainly responsible for the creep resistance. Both, the $M_{23}C_6$ carbides and the MX carbonitrides contribute to the high strength and high creep resistance [9].

2.1.1.2 LAVES PHASE A2B & MODIFIED Z-PHASE Cr(V,Nb)N

The Laves phase, an intermetallic hexagonal structure $(\text{Fe,Cr})_2(\text{Mo,W})$, which appears after 1000-3000 hours, at temperatures between 500 and 700°C. It is assumed that due to the tendency of coarsening, the small particle population and the Mo and W depletion of the matrix, the creep resistance gets reduced [15]. The Cr(V,Nb)N phase is mainly responsible for the decline of creep strength in martensitic steels. Studies have shown that this phase grows into a few very large particles at the expense of MX particles. As a result, the latter can no longer contribute to precipitation strengthening [9].

2.1.1.3 WELDING

The optimized base material's microstructure and properties are completely changed within the weldment as a result of the welding cycle. The resulting microstructure and properties in the molten zone and in the heat affected zone (HAZ) are governed by the welding thermal cycle: pre-heat temperature, heating rate, peak temperature, cooling rate and post-weld heat treatment (PWHT). A decisive welding aspect is the width and the microstructure of the HAZ, the latter exhibiting a coarse grain zone and a fine-grained zone. Of particular interest in this work is the HAZ in the CB2 steel near the fusion line ($T_p \gg A_{C3}$). Precipitates which impede the grain growth at lower temperatures are dissolved and coarse austenite grains are formed. In 9-12% Cr steels, δ -ferrite grains can appear [9] and replace the austenite grains. Due to the rapid cooling process, the δ -ferrite remains stable down to room temperature. The coarse grain zone typically has the highest hardness and the lowest toughness [16].

It should be noted that for high temperature applications the fine grained HAZ ($T_p > A_{C3}$) is also crucial. This zone is considered the weakest link in welded joints in terms of creep resistance. Even at low stress and in short time many welds in creep-resistant martensitic steels fail in this area [16]. The most dominant failure mode of weldments in service is called Type IV cracking.

2.2 NICKEL BASE ALLOY 625

The Inconel 625 (A625) is a nickel-base superalloy with good mechanical properties, superior corrosion behavior and outstanding creep resistance. The microstructure of this material is cubic face centered and there are no phase transitions in the solid state. A625 is strengthened mainly by carbon, chromium, molybdenum and niobium. The high strength is achieved by solid solution hardening (Mo, Nb) and by precipitation hardening which is mainly derived from the metastable γ'' phase $[\text{Ni}_3(\text{Nb,Al,Ti})]$. Depending on the application of this material (high corrosion resistance or high creep resistance) different heat treatments are performed. For high temperature applications ($T > 600^\circ\text{C}$), where higher strength and better creep properties are required, the material is solution annealed at 1120°C to form $\text{Ni}_3(\text{Nb,Mo})$ phases [10],[17] & [18].

2.2.1.1 γ' -PHASE

This intermetallic phase (Ni_3Al) is present in many nickel base alloys and is used as precipitation hardener. In the A625 the γ' -Phase takes a minor role, since the Al and Ti contents are low and the A625 tends to form the Nb-rich γ'' -phase [9].

2.2.1.2 γ'' & δ -PHASE

This γ'' body-centred tetragonal phase (Ni_3Nb) is metastable; it begins to dissolve at more than 650°C. The precipitation kinetic of this phase is very slow, and results in a better weldability and a

higher resistance against strain-age cracking during heat treatment. After some time it is transformed into the stable, orthorhombic ordered δ -phase. The δ -phase is undesirable because it is incoherent with the Ni matrix and therefore not an effective strengthener. In addition, it leads to embrittlement. This behavior results in a reduced creep resistance [9], [19].

Various applications of nickel alloys are based on the various characteristics of the main element nickel. Widespread applications can be found in aeronautics, aerospace, marine, chemical and petrochemical industries and as well as in pressurized water reactors [18], [20].

2.2.1.3 MACHINING & WELDING

Due to the high ductility and work hardening of the A625, machining is costly. For machining, a low cutting speed and a low feed should be selected; an adequate machining depth is important in order to undercut the work hardened zone [18].

Precipitation hardened nickel-base super alloys tend by usage of conventional welding processes to hot cracking, because of the formation of eutectics. Furthermore, the creep resistance of these alloys decreases when the welding process leads to a reduction in grain size. The rapid temperature cycle and the low heat input during EBW counteract here [21]. Because there is no phase transformation in the solid state, there is only grain growth to be expected in the HAZ; starting from the melting zone, the grain size decreases continuously. Working with nickel requires a maximum of cleanliness; Sulphur (comprised in oil, grease, ...) can form the low melting Ni-Ni₃-S₂ eutectic (melting temperature 637°C) [9],[18].

2.3 ELECTRON BEAM WELDING

According to *OENORM EN ISO 40 63:2000 "Welding and allied processes"*; electron beam welding belongs to the beam welding group.

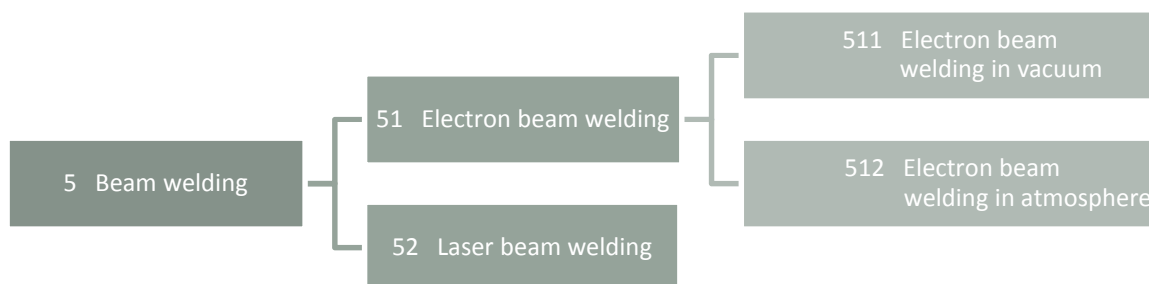


FIGURE 5: REFERENCE NUMBERS OF WELDING PROCESSES, ISO 40 63

2.3.1 HISTORY

This part refers to *"An International History of Electron Beam Welding"* by Dietrich von Dobeneck [22]. Other references are indicated separately.

Electron beams apply the principles of electro-optics, which have been well defined and explored since the beginning of 1920s. The use of electron beams in welding was discovered a few decades later by Dr. **Karl-Heinz Steigerwald** and Dr. **Jacques-André Stohr**. They both worked independently on this topic. Steigerwald experimented with electron microscopes for the *Allgemeine Elektrizitäts-Gesellschaft* (AEG), a German producer of electrical equipment. He discovered the potential of electron microscopes for drilling and welding. Steigerwald found a solution and was

looking for applications. Jacques-André Stohr, who worked for *Commissariat à l'Energie Atomique* (CEA), on the other hand, had a problem to solve: the welding of reactive materials. He discovered the use of electron beams in welding accidentally during manipulations on X-ray tubes.

In Germany AEG considered this technique uninteresting. Fortunately the American patent broker, Mr. Irving Rossi, realised the potential of this technology and funded Steigerwalds research. In 1952 he built the first electron beam machine. Finally, in **1958**, the first deep penetration welds, in a zircaloy plate, were performed [23]!

The availability of capital in nuclear- and aerospace industries in the early 1960's was of essential importance for the development of this technology. Just shortly after the spadework of Steigerwald, electron beam welding started to be used as an industrial process [21]:

- welding of synchronizing rings to gears; Volkswagen (1961)
- welding of artificial hip joint (1963)
- welding of water-cooled aluminum pistons for car engines (1969)
- ...

2.3.2 STUDIES ON EBW

Since the rise of EBW, a lot of research had been done. Till the 1980's the focus was based on the process itself and on applications up to 50mm welding depth. After the 1980's, the interest was shifted to thick walled welding, especially in the field of power plants, chemical plants and vessel construction. Unfortunately, most of these researches focused on specific applications and less on the welding procedure itself. So the results (including the welding parameters used on one machine and the analysis of the weld) cannot be transferred easily to other machines, materials or applications [24]. The key issue is that the "welding tool", the electron beam and its direct environment during welding can be barely examined. The knowledge of the movements of the melting pool in the keyhole is mainly based on mathematical models (see [19], [25–27]).

2.3.3 PRINCIPLE

Electron beam welding is a fusion welding process. The heating source in EBW is the kinetic energy of electrons which are shot on the workpiece. Electrons are, as protons and neutrons, elementary particles of matter. Electrons occur bonded to an atomic nucleus, as free charge carrier in a metallic lattice or as free electrons in vacuum. They have the mass of $9.1 \cdot 10^{-28}$ gram and carry a negative electric charge of $1.6021 \cdot 10^{-19}$ coulomb. Because of their electric charge, the electrons can be accelerated by an electric field (\vec{E}) and their orbit can be controlled with magnetic fields (\vec{B}). The responsible force for acceleration is the Coulomb force while the Lorentz force affects the electrons while moving through a magnetic field. Figure 6 and Figure 7 show the orientation of the forces due to the magnetic and electric fields [28].

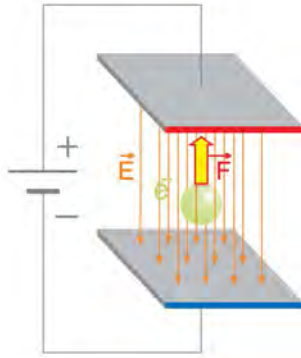


FIGURE 6: COULOMB FORCE [28]

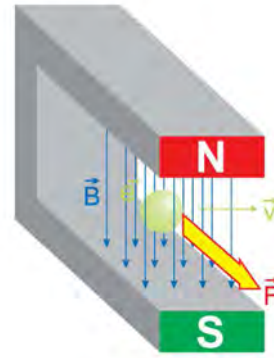


FIGURE 7: LORENTZ FORCE [28]

With an acceleration voltage of 150kV, electrons reach a speed of $2 \cdot 10^8$ mm/s, which is 70% of the speed of light. At this speed a relativistic mass increase of about 35% already occurs. This kinetic energy is usable for welding [29].

$$E = \frac{m \cdot v^2}{2}$$

$$\text{Energy } [E] = J = kg \cdot m^2 \cdot s^{-2}$$

$$\text{Mass } [m] = kg$$

$$\text{Velocity } [v] = m \cdot s^{-1}$$

EQUATION 2: KINETIC ENERGY

When hitting the metal surface, the electrons are decelerated during the first hundreds of a millimeter. Due to colliding with the orbital and the free electrons in the metal, the incoming electrons transfer their kinetic energy to the lattice atoms in the workpiece. The moving energy of the lattice atoms, which is coherent with the temperature, increases immediately. The material melts [29].

The penetration depth of the electrons depends on the acceleration voltage and on the density of the material. An approximate value is given by the equation of Schonland. The result specifies the distance in which the electrons lose 99% of their kinetic energy [30].

$$R_{pr} = 2.1 \cdot 10^{-2} \cdot \frac{U_B^2}{\rho}$$

$$\text{Penetration depth } [R_{pr}] = \mu m$$

$$\text{Acceleration voltage } [U_B] = kV$$

$$\text{Material density } [\rho] = \frac{kg}{dm^3}$$

EQUATION 3: SCHONLAND EQUATION

Not all electrons penetrate the material till this depth, some are backscattered directly and some diffuse out after penetrating [29]. The reflection reactions are shown in Figure 8.

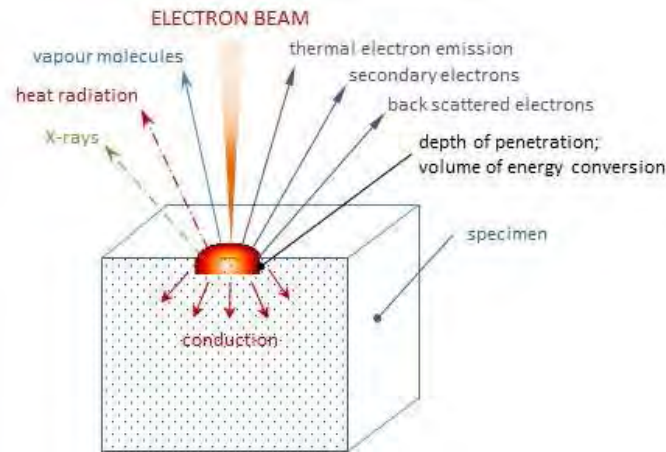


FIGURE 8: EB REFLECTION

Opportunately, the electron beam remains almost uninfluenced by metal vapor or plasma, compared to laser beam welding [31]. Furthermore, the grade of efficiency is much higher than with laser beam welding (Figure 9).

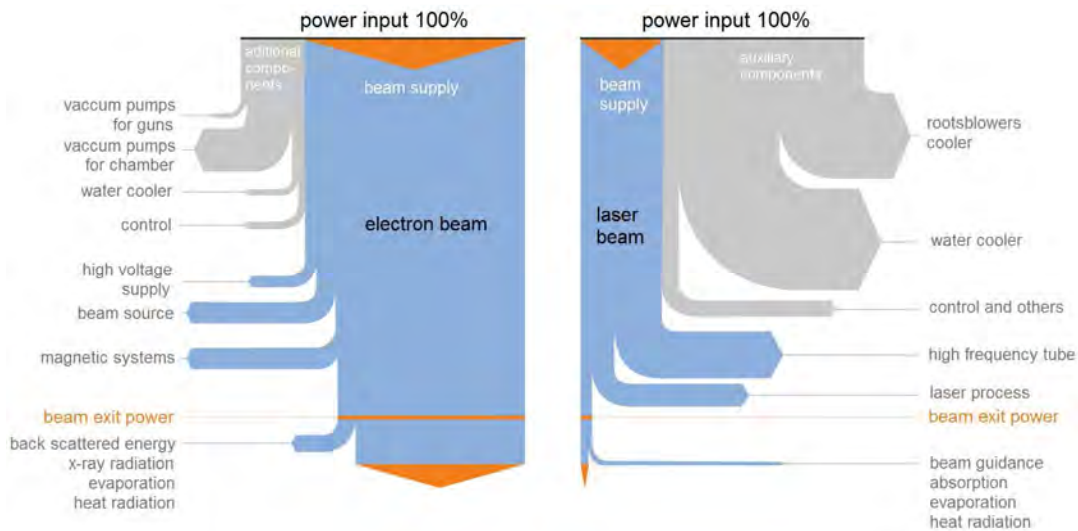


FIGURE 9: GRADE OF EFFICIENCY BEAM WELDING [28]

2.3.4 EQUIPMENT

All EBW systems are constructed of the same basic modules, as shown in the next figure [32].

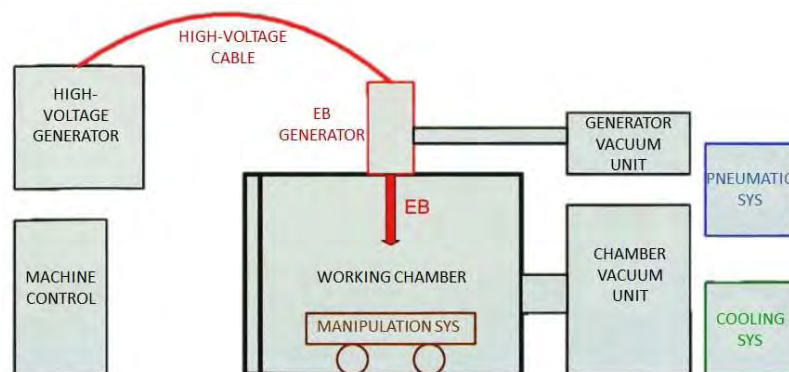


FIGURE 10: EBW MACHINE MODULES [31]

The **High-voltage generator** provides the electric power needed in the **EB generator** (or EB gun) to generate the electron beam. Moreover, the magnetic lenses for beam focusing, adjusting and deflecting are located inside the generator. The EB generator is separated from the **working chamber** by a valve. A constant high vacuum in the generator can be kept, while venting the working chamber. The **manipulation system** (e.g. rotary table) can perform a macroscopic movement of the work piece. The **generator vacuum unit** and the **chamber vacuum unit** contain several different vacuum pumps to create the required vacuum (generator $p_{\text{gen}} \approx 10^{-5}$ mbar; chamber $p_{\text{cham}} \approx 10^{-3}$ mbar). The **cooling system** regulates the temperature of the power components. The **pneumatic system** is needed for valve controlling. The functions of the whole system can be controlled and monitored by the **machine control**.

2.3.5 BEAM GENERATION

The beam generation takes place in the EB generator. Its main components are shown in Figure 11.

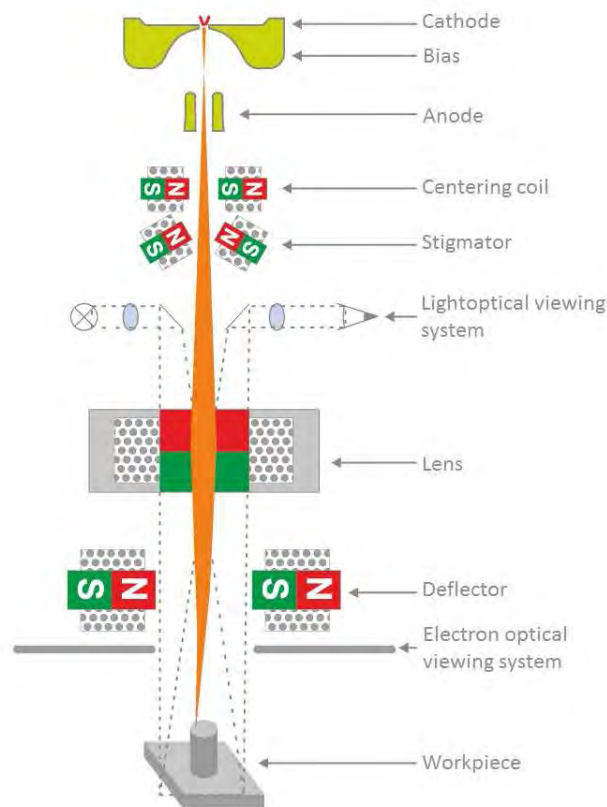


FIGURE 11: EB GENERATOR [28]

The **cathode** is the electron source. It is a flat ribbon filament usually made of tungsten; less common is lanthanum hexaboride (LaB6). By heating up the cathode, electrons gain enough energy to leave the material's surface. They gather around the filament and form an electron cloud. The number of the emitted electrons correlates with the temperature of the filament, as shown in Figure 12.

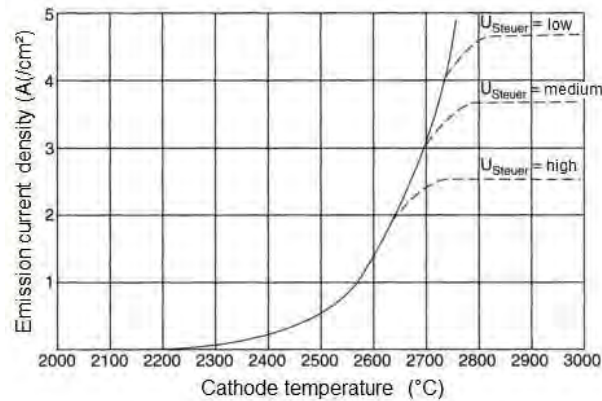


FIGURE 12: EMISSION CURRENT DENSITY OVER CATHOD TEMPERATUR [29]

The dashed lines represent the current density as a result of the auxiliary voltage (U_{Steuer}) of the **bias**. The bias (or Wehneltcylinder) is needed to control the beam current; a negative voltage in the bias reduces the beam current, the beam is pinched. By pinching the beam the bias also adjusts the location of the first real beam crossover. The position of the beam crossover is important for the divergence of the beam which influences the focal position (see 2.3.6.2 Focus) [29]. Figure 13 shows schematically the build-up of this so called triode system.

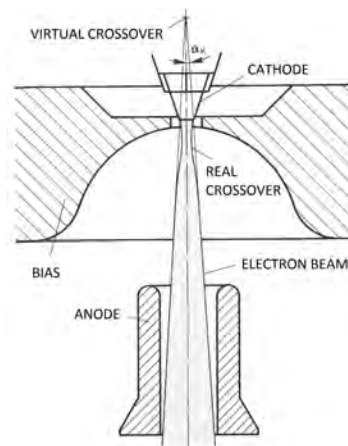


FIGURE 13: TRIODE SYSTEM [29]

The bottom part of the triode system is the **anode**. The anode is, contrary to the cathode, at ground potential. The electric field between these two components is responsible for the acceleration of the electrons. The acceleration voltage is constant during welding. The power of the beam is adjusted by the beam current, which is equivalent to the number of electrons in the beam in unit time. The following equations, taken from [33], explain the physical background of the beam energy.

$$\text{Electric charge } [Q] = C = As$$

$$\text{Elementary charge } e = 1.602177 \cdot 10^{-19} \text{ C}$$

$$\text{Number of electrons } n$$

$$Q = n \cdot e$$

EQUATION 4: ELECTRIC CHARGE [32]

$$I = \frac{Q}{t}$$

EQUATION 5: ELECTRIC CURRENT [32]

Current $[I] = A$

Time $[t] = s$

$$P = U \cdot I$$

EQUATION 6: ELECTRIC POWER [32]

Electric power $[P] = W = VA$

Voltage $[U] = V$

Behind the anode, a set of lenses is required to shape the electron beam and to position it accurately. This section in the EB gun is called beam optics. The magnetic lenses use the Lorentz force to manipulate the path of the electrons. The lenses consist of copper coil inside the iron pole pieces. The first lens is called **centering coil** (Figure 14). It is used to keep the electrons in the centre of the gun to minimise lens errors. The **stigmator** (Figure 15) controls the beam shape by correcting the stigmatism.

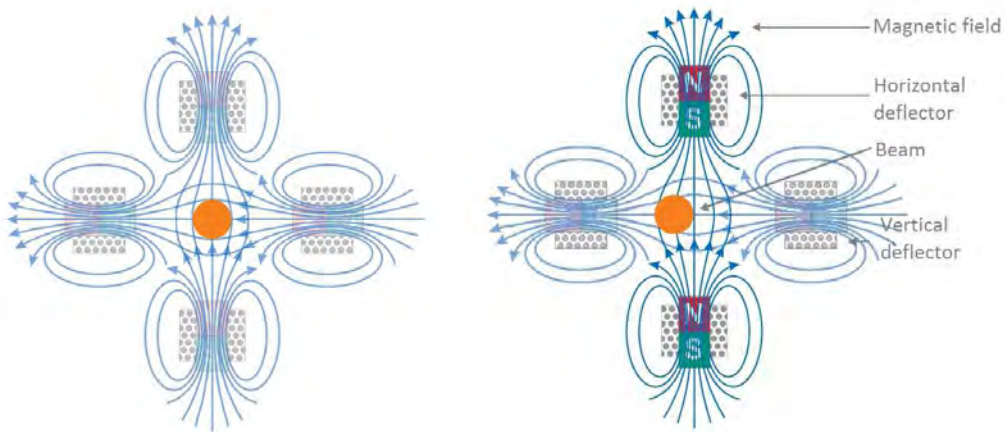


FIGURE 14: CENTERING COIL [28]

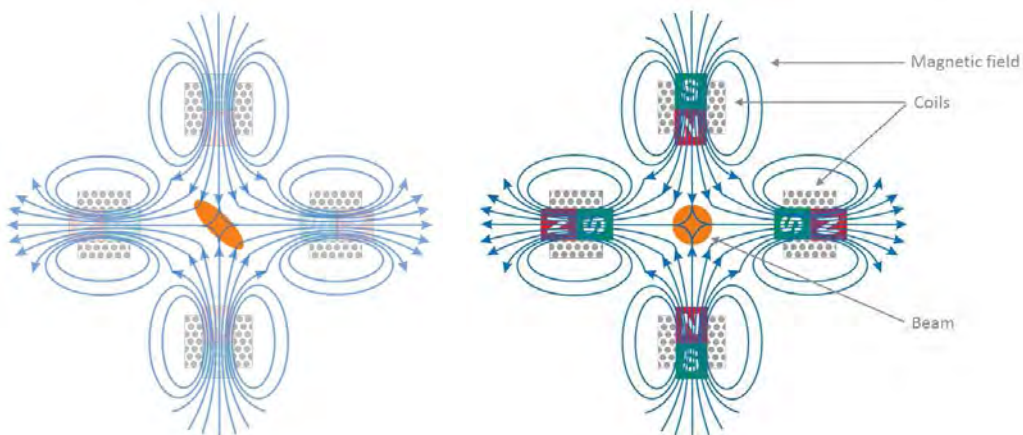


FIGURE 15: STIGMATOR [28]

The following **lens**, the focal lens, alters the focus of the beam, which is important to place the crossover in the right position related to the workpiece surface. Furthermore, the lens is responsible for the divergence of the beam; thereby also for the minimum beam diameter on the surface of the workpiece which is equal to beam intensity in this spot.

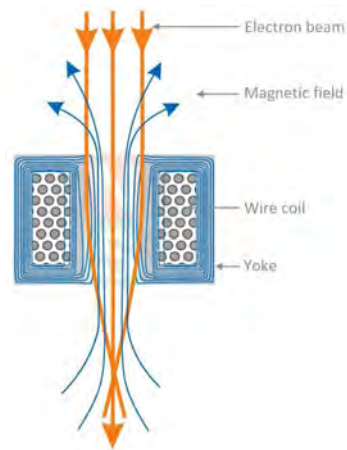


FIGURE 16: ELECTROMAGNETIC LENS [28]

Figure 17 shows the connection between the beam diameter (d_0), the divergence angle (θ_{full}) and the intensity of the beam.

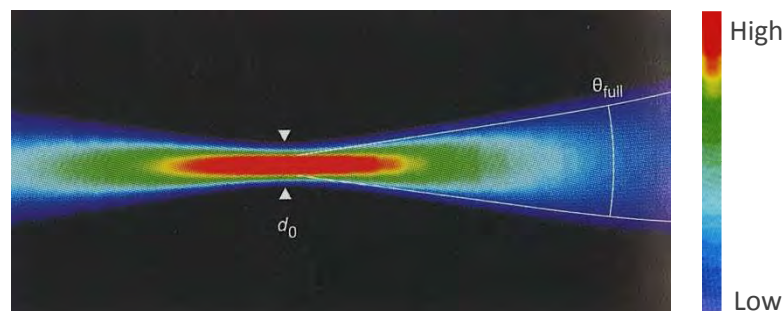


FIGURE 17: BEAM DENSITY [28]

The **deflector** is the bottom part of the EB generator. The working principle of this lens is equal to the centring coil. Beam deflection is performed to direct the beam across the work piece. Deflection can be done very rapidly because the beam has marginal inertia. Because of this, several special welding techniques can be applied (beam oscillation, simultaneous welding and beam wobbling (see 2.3.10)).

In addition to the beam optics a **light-optical viewing system** and an **electron-optical viewing system** are installed. Both systems are made for controlling the welding process. The light-optical system is a charge-coupled device (CCD) camera. The electron-optical system uses the backscattered electrons and the secondary electrons to create an image; the same principle as used in a scanning electron microscope (SEM).

2.3.6 PROCESS PARAMETER

An EBW unit offers a lot of parameters to adjust. The following sections list them and explain their influence on welding. Denomination and definition of the terms are taken from the *ÖNORM EN 1011-7* [34] and the *ÖNORM EN ISO 15609-3* [35] standards. The repeatability and stability of the process is very high due to the high level of machine controllability of the different processing parameters. Knowing the mentioned process parameters, welding experiments can be repeated exactly.

2.3.6.1 OPERATING DISTANCE

The distance (A_w) in millimetre between the surface of the workpiece and a fixed reference surface of the device with a defined distance from the focus-lens centre (see Figure 18).

Due to the convergence of the beam, the operating distance should be kept constant within an experiment to acquire comparable results.

2.3.6.2 FOCUS DISTANCE AND FOCAL POSITION

The distance (A_f) between the focus-lens and the focal point (d_0) of the beam.

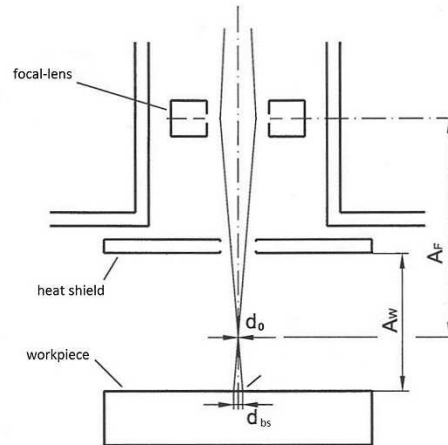


FIGURE 18: OPERATING DISTANCE & FOCAL POSITION [29]

The term focal position (u) is used to describe the position of the focal point of the beam (at d_0), related to the position of the work piece surface (Figure 19). The focal point position is given in milliamperes (mA). A negative value leads to a focal point below the surface and a positive value leads to a focal point above the surface. In both cases the diameter of the beam spot on the surface (d_{bs}) increases.

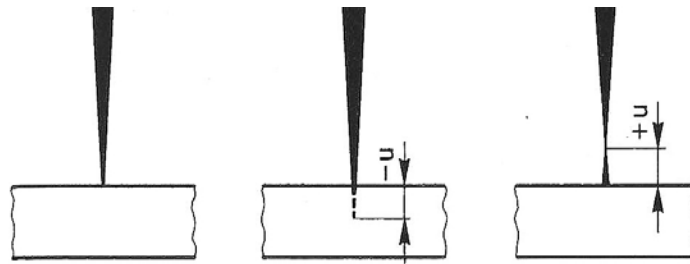


FIGURE 19: DIFFERENT FOCAL POSITIONS [29]

The focus has considerable influence on the forces in the melting pool (steam pressure). A not well chosen focal point leads to cavities in the seam and to undercuts on the seam top, due to process instabilities. For thin plates and for high welding speeds the focal position is not influencing the welding process significantly. But with increasing thickness of the working parts this parameter becomes more important. The following picture illustrates the influence of the focal position [24].

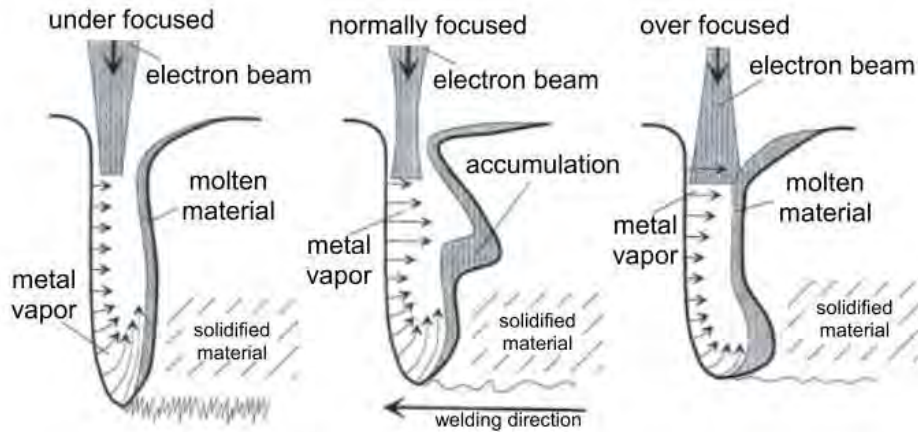


FIGURE 20: INFLUENCE OF FOCAL POSITION [19]

2.3.6.3 ACCELERATION VOLTAGE

The electric potential between the cathode and the anode in kilovolts (kV).

The accelerating voltage directly affects the speed of the electrons. It is an advantage to use a higher acceleration voltage and a low beam current to obtain a smaller beam spot diameter in the focal point. This setup is more tolerant to a change of the focal position and the machine adjustment is easier [29]. Usually an acceleration voltage of 60kV, 120kV or 150kV is used; up to 200kV is possible. The advantage of using an accelerating voltage below 60kV (low potential equipment) is that there is no need of a lead casing since below this voltage the x-ray radiation is negligible. Furthermore a cheaper design of the high voltage tank and the EB-gun is possible [29].

2.3.6.4 BEAM CURRENT

The value of the flow of the electric charge in the beam in mA.

The beam current combined with the accelerating voltage results the beam power and takes an essential influence on the welding result. The optimal beam current is responsible for a proper welding bead on both, face and root, sides of the welding [29]. For a smooth start and end of the welding, the beam current is gradually raised at the beginning of the welding and gradually reduced at the end of a welding. This is called “slope-in” and “slope-out”. Special attention to the slope-phase has to be paid in the case of radial welds [24].

2.3.6.5 LENS CURRENT

The current in the lens which is needed to focus the beam in mA.

2.3.6.6 BEAM OSCILLATION

Periodic deflection of the beam by electromagnetic forces. The parameters for beam oscillation are:

- Figure ... circle, parabola, fish, et al.
- Amplitude ... in X- and Y direction in mm
- Frequency ... how often the beam cycles the figure per second (Hz)
- Orientation ... of the profile in relation to the welding direction

The different beam figures are used to stabilize the keyhole during welding and to smooth the seam top. For stabilising the steam capillary, an enlargement of the effective area of the beam spot is performed. This is usually done by using a small circular figure with more than 100Hz. Thus, beam oscillation helps to avoid incomplete fusions, reduce porosity in alloys with a low melting point, reduce hardness in the fusion zone and allows the melting pool movement [24] [36]. It should be noted that the beam power has to be raised to reach the same welding depth with an oscillated beam as well as with a non-oscillated beam. The higher the amplitude, the higher the beam power must be.

Figure 21 and Figure 22 show, some different shapes which can be used for several purposes.

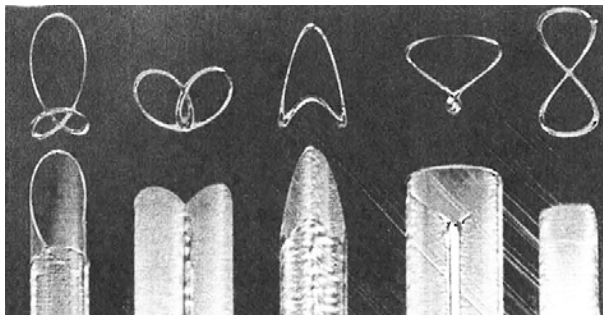


FIGURE 21: OSCILLATION FIGURES, TOP VIEW [40]

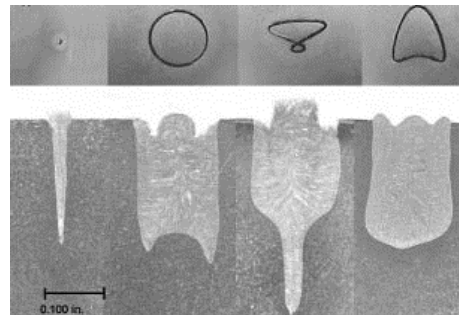


FIGURE 22: OSCILLATION FIGURES, SECTION VIEW [36]

2.3.6.7 BEAM PULSATION

Intentional, periodic variation of the beam current. The parameters for beam pulsation are:

- maximum beam current in mA
- minimum beam current in mA
- pulse frequency in Hz

2.3.6.8 WELDING SPEED

The relative velocity of the beam in relation to the work piece's surface in mm/s.

The welding speed defines together with the accelerating voltage and the beam current the energy per unit length. There is always an upper and a lower limit of the welding speed. The lower limit is set by the leakage of the melting pool on the root side of the seam. Above the upper speed limit porosities, cavities and cracks in the seam take place. The upper limit can be recognized by a very bumpy seam top with drops nearby [24].

The following diagram shows a rough guide for the recommended working speed as a function of seam thickness and beam power [29].

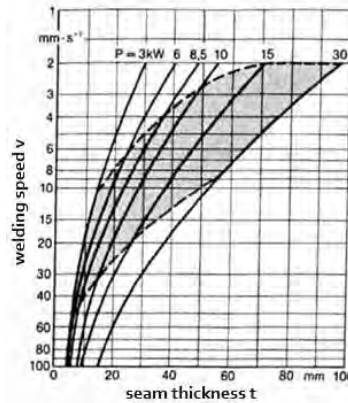


FIGURE 23: WELDING SPEED OVER SEAM THICKNESS [29]

2.3.6.9 WORKING PRESSURE

The pressure in the chamber during welding. It should be noted that welding parameters, determined at a certain pressure, are only reproducible at the same pressure level [37].

2.3.6.10 DIABEAM

All the parameters listed above are related to the machine and the welding settings. Besides, there are some parameters of the beam itself which are important to get a qualitative statement out of the welding results.

A pretty young system called DIABEAM, developed by the ISF-Welding Institute of Aachen University in Germany, takes care of the analysis and determination of the beam. The DIABEAM system is able to determine the beam geometry precisely, display the three dimensional power density distributions across the beam diameter and identifies variations caused by the cathode system or the vacuum. Moreover the focus curves can be evaluated, which describe the dependency of the working distance or the focus current and the beam diameter [38].

DIABEAM is used to ensure the quality of the beam and to document it. This is strongly required for three-dimensional contour and thick plate welding [38]. This system contains a sensor unit as well as a special computer hard and software [39].

2.3.7 DEEP WELDING EFFECT

The range of the power density of beam welding is a result of the option of focusing. Applications from heating up the material till a direct evaporation of the material can be carried out. Figure 24 relates the approximate power density values to the different effects in the material.

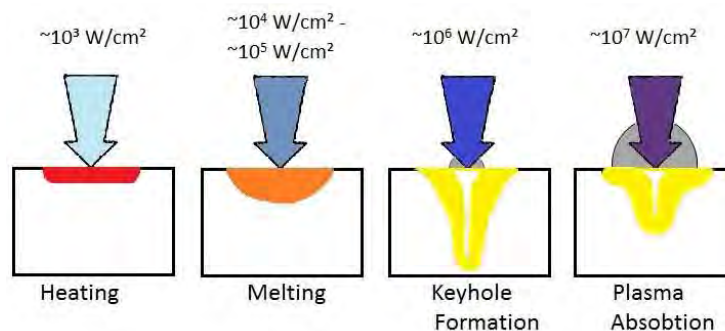


FIGURE 24: POWER DENSITY [19]

At a beam power density above 10^5 W/cm² in the beam spot, the **deep welding effect** occurs. Conduction of heat now is secondary; locally the material evaporates instantly. While creating a steam capillary (keyhole), surrounded by molten metal, the beam penetrates deeper into the material as illustrated in Figure 25 [37].

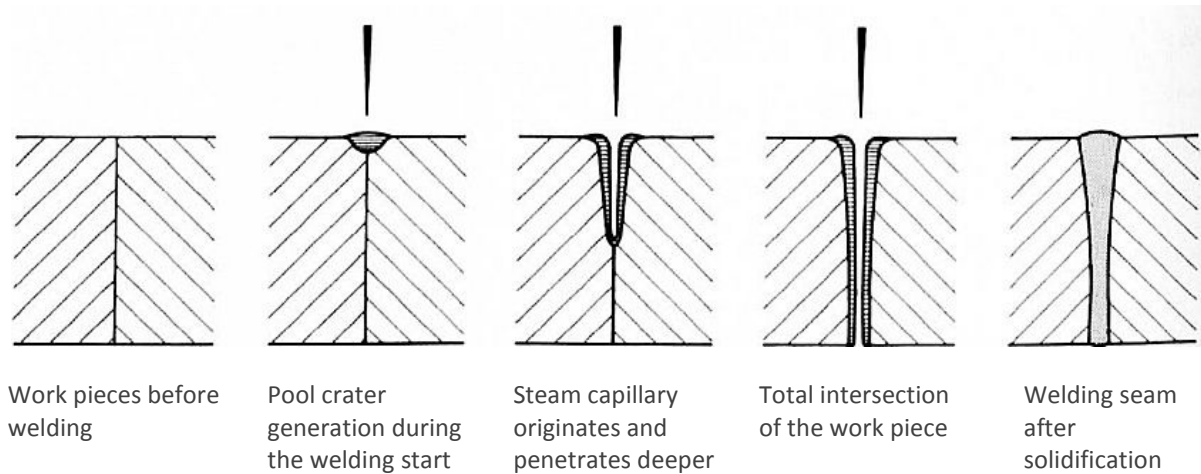


FIGURE 25: DEEP WELDING EFFECT [13]

The keyhole is filled with high-temperature metal-vapor phase surrounded with a metal-liquid phase. A thin liquid layer is formed in front of the keyhole wall and a rapid solidification region in the rear area of the keyhole with respect to the moving direction as well. Thus, by a relative movement between the workpiece and the electron beam, molten material from the beam front side flows around the capillary and solidifies on the back of it; the weld seam is formed. For deep-penetration welding on thick walled parts, the keyhole length is much larger than the keyhole radius [26]. The next two figures (Figure 26 and Figure 27) show a model of the moving keyhole as it is used for simulations [26], [27].

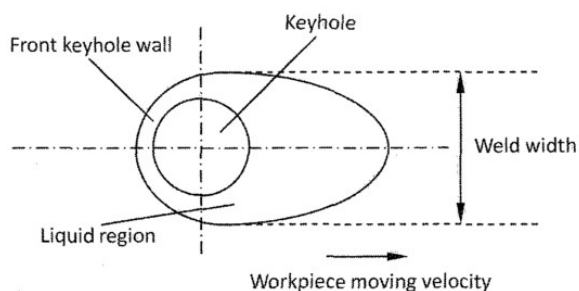


FIGURE 26: MOVING KEYHOLE, TOP VIEW [26]

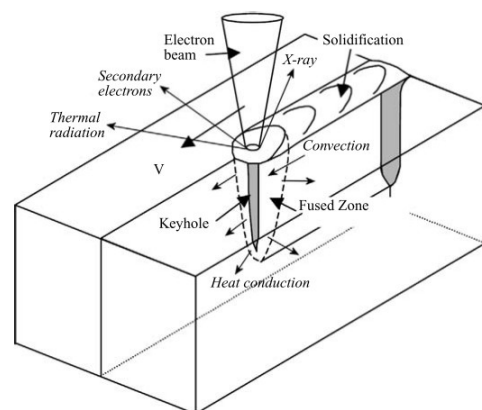


FIGURE 27: MOVING KEYHOLE, 3D [27]

For the welding process, the keyhole must not close! Several forces have to be in equilibrium; vapor pressure, gravity, capillary force, surface energy, hydrostatic pressure and friction forces act during welding (Figure 28). The vapor pressure must be sufficient; it is the primary force to keep the keyhole open. Furthermore, thermoelectric effects between two different materials or metal steam effects must be considered [19], [40]. Due to the complexity of this issue, here is referred to the works of Schultz [29], Luo [26] and Olshanskii [41].

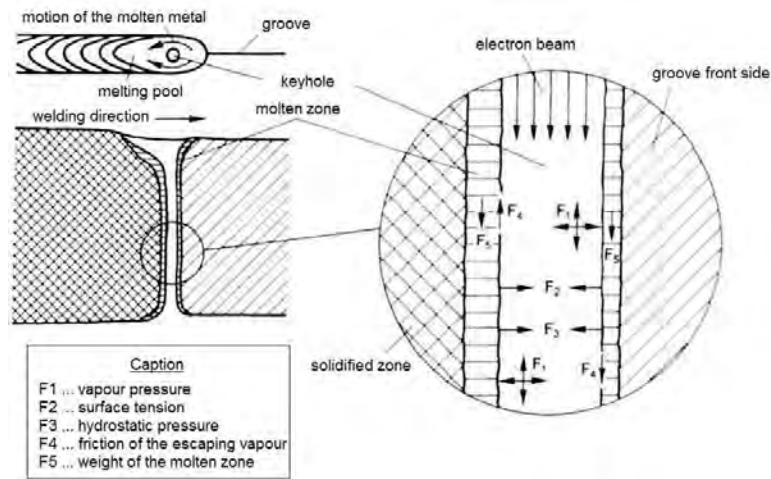


FIGURE 28: FORCES IN THE KEYHOLE [13]

Compared to other welding techniques in EBW a very small area is molten. Figure 29 shows the isothermal lines during EB welding and Figure 30 the temperature gradient in different distances around the beam centre. Measurements were made in mild steel with a thickness of 8 mm, a welding speed of 6.4 mm/s and the welding was done from right to left [29].

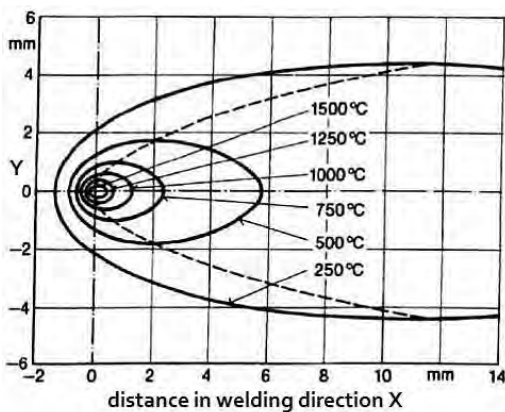


FIGURE 29: ISOTHERMAL LINES EBW [13]

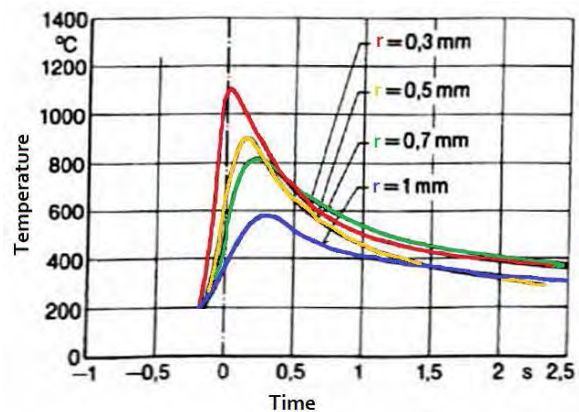


FIGURE 30: TEMPERATURE GRADIENT [13]

By reason of this special characteristic a very low heat quantity is brought into the workpiece [42]. Figure 31 compares the specific heat input of different welding processes.

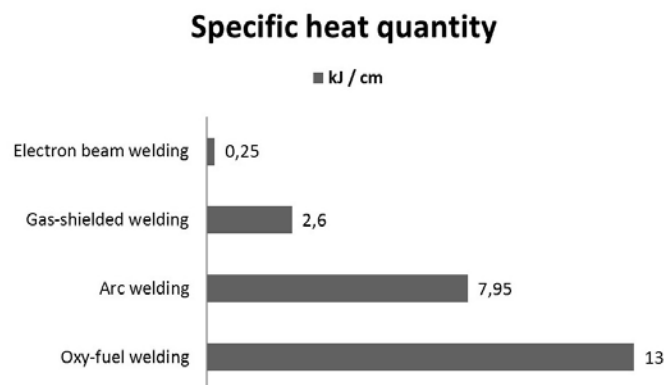


FIGURE 31: SPECIFIC HEAT INPUT OF WELDING TECHNIQUES [42]

2.3.8 SEAM PROPERTIES

EBW is a single layer welding technique with unique high aspect ratio and a very small heat affected zone, particularly in thick walled parts.

In EBW, cooling rates between 10^3 and 10^5 K/s [43] occur. As a result of this short thermal cycle, a very high heat transfer in the material happens. Due to these special circumstances, the materials show no overheated microstructure despite the high peak temperatures. The very fine grains in the HAZ have high strength and toughness and are further required for corrosion resistance of high alloyed steel [29], [24]. Figure 32 shows a cross section of an EB weld in mild steel with a depth of 35mm and a width of 2mm. The visible HAZ on each side is less than 1mm.

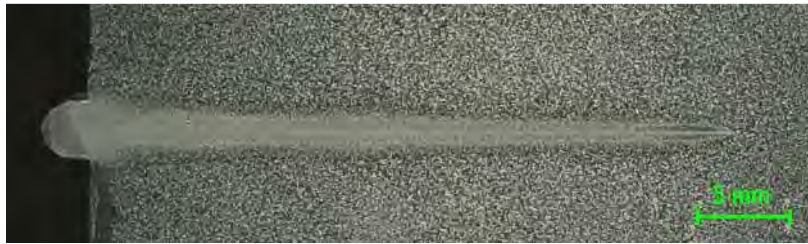


FIGURE 32: STEEL, EB WELD DEPTH 35MM

A disadvantage of this high cooling rate occurs in steels with high carbon content. Martensite with excess hardness is formed. Depending on the material, hardness levels above 600HV can be reached with EBW; way more than in other welding techniques [24], [42].

2.3.9 WELD PREPARATION

Usually EBW is performed without filler material. For this reason, there are two basic joint assemblies as displayed in Figure 33; a) *butt weld* and b) *lap weld* or *pass weld*. A special feature in EBW is the possibility to weld in different levels simultaneously, so that normally inaccessible joints can be made (Figure 34) [37].

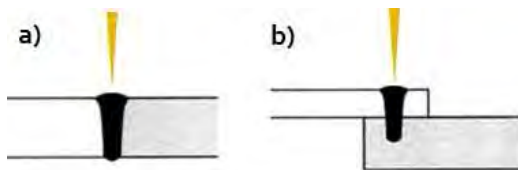


FIGURE 33: BASIC EBW JOINT ASSEMBLIES [44]

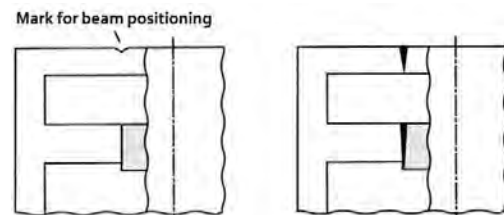


FIGURE 34: HIDDEN JOINT [44]

Because of the narrow fusion zone in EBW a main criterion is the size and the surface quality of the gap between the parts. A blank metallic joint surfaces with an average surface finish of $R_a=1.6$ to maximum $3.2\mu\text{m}$ is required. The surfaces on the top and bottom area beside the seam have to be free of oxides film, grease, oil and paint (Figure 35). Insufficient cleaning causes problems with the vacuum besides incomplete fusions [44].

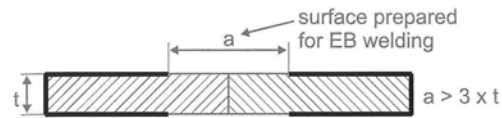


FIGURE 35: SURFACE PREPARING [28], [44]

If a “beam-friendly” design is taken into account, the versatile properties of EBW provide creative designers a powerful tool for numerous ways of solving welding problems.

Basic knowledge of designing for EBW can be found in the *DVS Information Sheet 3201* [44].

2.3.10 SPECIAL WELDING PROCEDURES

Because of the good adjustability of the beam parameters and the fast beam deflection, some special welding procedures can be performed. Especially the very high beam deflection rate offers several possibilities in EBW.

2.3.10.1 MULTI CAPILLARY WELDING

The beam can swap positions so fast that no melting occurs between these positions. For this reason, several welding capillaries can be formed “simultaneously” and kept open. The beam current in the different welding positions is equal. Figure 36 shows multi capillary welding of a gearwheel dummy. The three “simultaneously” created weld seams balance the thermal expansion and reduce distortion significantly [45].

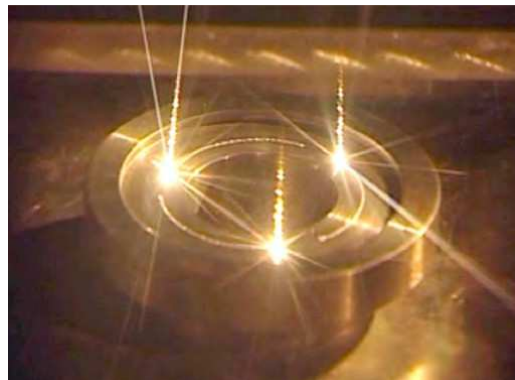


FIGURE 36: MULTI CAPILARY WELDING [45]

2.3.10.2 MULTI POOL WELDING

Multi pool welding means creation of several welding pools with different beam currents at the same time. It is very effective to reduce pores in materials which degas during the welding process causing porosity in the seam (e.g. cast aluminium or cast iron) [28], or to diminish the cooling rate (e.g. α titanium) [46].

Figure 37 and Figure 38 show the multi pool technique and their effect on cast iron, investigated by K. R  thrich and R. Zenker in [47].

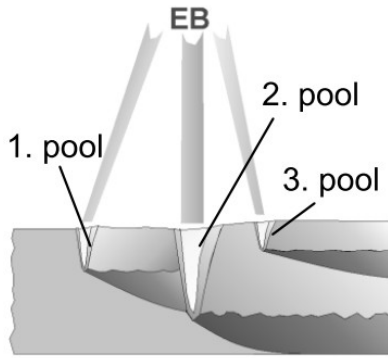


FIGURE 37: CROSS SECTION MULTI POOL WELDING [47]

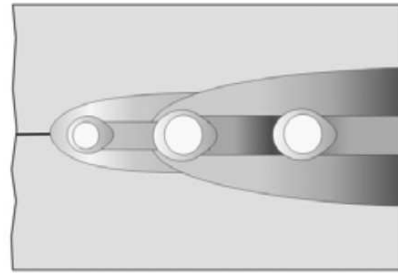


FIGURE 38: TOP VIEW MULTI POOL WELDING [47]

Figure 39 shows cast iron welded with single pool technology and the same material welded with multi pool technology.

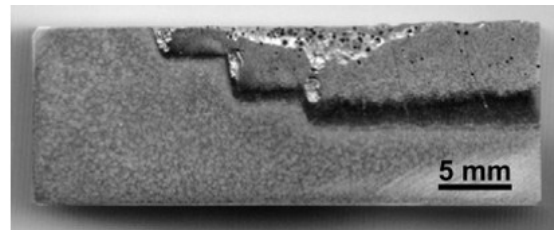


FIGURE 39: PORES IN CAST IRON [47]

The multi pool technique is also used for cosmetic travels along the butt joint to give the weld bead a smooth surface [22].

2.3.10.3 MULTI PROCESS TECHNIQUE

The multi process technique is a procedure where the electron beam is deflected to cause only one welding pool and several heating zones. By adjusting focusing-, current-, and deflection parameters, scanning patterns can be designed [46]. Moreover, modulation of the beam power between the different processing points can be used [31]. The main beam creates the welding seam while the assistant beams are used to bring thermal energy in the workpiece. This technique is used to perform pre-heating (e.g. for high carbon steels) to avoid stress cracks, or to give a post heating treatment to the weld seam of alloys which are prone to hot cracking (e.g. nickel alloys) [28]. Both heat treatments, pre- and post- heating, can be performed at the same time. Figure 40 shows the collocation of the beam.

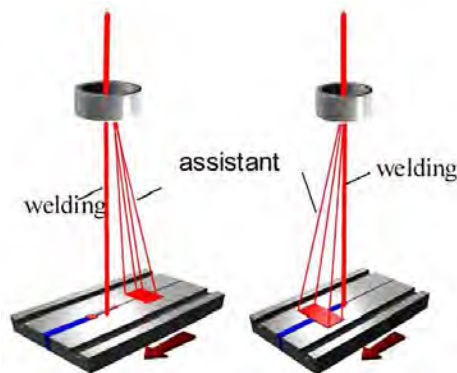


FIGURE 40: MULTI PROCESS WELDING [46]

Such scanning patterns or a strong defocused beam is also used in the electron beam surface treatment technology.

Moreover, a reduced stress level in the work piece can be achieved by creating heating spots, traveling on both sides of the seam. The reduction of the stress level depends on the geometrical parameters shown in Figure 41. In this case, two heat patterns trailing the weld pool at some distance to cause prepressure from thermal extension, which compensates the tensile stress in the weld pool during cooling. The two beam spots, created from a defocused beam or a scanned pattern, should not melt the surface.[28], [48].

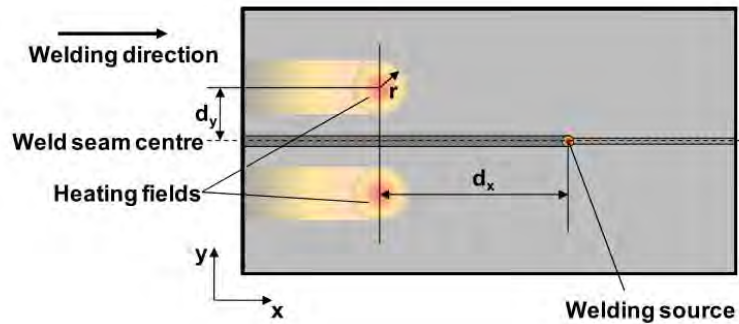


FIGURE 41: STRESS REDUCING BY HEATING SPOTS [48]

In literature there is no clear classification among these techniques. The author of this thesis suggests making the following classification:

1. Multi capillary welding	Several welding seams are created "simultaneously"; the beam doesn't pass areas of the work piece surface twice
2. Multi pool welding	One weld seam is created; several supporting melting pools are created along the seam (different beam currents)
3. Multi process welding	One weld seam is created; assistant beams are used to bring thermal energy into the work piece; only one melting pool occurs

TABLE 1: CLASSIFICATION OF EBW TECHNIQUES

2.3.10.4 FOCUS WOBBLING

Focus wobbling is quite new EB procedure and first investigated by C. Börner, [49]. Focus wobbling is a dynamic focus technique. During welding, the focal point of the beam is changing. This can be done point-wise, the focus jumps between two positions, or by a constantly shift of the focus. C. Börner investigated in [49] the positive influence of focus wobbling on hot crack susceptibility of nickel-based alloys.

2.3.11 THICK WALLED WELDING

A very unique characteristic of electron beam welding is its possibility to weld thick walled parts with a single layer. With modern equipment welds up to 300mm in aluminium and 200mm in steel are possible [50], [51]. The use of this technique is a very strong economic advantage. Figure 42 shows a comparison of a 150mm deep welding; one is produced using EBW and the other one using submerged arc welding (SMAW) [21].

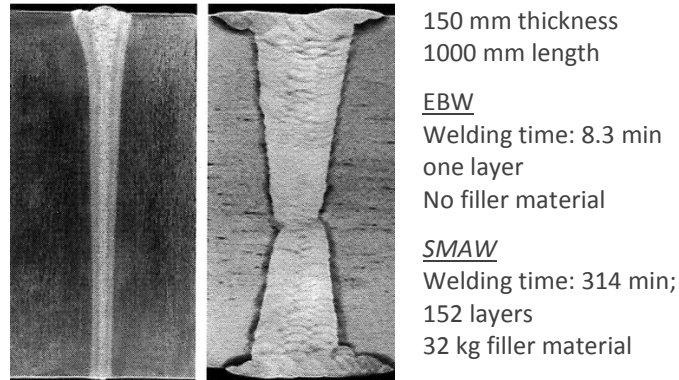


FIGURE 42: COMPARISON EBW AND SMAW [23]

However, it should be noted that with increasing thickness the possibility of welding failures also increases. In a bigger melting pool, the effect of highly dynamic movements increases strongly and moreover the influence of the beam geometry rises. Not only the beam current and the welding speed have a strong influence on the welding, but also the focal position and the beam oscillation gain much higher influence. For deep welds the parameter window for the focal position and the beam oscillation is way smaller than for welds with smaller depth. This of course implies that the effort for the evaluation of the correct welding parameters is increasing with the depth of the welding; not only in case of preparing the parameters, but also in machining and preparing the welded parts for investigation [24], [29].

In thick walled welding, the gravity is an additional key factor. Besides the fact that for thicknesses higher than 30-40 mm the melting is going to leak out on the root side, the mass of the melted material in not full penetration welding makes it difficult to keep the keyhole in vertical position stable [40], [42]. This effect is visible in seam cross section (Figure 43); the bottom of the welding is full of “melting-tips”; the so called “spiking effect”. One possible solution for welds up to 40mm thickness is to do a full penetration welding (what is always to prefer in EBW). For thicker welds, a horizontal welding position (PC-position) must be used [29].



FIGURE 43: SPIKING [29]

Special attention has to be paid on the beam deflection (Seebeck Effect, see 2.3.12.1); even a marginal angular deviation in deep welds could produce a missed joint due to the very thin fusion zone.

2.3.12 DISSIMILAR WELDING

The joining of dissimilar metals is far more complex than producing a similar joint. The difficulties when joining dissimilar materials include the problems when joining each base metal individually, and the problems to the range of their compositions. Furthermore, a possible incompatibility between the two metals must be considered as well. Any kind of physical and/or chemical mismatches can easily result in incompatibility [52].

The main difficulties in dissimilar welding occur in:

- large differences in physical properties
- large differences in melting temperature
- large differences in thermal conductivity
- chemical mismatches (e.g. formation of intermetallic compounds)

EBW offers strategies to reduce or overcome these problems to a certain extent [24], [52], [53]:

- The low total-heat input per length can reduce the residual stresses substantially;
- The high-energy density can solve the problem of the large difference in melting temperature;
- The thermal conductivity problem can be overcome by directing the beam correctly to the required location;
- The small weld bead size of EB welds minimizes the mixing of dissimilar metals; that limits the brittle zones arising from the chemical mismatch;
- Due to the very small time slot of diffusion permitting temperatures, the intermetallic phase fringe can be kept very small;
- Because of the high temperature gradients and associated rapid solidification of the materials, the solubility limit of elements is shifted to higher concentrations. So for a system which usually forms intermetallic phases, mostly other simple formed and less brittle phases occur;

2.3.12.1 THERMOELECTRIC EFFECT (SEEBECK EFFECT)

A special problem in EBW for dissimilar materials is the thermoelectric effect. Temperature gradients existing between the top and the bottom and before and behind the cavity cause thermoelectric currents. These currents induce inner and outer magnetic fields (Figure 44) which can lead to a deflection of the electron beam (Figure 44 and Figure 45) [24], [27]. The deflection can be minimised by using a high acceleration voltage but it still can be critical especially for thick walled parts (>75mm) [24].

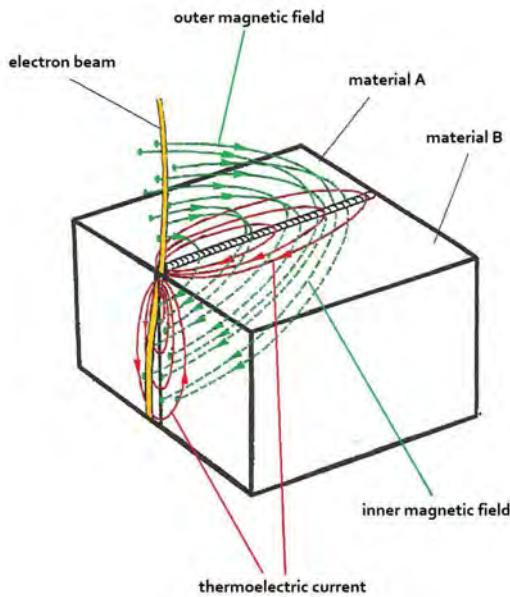


FIGURE 44: THERMOELECTRIC EFFECT [24]



FIGURE 45: BEAM DEFLECTION IN DISSIMILAR WELDING [27]

Because of joining a non-ferromagnetic material (A625) and a ferromagnetic material (CB2) within this thesis, special attention needs to be paid on a previous demagnetizing of the work pieces.

2.4 DESIGN OF EXPERIMENTS (DOE)

This part refers mainly to *TASCHENBUCH VERSUCHSPLANUNG – Produkte und Prozesse optimieren* [54], written by Wilhelm Kleppmann and on the *Minitab® 15* software [55]. Other references are separately identified.

Because time and materials available for the experimental part of this thesis are limited, a compromise between accuracy and reliability has to be found. Especially, if there are several factors influencing a target variable in a different manner, “one factor at a time” - testing becomes unmanageable. By changing more parameters at a time, experimental workload can be reduced significantly. Due to the fact that simultaneous change of multiple factors leads to interactions that are difficult to separate into individual effects, a carefully planning is required.

2.4.1.1 TERMS DOE

The experimental variables have to be divided into **target variables** and influencing **factors**. Target variables represent the result of the experiment and should be measurable. An experiment can have several target values. Factors are the adjustable variables for the experiment chosen out of the pool of influencing variables and which are quantified in **factor-levels**. The levels are the concrete values of the factors (e.g. the factor temperature has the factor-levels 90°C and 100°C). After defining these variables and values, the combination of the factor-levels can be arranged. Depending on the experiment itself and the knowledge about the process that has to be simulated, multiple default experiment designs are available.

2.4.1.2 EXPERIMENTAL DESIGNS

In this thesis, three different designs were used: the **fully factorial design** (FFD), the **central-composite-design** (CCD) and the **Box-Behnken-design** (BBD).

The **FFD** design is the basic design in DOE; it combines every factor level combination. This method compares the arithmetic means of the experimental results. Here an example of a two-factor-two-level design (2^2) (Figure 46) is given.

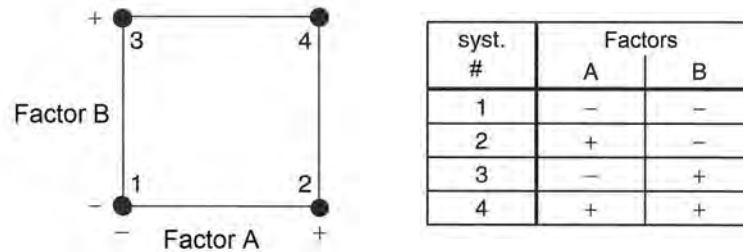


FIGURE 46: 2-FACTOR-TO-LEVEL DESIGN [54]

The figure above shows the experimental design of the two factors A and B, each factor with two factor levels (+ and -). The effects of the factors can be calculated as follows.

$$Effect A = \frac{y_2 + y_4}{2} - \frac{y_1 + y_3}{2}$$

$$Effect B = \frac{y_3 + y_4}{2} - \frac{y_1 + y_2}{2}$$

EQUATION 7: EFFECT A AND B [54]

The effect AB is called interaction effect. The interaction effect indicates how much a factor depends on the other factor.

$$Effect AB = \frac{y_4 - y_3}{2} - \frac{y_2 - y_1}{2} = \frac{y_1 - y_2 - y_3 + y_4}{2}$$

EQUATION 8: INTERACTION EFFECT AB [54]

With every more factor the experimental capacity doubles (Figure 47).

syst. #	Factor A	Factor B	Factor C	Factor D	...
1	-	-	-	-	-
2	+	-	-	-	-
3	-	+	-	-	-
4	+	+	-	-	-
5	-	-	+	-	-
6	+	-	+	-	-
7	-	+	+	-	-
8	+	+	+	-	-
9	-	-	-	+	-
10	+	-	-	+	-
11	-	+	-	+	-
12	+	+	-	+	-
13	-	-	+	+	-
14	+	-	+	+	-
15	-	+	+	+	-
16	+	+	+	+	-

FIGURE 47: FULLY FACTORIAL DESIGN TABLE [54]

The FFD is a linear system of equations. Consequently, the resultant model is also linear. The model shows the main trend of the experiment but it does not show if there are nonlinear correlations in the parameter. To identify a non-linear phenomenon the CCD is required.

The **CCD** is usually used for experiments where the key-variables are already known and an optimised value for the target variable is requested. Additionally, the CCD is appropriate for testing new operating conditions because of the quadratic solution statement. In the following figure, the difference from FFD to CCD is pointed out. In addition the CCD has to the FFD a centre point and 6 points outside the testing area.

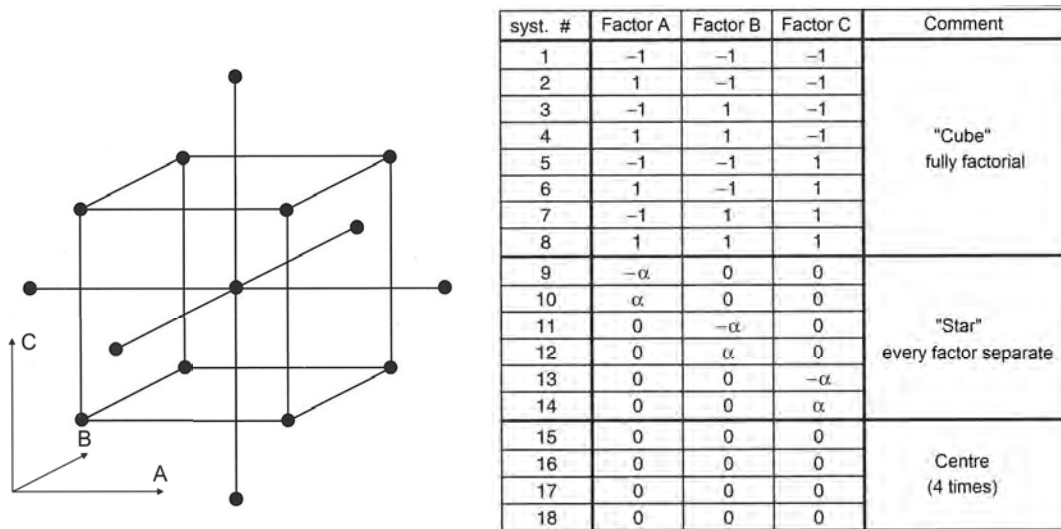


FIGURE 48: CENTRAL COMPOSITE DESIGN [54]

The **BBD** is a modified version of the FFD. All factors are only varied between three levels; this reduces the number of trials. The geometry of this design represents a sphere within the process volume. Another advantage of the BBD is the avoidance of extreme factor combinations, all testing points are in the middle on the edges of a cube. The disadvantages of the BBD are that the non-linear connections cannot be determined and the results are less accurate compared to the CCD.

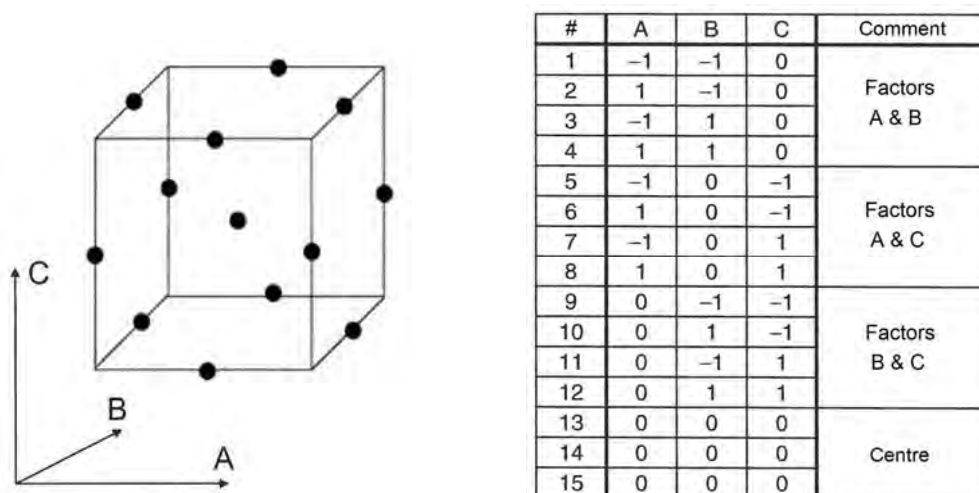


FIGURE 49: BOX-BEHNKEN DESIGN [54], [55]

2.4.1.3 ARRANGEMENTS

If an execution of the experiment plan cannot be done at once, **blocking** is necessary (e.g. several batches of specimens are needed or several days are needed). Blocking means the arrangement of the single trials in blocks, where every factor combination is represented.

At last a **randomisation** has to be done. The randomisation is needed to avoid trends and to suppress unknown disturbances.

2.4.1.4 ANALYSIS

To display the interaction between two factors and the response to the target variable **factorial-plots** are used. These diagrams are based on the mean values of the results. The following pictures show how factorial-plots illustrate the effect of single factors (A & B) and also the interaction between these factors on the target variable (Y).

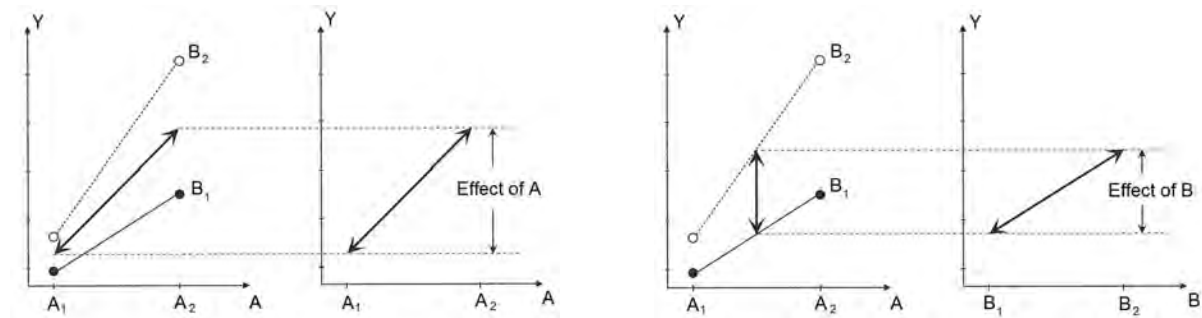


FIGURE 50: EFFECTS OF A AND B [54]

The interaction is represented by the deviation to parallelism of these two lines (Figure 51).

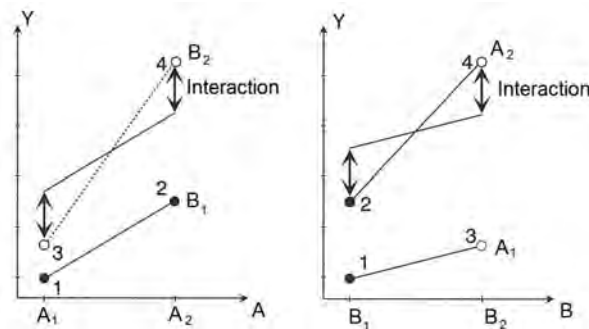


FIGURE 51: INTERACTION OF A AND B [54]

Another useful tool is the **main effects plot**. It is used to visualize the effect of the factors on the response and to compare the relative strength of the effects. Particularly, in case of having several factors the main effects plot can show which effect influences the response most. A main effect is present when different levels of a factor affect the response differently.

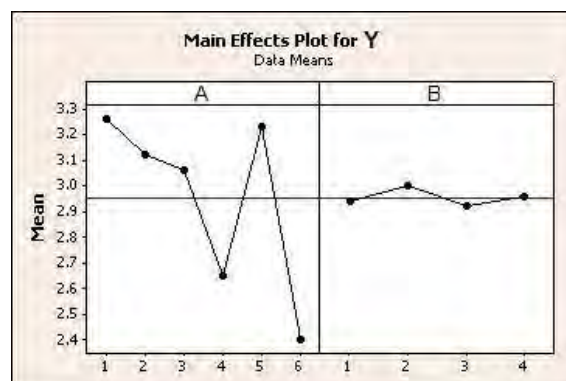


FIGURE 52: MAIN EFFECTS PLOT [55]

In Figure 52, a main effects plot is shown where the factors A and B response to Y. The horizontal line at 2.95 is the mean value for Y. The zigzag line represents the influence of the factors to the mean value. If the line follows the horizontally mean, there is no main effect; if the line increase or decrease a main effect is present. Figure 52 illustrates that A has a strong effect on Y and B nearly does not affect Y.

If the main task of the experiment is to determine the factor combination for a certain target value a **contour plot** or a **response surface model** is very helpful. The response surface model is a three dimensional view where the surface represents the target variable. The contour plot is a two dimensional view where points with the same target-variable value are connected; contour lines with constant data occur. Below an example of each mentioned result visualisation is shown. Both contain the same data.

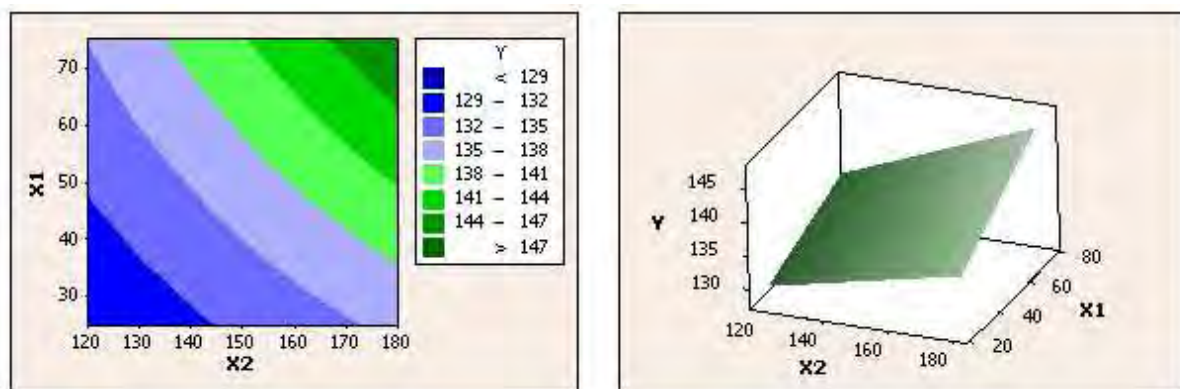


FIGURE 53: CONTOUR PLOT AND RESPONCE SURFACE MODEL [55]

The analysis of the experiments is usually done with software support. Especially in pictorial representation of the results such software is a very powerful tool. In this thesis Minitab® 15.1 was used.

3 METHODS

The Methods part first provides basic information about the investigated materials (chemical composition and the mechanical data) and second, a description of the EBW machine. Subsequently, a detailed description of the experiments performed in this thesis is given; the testing routine is described, the chosen welding parameters are listed and the analysis methods are mentioned. The subsection order follows the chronological order of the experiments. All evaluation and examination methods are described in chapter 3.6. INVESTIGATIONS.

The testing schedule can be roughly segmented into four phases:

1. Parameter selection	<i>Classify welding parameters in adjustable parameters and constant parameters</i>
2. Blind Welding	<i>Blind welding in a full block to determine basic parameters for A625 and CB2</i>
3. Joint welding	<i>Joint welding of A625 (similar) and A625 with CB2 (dissimilar)</i>
4. Welding test according to EN standard (pWPS)	<i>Joint welding of Alloy 625 with COST CB2 according to EN ISO 15609-1</i>

TABLE 2: TESTING SCHEDULE

The following flowchart shows the workflow of the experiments and investigations.

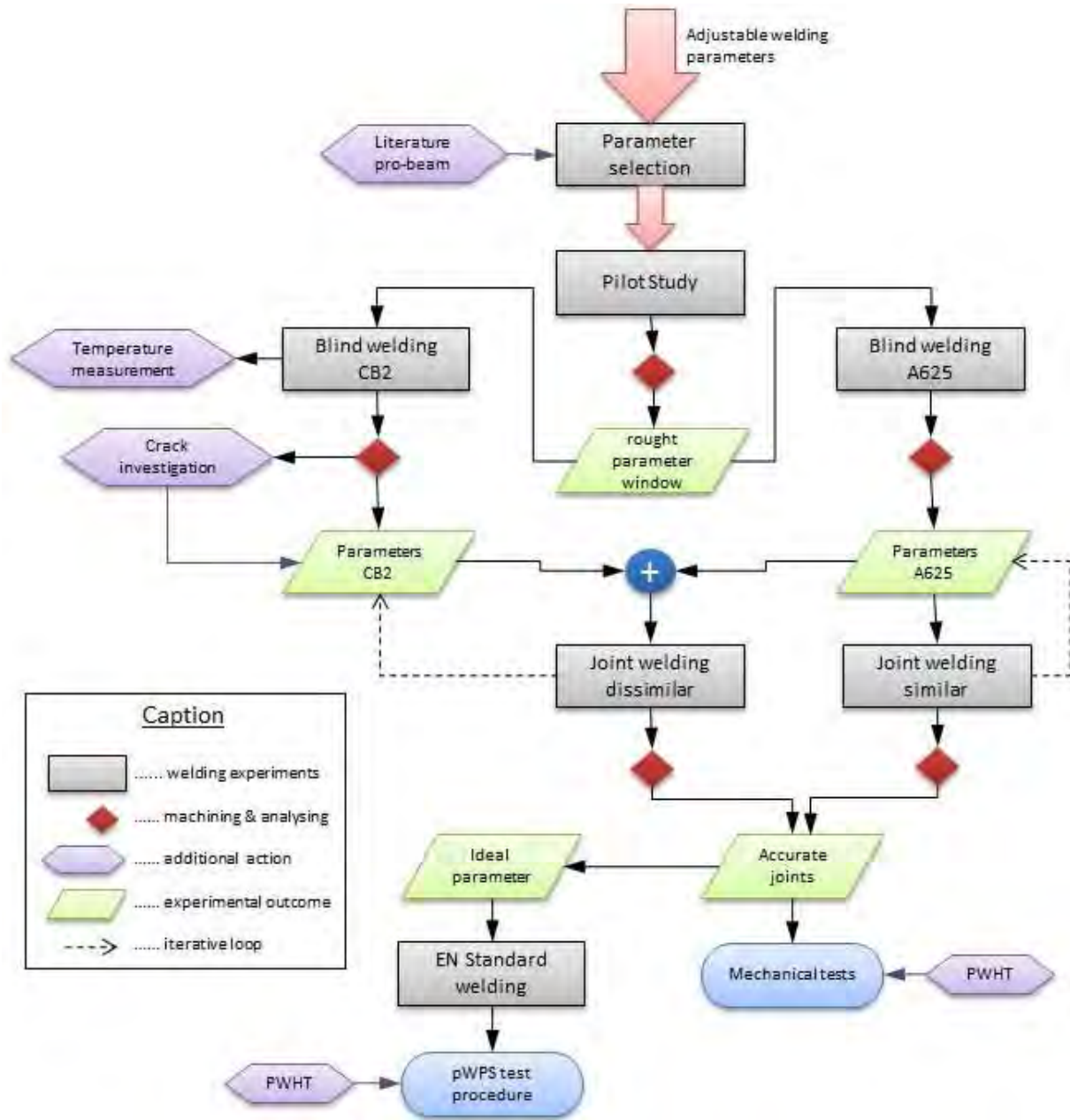


FIGURE 54: EXPERIMENTAL WORKFLOW

3.1 MATERIALS

The materials investigated in this thesis were provided by the *voestalpine Gießerei Traisen* (VAGT). (Figure 55 and Figure 56).



FIGURE 55: CB2 BLANKS



FIGURE 56: A625 BLANKS

Two blanks of the CB2 and two blanks of the A625 were used. A cutting plan was worked out to make good use of the restricted amount of material.

3.1.1 CB2

The labeling of the CB2 is ***GX13CrMoCoVNbNB10-1-1***; a standard number does not exist. The chemical composition can be found in Table 3 [56]. After casting, the material was austenitised and tempered at 760°C. The mechanical properties are shown in Table 4 [56].

	C	Si	Mn	P	S	Al	Co	Cr
Min.	0.120	0.200	0.800	-	-	0.010	0.900	9.000
Max.	0.140	0.300	1.00	0.015	0.005	0.020	1.100	10.00
Act.	0.143	0.262	0.857	0.011	0.001	0.018	0.947	9.516
	Cu	Mo	V	Nb	Ni	Ti	B	N
	-	1.400	0.180	0.050	0.100	-	0.008	0.015
	0.100	1.600	0.220	0.070	0.200	0.005	0.015	0.030
	0.056	1.492	0.198	0.059	0.164	0.002	0.011	0.024

TABLE 3: NOMINAL AND ACTUAL CHEMICAL COMPOSITION OF CB2 STEEL [56]

	Rp02%	Rm	A5	Av 20°C	HV 10
	MPa	MPa	%	J	
Nom.	450	600-750	15.0		
Act.	591	727	15.9	44	215

TABLE 4: MECHANICAL PROPERTIES OF CB2 MATERIAL[56]

Figure 57 shows the tempered martensitic structure of the material. The prior austenite grain boundaries are still visible and some precipitates ($M_{23}C_6$ and/or MX) are identified, which are main contributors to the creep strength [14].

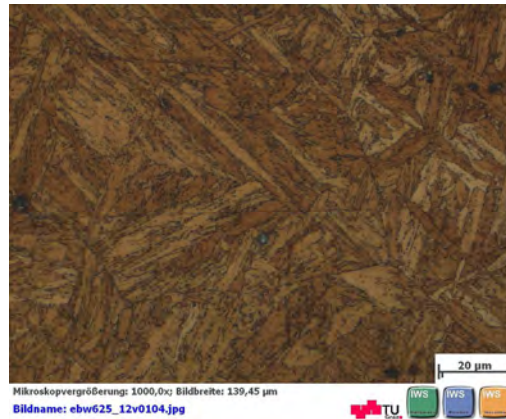


FIGURE 57: CB2 MICRO STRUCTURE

3.1.2 A625

The labeling of the alloy 625 is **NiCr22Mo9Nb**, standard number is 2.4856. The composition is listed in Table 5 [57]. The material was delivered in the solution annealed condition. The mechanical properties are shown in Table 6 [58].

	C	Si	Mn	P	S	Al	Co
Min	0.03	-	-	-	-	-	-
Max	0.100	0.500	0.500	0.02	0.015	0.400	1.000
Act.	0.018	0.334	0.201	0.005	0.001	0.109	0.001
	Cr	Fe	Mo	Nb + Ta*	N	Ti	
	20.00	-	8.000	3.150	-	-	
	23.00	5.000	10,00	4.200	0.400	0.400	
	21.702	1.037	8.933	3.507	0.001	0.0039	0.197

TABLE 5: NOMINAL AND ACTUAL CHEMICAL COMPOSITION OF A625 (WEIGHT PERCENT) [57]

*20% of Nb can be replaced with Ta

	Rp02%	Rm	A5	Av 20°C	HV 10
	MPa	MPa	%	J	
Nom.	275	400	20	50	-
Act.	257	475	56	-	160

TABLE 6: MECHANICAL PROPERTIES OF A625 IN SOLUTION ANNEALED CONDITION [58]

In Figure 58 the solution annealed microstructure of A625 is shown. The large grains size and the high amount of pores are typical for cast material. Under high magnifications, precipitates at the grain boundaries can be recognized and within the grains (Figure 59). The gold colored precipitates are titanium carbides and/or titanium niobium carbonitrides [59], [60].



FIGURE 58: A625 MICRO STRUCTURE



FIGURE 59: A625 PRECIPITATES

3.2 EBW MACHINE

The EB machine was manufactured by *pro-beam* (www.pro-beam.com); it is the “Universal-chamber machine EBG 45-150 K14” model. This machine type offers a wide range of applications; it is especially appropriate for research and for welding prototypes. A picture of the used machine and a scheme of the functionality are showed below.



FIGURE 60: EBW-M @ TU GRAZ

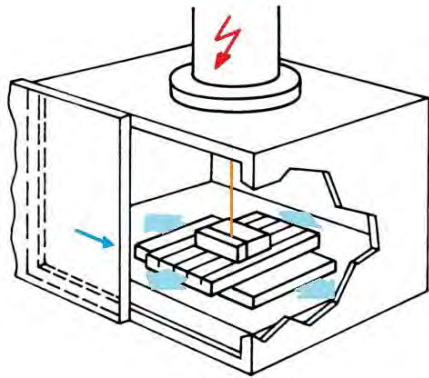


FIGURE 61: BUILD -UP CHAMBER MACHINE

The benchmarking data can be found in Table 7. A welding depth of 100mm for steel and 200mm for aluminum is assured for this machine.

EB Gun	
Power	45kW
High Voltage	150kV
Beam Current	0,1 - 300mA
Beam oscillation	1° / µs
Chamber	
Volume	1.4 m ³
table feed rate	0,5 - 100mm/s
Vacuum (operating pressure)	
Evacuation time	< 6min
EB Gun	≤ 5 x 10 ⁻⁵ mbar
Chamber	≤ 5 x 10 ⁻³ mbar

TABLE 7: BENCHMARKING DATA EB-MACHINE

3.3 PARAMETER SELECTION

In EBW technology, a lot of different welding parameters affect the resulting weld. To keep the experimental workload feasible, the modifiable parameters had to be reduced. This was done by focusing on these parameters which are significant for the welding procedure and have a good adjustability; all other parameters are kept constant during the experiments. During EBW training, guided by the pro beam staff, and a literature study of the beam-welding basics, the following parameters arrangement was done:

- Constant parameters
 - Acceleration Voltage: 120 kV
 - Operating distance 895mm (104mm above the working table)
 - Beam figure / oscillation frequency: Circle / 600 Hz

- Adjustable parameters
 - Beam Current: I
 - Welding speed: v
 - Focal Position: fp
 - Figure amplitude: h

With this selection the scope for the design of experiments (DOE) was defined.

3.4 BLIND WELDING

The blind welding was the second test phase in this thesis. The goal of the preparative testing was to evaluate which parameter affects the welding in which aspect. All welding seams in this section are performed in a full block (blind welds). The target variable is the welding depth.

The test set-up for all tests in this phase one was constant; several welds with different parameters were done in a big block. The block was supported with an extra plate to avoid total beam penetration. This structure was placed on two flat rods to avoid an accidental welding to the machine table if beam power is still too high. The dimensions of the used blocks differ slightly because of the geometry of the different blanks, from which they were cut out.

Welds were done parallel with small spacing (~10mm) to make good use of the material. Start and end point of the welding was within the block. In Figure 62 the test set up for the blind welding tests is shown.

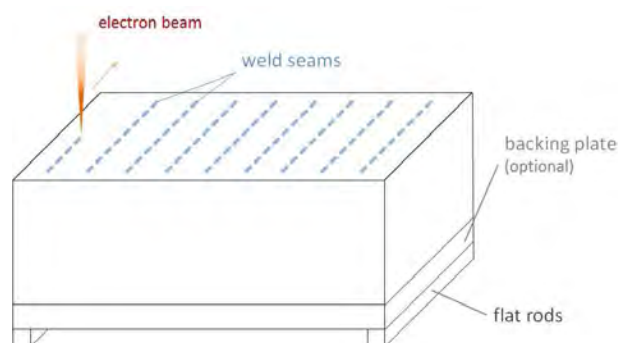


FIGURE 62: PRE-TEST SPECIMENS

After welding, each specimen was cut at several positions, perpendicular to the welding seams to determine the penetration depth and to search for potential defects along the seam. After a macroscopic etching, the penetration depth of the beam was measured digitally with the Axio Visio Release 4.8.2 Software. Statistical and mathematical analysis was done with Minitab® 15.1 and Microsoft Excel.

3.4.1 PILOT STUDY

In a pilot study, the first welds for this thesis were performed in a big steel block. A quite high beam current was applied to determine the maximum usable parameters without damaging the machine. Moreover this was done to obtain a smaller parameter window for the two main parameters I and v . The blind welds were carried out in a big mild steel block, to get an idea of the approximate beam penetration for different parameters. Although the material used in this study differs from the material used later for welding, a rough parameter window could be estimated. This test was mainly designed to prevent the machine from being damaged seriously by choosing wrong welding parameters.

The pilot study was completed in FFD. Factors were the beam current (I) and the welding speed (v); target variable was the penetration depth (t).

Constant parameters were set as written in 3.3 PARAMETER SELECTION on page 36; the focal position was set to $fp = -20\text{mA}$. No beam oscillation was used for this test. The factor combination for the FFD is shown in Table 8.

#	Beam current I / (mA)	Welding speed v / (mm/s)
1	105	5
2	205	5
3	105	15
4	205	15

TABLE 8: FACTOR COMBINATIONS PILOT STUDY

With the results of the pilot study the testing area for the CB2 blind welding could be restricted. The localisation of the “parameter box” for the blind welding was done geometrical by drawing the new parameter box on the plot of the pilot study contour plot.

3.4.2 TEMPERATURE MEASUREMENT

In cooperation with Michael Hörtenhuber (working on his Bachelor thesis „*Planung, Konstruktion und Fertigung einer gekühlten Unterlagsplatte aus Aluminium für das Elektronenstrahlschweißen*“), a temperature measurement during welding, using two thermocouples (TC), was performed. The measurement was done to determine the temperature development in a welded part next to the seam. After 10s welding, the temperature was recorded for 30 minutes. During cooling, the welded block remained in the vacuum chamber.

The first thermocouple was welded on the top of a 50x50x100mm CB2 steel block, 5mm beside the welding path. The second thermocouple was positioned in the same way but placed 15mm besides the welding path. The block was supported with a backing plate to enable a 50mm deep welding. The experimental set up is illustrated in Figure 63. The welding parameters were: $I = 180\text{mA}$; $v = 10\text{mm/s}$;

$f_p = -30\text{mA}$; circular beam oscillation with an amplitude of $h = 0.5\text{mm}$ and a frequency of 600Hz ; seam length 100mm .

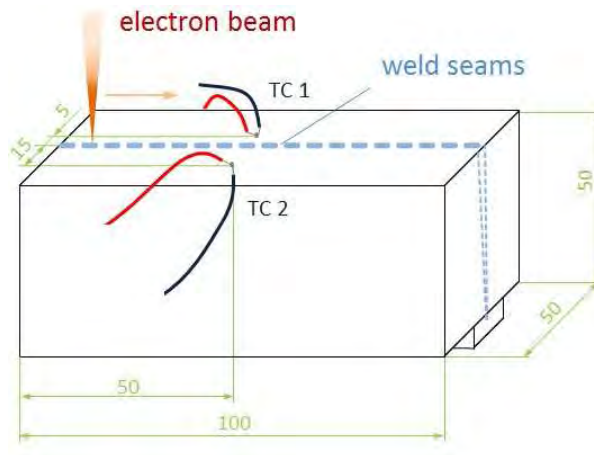


FIGURE 63: TEMPERATURE MEASUREMENT SET UP

3.4.3 BLIND WELDING CB2

This blind welding study was carried out with several welds performed in four COST CB2 blocks. The welds were made alternately in two blocks to reduce influence of residual heat of previous welds. Moreover one middle parameter combination (parametric centre point) was used a number of times during the experiments. With these reference points, the change in welding depth, due to the increasing temperature of the block after several weldings, could be considered. Totally, 30 welds were performed in this study.

For the first two blocks the experimental design was central-composite (CCD) with four factors: beam current (I), welding speed (v), focal position (Fp) and figure amplitude (h). Target variable was the welding depth. Constant parameters were set as defined in 3.3. The range of the factor levels are shown in the table below (a detailed list of all trials is given in the RESULTS part).

<i>Factor levels</i>	Beam current $I / (\text{mA})$	Welding speed $v / (\text{mm/s})$	Focal point $f_p / (\text{mA})$	Figure amplitude $h / (\text{mm})$
Minimum	150	5.50	-30	0
Maximum	180	9.00	0	1.00
Centre	165	7.25	15	0.50
Min. star point	135	10.75	-45	0.25
Max. star point	195	3.75	-45	1.25

TABLE 9: PARAMETERS BLIND WELDING CB2, BLOCK 1 & 2

Because of the appearance of cracks in most of the welding seams in the first two CB2 blocks, an additional investigation on cracking was made.

In block three and four, successful trials of the two first blocks were repeated. In matter of welding depth and seam shape, small parameter variations were done to enhance the results. The welding parameters are listed in Table 10. Owing to the results of block one and two, the focal position for block three and four was held constant with $f_p = -30\text{mA}$ (# weld number, Bl. Block number)

#	Bl.	Beam current I / (mA)	Welding speed v / (mm/s)	Figure amplitude h / (mm)
1	1	150	8.00	0.50
2	1	160	8.75	0.50
3	1	170	8.50	0.75
4	1	160	8.00	0.75
5	2	150	7.50	0.75
6	2	180	6.75	1.00
7	2	165	6.50	1.00
8	2	150	6.25	1.00

TABLE 10: PARAMETERS BLIND WELDING CB2, BLOCK 3 & 4

3.4.4 BLIND WELDING A625

In this third part of the blind welding study, three nickel based alloy blocks were used. For block one and two, the BBD experiment concept was used. The advantage, compared to the CCD which was used for the CB2 blind welding, is a reduced number of trials (15 trials instead of 20, by varying three factors). Another advantage of this experimental design is that no parametric extreme points are tested and no star points need to be done.

The approach for this study was the same as in the CB2 blind welding study. The smaller geometry of the nickel base specimen reduced the number of trials to 14. Based on the results of CB2 blind welding study, the focal point was set constant at -30mA. The parameter range in which the values were varied is listed in Table 11.

<i>Factor levels</i>	Beam current I / (mA)	Welding speed v / (mm/s)	Figure amplitude h / (mm)
Minimum	150	5.0	0
Maximum	180	10.0	1.0
Centre	165	7.5	0.5

TABLE 11: PARAMETERS A625, BLOCK 1 & 2

For the third A625 block the trials were performed in FFD. Due to the less accurate BBD design, used in block one and two, the FFD offers additional results usable with software analysis methods. The oscillation amplitude was held constant at 0.5mm, therefore a short testing plan was feasible. The focal point for every welding was set constant at -30mA. Table 12 shows the setup for the single trials.

#	Bl.	Beam current I / (mA)	Welding speed v / (mm/s)
1	1	150.0	10.00
2	4	150.0	7.50
3	3	157.5	8.75
4	2	165.0	10.00
5	5	165.0	7.50

TABLE 12: PARAMETERS A625, BLOCK 3

Every welding here was performed in the cold block. So the block had to be cooled down in air after each welding; so only two welds per day could be executed. Adjusting the machine for every welding may lead to slight scattering in the machine calibration (vacuum, beam adjusting, zero-focus,...), but the temperature influence, which has way more effect on the welding behaviour, can be eliminated.

3.5 JOINT WELDING

The welding section contains all experiments according test phase three (joint welding) and four (EN standard welding specification test). In each testing phase, several welds with different parameter settings (I , v and h) were produced. Within these experiments not only the welding depth but also the microstructure of the weld and mechanical values of the joint were analysed.

3.5.1 TEST SET-UP

The joint samples were assembled from three parts; two equal blocks (50x50x100 mm), to be welded and a backing plate (10x20x100mm). The backing batten was needed to protect the weld pool of draining out due to the influence of gravity on the liquid metal. This design leads to an optimum welding depth of 55mm, to produce a complete joint for the 50mm blocks with the seam root in the backing batten.

The three parts were tack welded together on both end walls using the tungsten inert gas welding method (TIG) without filler material. All edges were deburred and the surfaces were cleaned with alcohol before tacking and welding. In Figure 64 A) the three parts, of which a joint sample is assembled, are shown; in B) the path of the beam is shown and in Figure 64 C) the finished weld with a nominal depth of 55 mm is illustrated.

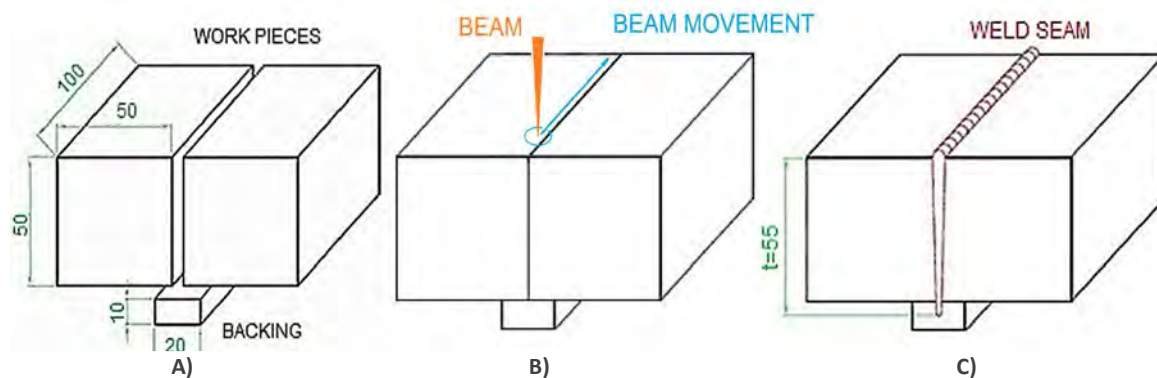


FIGURE 64: WELDING SETUP STANDARD

For similar welding experiments all parts were made of A625; for the dissimilar welding one of the workpieces and the backing batten were made of CB2.

Some bigger samples for side bend testing were also machined. To get adequate sized side bend test pieces the joint samples had to be assembled of two parts with the double width (50x100x100mm). The arrangement of these parts was identical to the standard joint samples.

Every welded specimen gets an identification number (ID). It is a combination of the joint variant (S for similar or D for dissimilar), the numbers, stamped on the work pieces by the VAGT, and an additional B if it is a bending test specimen.

3.5.2 SIMILAR WELDING A625

In this phase, the first joints were welded. The welding experiments were done in several batches. After welding one batch (one to three joints), the welded parts got investigated.

Every weld was done on the cold specimen, and for all of these welds the same focal point (-30mA) was used. Table 13 shows the parameters for single trials in this experiment. Eleven welds had to be done to get the designated number of test pieces for the mechanical testing.

#	ID	Beam current $I / (\text{mA})$	Welding speed $v / (\text{mm/s})$	Figure amplitude $h / (\text{mm})$
1	S14/15	165	10.0	0.5
2	S27/28	165	10.0	0.5
3	S16/17	165	7.5	0.5
4	SS29/30	165	7.5	0.5
5	S7/8	150	9.0	0.5
6	S3/4	165	11.0	0.5
7	S1/6	180	15.0	0.5
8	S9/10	165	10.0	1.0
9	SS26/31	185	11.0	0.5
10	S6/10B	165	10.5	0.5
11	S11/12B	165	10.0	0.5

TABLE 13: PARAMETERS FOR A625 SIMILAR JOINTS

3.5.3 DISSIMILAR WELDING A625 / CB2

With these experiments the welding study continued. The experimental process is the same as for phase two. Again, for all of these welds the same focal point (-30mA) was used. Special attention was paid to an accurate demagnetisation before welding, to avoid a beam deflection due to the Seebeck effect. Every weld was carried out on the cold specimen. Table 14 shows the parameters for the 14 welds that had to be done to get the designated number of test pieces for the mechanical testing.

#	ID	Beam current $I / (\text{mA})$	Welding speed $v / (\text{mm/s})$	Figure amplitude $h / (\text{mm})$
1	D2/2	165	10.0	0.5
2	D11/12	150	9.0	0.5
3	D5/11	180	15.0	0.5
4	D10/24	170	11.0	1.0
5	D4/11	175	10.0	0.5
6	D3/23	160	9.0	0.5
7	D17/25	185	11.0	0.5
8	D13/18	170	10.0	0.5
9	D15/17	180	10.0	0.5
10	D9/22	210	12.0	0.5
11	D6/37	170	10.0	0.5
12	D9/5	180	10.0	0.5
13	D5/6B	165	10.5	0.5
14	D7/7B	175	10.0	0.5

TABLE 14: PARAMETERS DISSIMILAR JOINTS

3.5.4 EN STANDARD WELDING PROCEDURE SPECIFICATION (WPS)

For the EN standard welding test, the size of the specimen was enlarged to 50x300x350mm (plus a 10x20x350mm backing batten). The arrangement was the same as for the other welding tests. Figure 65 shows the specimen arranged on the EB machine table before welding.



FIGURE 65: EN STANDART PART

This **final welding** was done with the best parameter combination found in the previous performed welding trials.

Beam current $I / (\text{mA})$	Welding speed $v / (\text{mm/s})$	Focal point $fp / (\text{mA})$	Figure amplitude $h / (\text{mm})$	Welding time in seconds
180	10	-30	0.5	35

TABLE 15: PARAMETER SET FOR WELDING SPECIMEN TO BE TESTED ACCORDING EN ISO 15614-1

3.5.5 POST WELD HEAT TREATMENT

As known from literature, in electron-beam welding very high hardness values can be reached. Especially, for CB2 a high hardness in the HAZ is expected. Due to the very small dimension of this brittle layer, there are different meanings about its effect on the joint, and on the performance of the component in later applications. In this thesis, some of the dissimilar welded mechanical test pieces were subjected to a post weld heat treatment to investigate the influence of this hardness peaks in comparison with the test pieces in as welded (AW) state.

The VAGT recommended a temperature of 700°C for less than 2 hours for these parts. The time should be as short as possible but long enough to reduce the hardness below the maximum hardness of 350HV defined in the standard (ÖNORM EN ISO 15614-1 [61] and ISO/TR 15608 [62] material group 9.1).

After two post weld heat treatment (PWHT) trials at 700°C for 60min and 120min, plus a following microscopic examination and a hardness measurement, the PWHT was set to 60min at 700°C. The PWHT was applied to the finished machined mechanical test pieces in an ambient furnace.

3.6 INVESTIGATIONS

To receive results from the experiments, different investigation methods are required. This chapter describes the necessary preparations and the execution of all made investigations.

3.6.1 TEST ORGANISATION

In this part, the organisation of the different investigation steps is described, as well as their extent. In the blind welding phase, every weld was cut several times and microscopically investigated. In the joint welding phase, a joint had to pass every investigation level to come to the next one. The first inspection was a simple visual examination of the weld bead. The seam face allows a conclusion on the weld quality- porosity or a leaked out melting pool can be recognised. Nevertheless, most of the

welds were cut to get a safe result. If the saw cut surface did not show a welding failure, the surface was prepared for metallography. If the microstructure of the welding was good too, the joint specimen was qualified for mechanical testing.

Figure 66 shows a block diagram of this sequence which finally led to twelve specimens (five similar, seven dissimilar) for mechanical testing. The number of the joint specimens was determined by the amount of required test results. Figure 67 shows a picture of the specimens before machining.

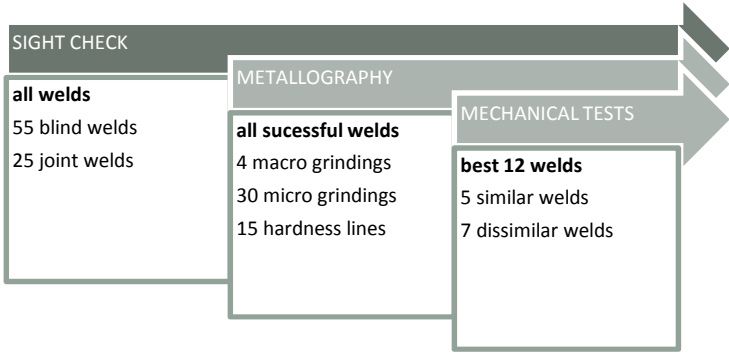


FIGURE 66: FLOW OF TEST MATERIAL



FIGURE 67: SAMPLES FOR MECHANICAL TESTING

Out of these 12 welded specimens and the EN standard weld test piece, the following amount of samples for mechanical testing were manufactured and tested.

	Tensile samples	Charpy samples	Side bend samples
AW	18	36	4
PWHT	9	30	3

TABLE 16: MECHANICAL TEST MATRIXSAMPLES

3.6.2 TESTING SPECIMENS

The first step was to divide the joined samples into the different mechanical test pieces. According to DIN standard ÖNORM EN ISO 15614-1 [61] and the EN ISO 15614-11 [63], the following test specimen layout was chosen; Figure 68 shows the layout for the tensile (T) and the Charpy (C) specimen. Figure 69 shows the layout for the side bend test specimen. From every specimen, a metallography and a hardness test piece (M+H) was taken.

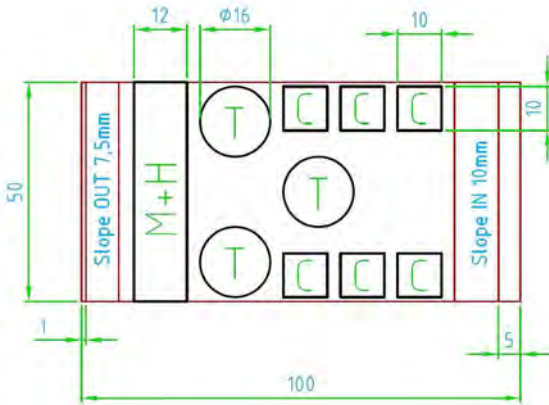


FIGURE 68: SPECIMEN LAYOUT

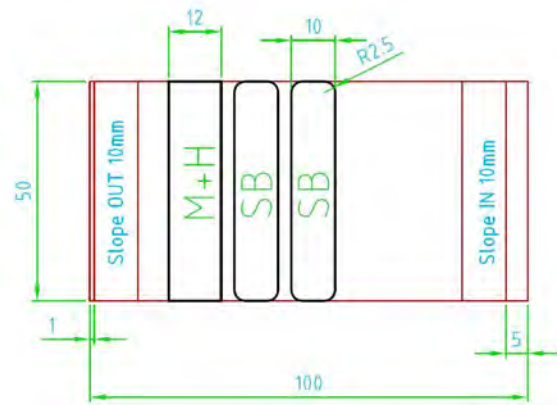


FIGURE 69: SPECIMEN LAYOUT SIDE BEND

The metallography and hardness test piece was cut off and prepared at the TUG, all other test pieces were cut by wire-eroding at the *Harald Umreich Ges.m.b.H.* The final machining was done at the TUG. Figure 70 shows a joint sample after wire eroding.



FIGURE 70: WIRE ERODED JOINT SAMPLE

The next two pictures show the welded EN standard specimen. In Figure 71, a picture of the welded part is shown and Figure 72 illustrates the positions where the mechanical test pieces were taken from. Additionally to the required welding test pieces, tensile and Charpy test pieces were taken from the edge of the workpiece to characterise the base material. This offers the possibility to compare the mechanical values of the welded and base material directly. The machining of the EN standard plate and the later on mechanical testing was done at the VAGT in Traisen.



FIGURE 71: WELDED EN STANDARD PART

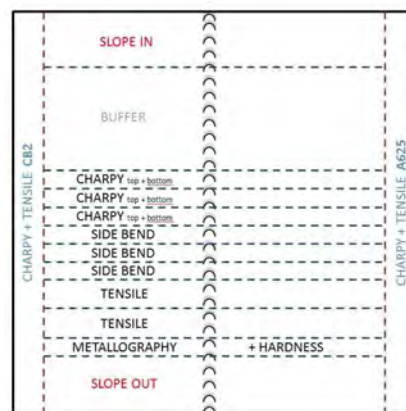


FIGURE 72: SPECIMEN LAYOUT EN STANDART PART

3.6.3 MACROSCOPY

The macro examination was needed to identify the seam geometry (width, shape and penetration depth) and the heat affected zone of the welding. After welding, the specimen was cut perpendicular to the welding seam to get a cross section. Then the specimens were mechanically ground with silicon-carbide paper (grid 80, 120, 220, 320, 500, 800, and 1200). Next, the ground surfaces were cleaned with an alcoholic solution in an ultrasonic bath to facilitate the upcoming etching. Then, the specimens were etched with Adler etchant (see composition in Table 17). The surface is treated as long as the fusion zone and the heat affected zone appear clearly. When finished, the specimen were cleaned with water and alcohol and subsequently dried for several minutes. Finally, the etched surface was photographed. The pictures were edited and dimensioned with Axio Visio Release 4.8.2.

Etching agent	Composition	Execution	Outcome
Adler	<ul style="list-style-type: none"> - 100 ml distilled water - 12 g ammonium tetrachlorocuprate(II) dihydrate $(NH_4)_2[CuCl_4] * 2 H_2O$ - 50 ml hydrochloric acid HCl - 60 g Iron(III) chloride $FeCl_3 * 6 H_2O$ 	<p>The surface is wiped with a soaked cotton-wool ball until the weld seam and the grain boundaries appear</p> <p>CB2: \approx 30 seconds A625: > 3 minutes</p>	Macro etching displays the weld seam structure, the HAZ and the grain boundaries in the base material

TABLE 17: MACRO ETCHANT

3.6.4 MICROSCOPY

Different types of microscopic observations were carried out: microstructure analyses, surface analyses and crack analysis.

3.6.4.1 MICROSTRUCTURE ANALYSIS

This examination allows to study the microstructure of the material; grain boundaries, precipitates and material phases can be identified.

For microstructure analysis of welded specimens with a light optical microscope (LOM), the requested area was cut and embedded in mounting resin. Because of the size of the EBW seams they mostly could not to be embedded. Next, the samples were grounded with silicon carbide papers (grit 80, 120, 220, 320, 500, 800, 1200, 2400 and 4000). After grinding, the samples were polished with $3\mu m$ and $1\mu m$ diamond abrasive paste. The polished surfaces of the samples were ready for etching. To get an ideal result, the etchant and the etching time had to be chosen very carefully.

Different materials need different etchants, furthermore different etchants lead to different etching results. Serious problems occur in etching dissimilar welds, because of the different attack on the different materials. As a result of the extensive and successful etching experiments in the thesis of Bernhard Berger [9], the same etching agents and methods could be used in the experimental work of this thesis. The following table provides an overview of all etching agents.

Etching agent	Composition	Execution	Outcome
NITAL 5%	- 95 ml ethyl alcohol C_2H_6O - 5 ml nitric acid HNO_3	Immersing the specimen until the surface gets dull and the grain boundaries appear slightly CB2: \approx 7 min	Micro etching Displays the HAZ and the microstructure of the base material, weak etchant
Modified Lichte-negger & Bloech II	- 100 ml distilled water H_2O - 0.75 g ammonium hydrogendifluoride $(NH_4)HF_2$ - 0,90 g potassium metabisulfite $K_2S_2O_5$	Dunking the specimen until the surface gets a golden brown discolouration CB2: \approx 40 seconds	Colour etching Displays the microstructure of the HAZ and the base material
Aqua regia	- 50 ml hydrochloric acid HCl - 20 ml nitric acid HNO_3 - 20 ml glycerin	Heating up the etchant to 50° C; dunking the specimen until the welding zone appears slightly A625: \approx 2 minutes	Micro etching Displays the microstructure of the welding seam
-	- 50 ml ethyl alcohol C_2H_6O - 50 ml hydrochloric acid HCl - 5 ml hydrogen peroxide H_2O_2	Dunking the specimen until the grain boundaries in the base material appear A625: \approx 3 minutes	Micro etching Displays the microstructure of the base material Macro etching Displays the weld seam structure

TABLE 18: OVERVIEW ETCHANTS

For all dunking etchings, a steady movement between the etchant and the specimen is necessary to ensure a uniformly acid attack of the whole surface.

3.6.4.2 FRACTURE SURFACE ANALYSIS

Surface analysis was done on surfaces of welding failures (cracks, cavities, bead inhomogeneities) and fracture surfaces after the mechanical tests

To analyse a crack surface, microscopes with a high depth of field are required. Within this thesis a scanning electron microscope (SEM) and a stereo microscope (SM) were used. Those microscopes have the ability to get a three dimensional view of the fracture surface. These observations do not require any specific preparations. The surfaces just had to be cleaned with alcohol in an ultrasonic bath and dried afterwards.

3.6.4.3 CRACK INVESTIGATION

The appearance of many cracks in the CB2 master study led to a crack investigation. To improve the following welds, the sort of crack had to be identified to draw conclusions about the acting mechanism based on the texture of the fracture.

For this study two welding seams were chosen in order to be reviewed, as all cracks are located similarly in the middle of the fusion zone and look the same. To open the cracks a four millimetres slice was cut off the block. Next, the samples were cooled down in liquid nitrogen for several seconds and subsequently were broken apart to reveal the fracture surface. After cleaning in an ultrasonic alcohol bath, crack surfaces were investigated using the stereo microscope and the SEM.

3.6.5 EDX ANALYSIS

The energy dispersive X-ray spectroscopy (EDX) is a micro analytical technique for the chemical characterisation of a sample. Scanning can be done in different modes. In the point mode the different elements in one spot are detected; in the line mode the qualitative variation of the elements along a line are detected; and in the mapping mode the qualitative variation of the elements inside a scanned area can be displayed [64], [65].

In this thesis the line scan and the mapping mode were used to investigate the distribution of the elements in the fusion zone of the dissimilar joints to evaluate dilution. The sample preparation is equal to the preparation for the microscopy.

3.6.6 HARDNESS TEST

According to EN ISO 15614-1 [61] and EN ISO15614-11 [63], a hardness test for every welding had to be done. The Vickers testing procedures based on the EN 1043-2 [66] standard, which specify the macro- and micro hardness test, was used. The hardness test is passed if the HV10 values are not above the maximum values according to EN ISO 15614-1 [61].

The hardness tests were done on a ground and polished cross-section of the welding seam.

3.6.6.1 HARDNESS LINE

Following EN 1043-1 [67], at least three individual hardness impressions in the base material, the heat affected zone (HAZ) and the welding have to be done. Due to the narrow fusion zone and the even smaller HAZ, it is recommended to reduce the test load from HV10 to HV1 [29]. This ensures a refined hardness line with more and smaller impressions in the requested areas.

The hardness test lines were made using an automated EMCO measuring system. The measurement lines were done horizontally and perpendicular to the beam direction in three positions: on the top, in the middle and on the bottom of the weld seam. The length of the hardness lines was at least four times the width of the seam, which leads to approximately 40 HV1 measuring points for every line. To have results comparable with the standard, HV10 hardness lines were made in addition. Using the same length, around 15 HV10 impressions were possible. The results can be illustrated as a hardness graph directly on the picture of the seam.

3.6.6.2 MICRO HARDNESS

The micro hardness testing was performed to identify different components in the microstructure due to their differences in hardness values. The test was done with the Vickers procedure and a test load of 0.2 Newton (HV0.02). The hardness values are not directly comparable to the standard Vickers according to DIN EN ISO 6507-1 but a qualitative judging of the different components and phases in the material can be made.

3.6.7 TENSILE TEST

The Tensile test according to EN ISO 15614-1 [61] and EN ISO15614-11 [63], permits to determine the static tensile strength of the weld. To pass this test, the welded specimens have to exhibit at least the tensile strength of the base material. For a dissimilar welding, the minimum acceptable value is the tensile strength of the weaker material.

For every joint welding, three tensile test pieces were taken to cover the whole depth of the welding [63] (see Figure 68 on page 44). The samples were taken across the seam with the fusion zone in the middle (Figure 73). The test pieces were machined according to DIN 50125 [68] in mode B.

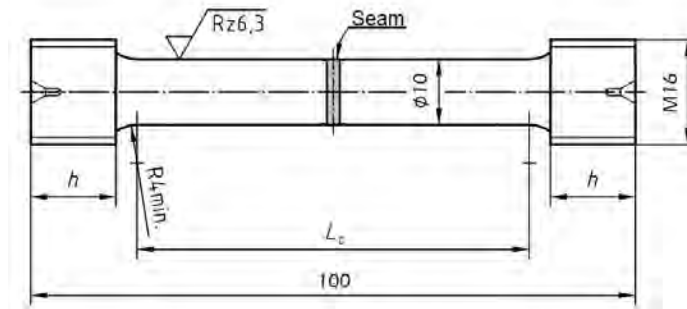


FIGURE 73: TENSILE TEST PIECE [68]

24 samples were tested (Table 19). Some of the dissimilar test pieces were in as welded (AW) conditions; the others were PWHT before the test. All trials were performed at room temperature. Table 19 lists up the amount of the test pieces and their classification.

		AW	PWHT
Similar	top	4	-
	centre	4	-
	bottom	4	-
Dissimilar	top	2	3
	centre	2	3
	bottom	2	3

TABLE 19: TENSILE TEST PIECES

3.6.8 CHARPY-V TEST

The Charpy test determines the amount of energy absorbed by a material during fracture.

According to ÖNORM EN ISO 15614-11 [63] the Charpy test has to be adapted to the present case. In this thesis the Charpy test was in dependence on ÖNORM EN 10045-1 [69] with reduced sample size. For every seam two sample batches (one out of the top of the seam and one out of the root) with three samples each were taken (see Figure 68 on page 44). The samples were made as **VWT** (V: Charpy-V notch; W: notch in the fusion zone; T: notch along the thickness; Figure 74 a.) and, despite it is not common for beam welding procedures because of the small HAZ, as **VHT** (V: Charpy-V notch; H: notch in the heat affected zone; T: notch along the thickness; Figure 74 b.) test pieces. The impact energy consumed for the welded test pieces must achieve the nominal values of the base material.

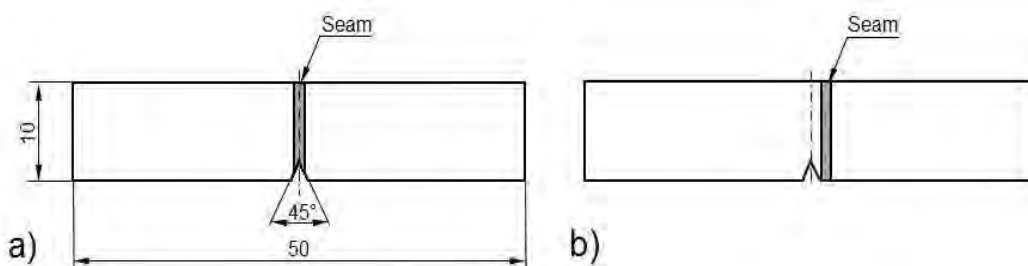


FIGURE 74: CHARPY TEST PIECES, A) NOTCH IN THE FZ, B) NOTCH IN THE HAZ

To position the notch correctly, all test pieces were first etched before notching (Figure 75).

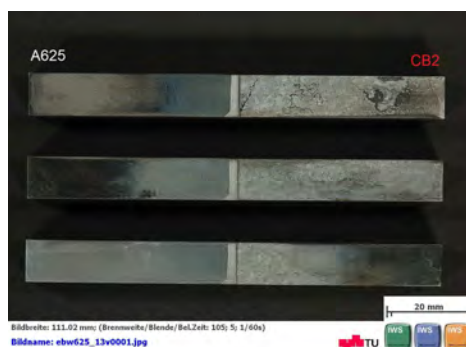


FIGURE 75: ETCHED CHARPY TEST PIECES

66 Charpy specimens were tested. Both, similar and dissimilar test pieces were made as VWT and as VHT. The notches for the dissimilar test pieces were made in both heat affected zones (A625 and CB2). Some of the dissimilar test pieces were tested in as welded condition the other were PWHT before the test. All trials were performed at room temperature. Table 20 lists the amount of the test pieces and their classification.

		AW		PWHT	
		VWT	VHT	VWT	VHT
Similar	top	6	6	-	-
	bottom	6	6	-	-
Dissimilar	top	3	3	9	6
	bottom	3	3	9	6

TABLE 20: CHARPY TEST PIECES

As prescribed in the standard, three Charpy test pieces lead to one result; the arithmetic mean of three equal test pieces has to be calculated.

3.6.9 SIDE BENDING TEST

The bending test is a so-called technological experiment. The test imitates processing operations and should determine whether the weld can endure this test without cracking. The test is passed if no failures longer than 3mm occur. Cracks that occur during the test on a samples edge are not included in the evaluation.

According to ÖNORM EN ISO 15614-11 [63], a bend test referred to ÖNORM EN 910 [70], which was replaced in 2009 with the EN ISO 5173 [71], had to be made. This standard allows the user to decide what kind of bend test is appropriate. For a sample thickness ≥ 12 mm, four side bend tests are suggested. The bending test in this thesis was made according to the tests performed in the thesis of Bernhard Berger [9]. The design of the test pieces is shown in Figure 76.

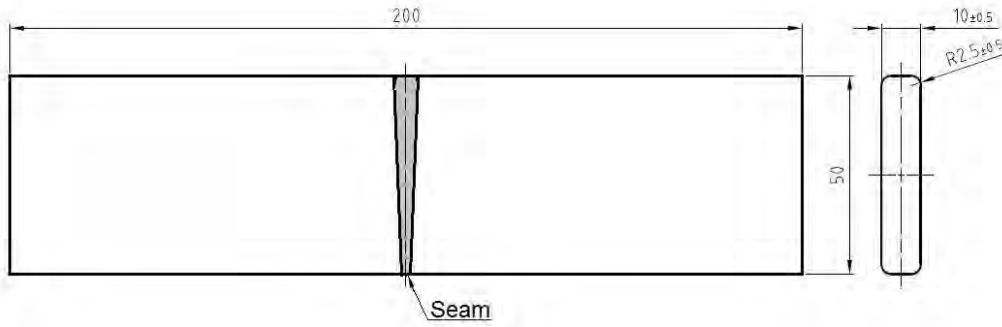


FIGURE 76: SIDE BEND TEST PIECE

Bernhard Berger describes in his thesis a sliding of the dissimilar test pieces during the side bend test to the nickel-base side. Therefore, “guided side bend test at voest alpine Stahl in Linz were performed. In this case the position of the seam is fixed to the position of the bending rod. During this thesis, unfortunately this machine was out of order so the side bend test had to be done with a conventional machine and a support plate. The diameter of the used bending rod was 40mm.

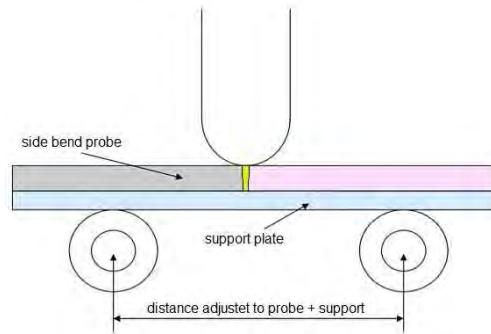


FIGURE 77: SUPPORTED SIDE BEND TEST

Nine pieces were tested. Some of the dissimilar test pieces were in AW condition while the other were PWHT before the test. All trials were performed at room temperature. Table 21 lists the amount of the test pieces and their classification.

	AW	PWHT
Similar	2	-
Dissimilar	2	5

TABLE 21: SIDE BEND TEST PIECES

4 RESULTS & DISCUSSION

This section provides all results of the performed experiments. The conclusions of the experiments are arranged in the same order as in the methods section; the results of the different investigation methods, mentioned in the previous subchapter, are integrated

4.1 BLIND WELDING

The results of the blind welding tests are the correct welding parameters which will be used for the subsequent joint welding. The parameter sets are related to the welding depth and analysed with Minitab®.

4.1.1 PILOT STUDY

The focus of these first welds was to find a rough parameter window and a safe working zone for the beam parameters. The target variable was the penetration depth (t) of the beam. The measured values are inscribed in bold numbers in the following tables. In the last column the energy input per length was calculated according to Equation 9. The energy input acts as an assistant dimension, which makes it possible to combine the three main welding parameters (I , U and v) and connect it directly to the beam penetration. The calculated input energy is only comparable when the same beam figure and the same figure amplitude are used. Below an explanation of the column labels is given.

- | | | | |
|------------------|-----------|--------------------------------|----------|
| ○ Welding number | # | ○ Figure amplitude | h |
| ○ Beam current | I | ○ Welding depth | t |
| ○ Welding speed | v | ○ Energy input per unit length | E |
| ○ Focal point | fp | | |

The welding trials performed in the pilot study and the reached depth is shown in Table 22.

#	I / (mA)	v / (mm/s)	t / (mm)	E / (kJ/cm)
1	105	15	29	8.4
2	105	5	45	25.2
3	205	5	68	49.2
4	205	15	48	16.4

TABLE 22: PARAMETERS PILOT STUDY

$$E = \frac{U \cdot I}{v}$$

EQUATION 9: ENERGY INPUT PER LENGTH

$$\text{Energy input per unit length } [E] = \text{kJ/cm}$$

$$\text{Acceleration voltage } [U] = \text{kV}$$

$$\text{Beam current } [I] = \text{mA}$$

$$\text{Welding speed } [v] = \frac{\text{cm}}{\text{s}}$$

Figure 78 shows an etched specimen. The welding seams carried out for the FFD pilot study are numbered from one to four (the non-marked welds do not belong to this study).



FIGURE 78: PILOT STUDY, MILD STEEL

Figure 79 shows the plot for two factor variables (I and v) and Figure 80 illustrates the results as a contour plot.

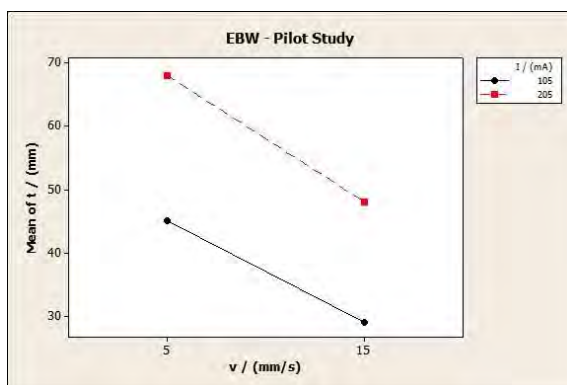


FIGURE 79: FACTOR PLOT PILOT STUDY

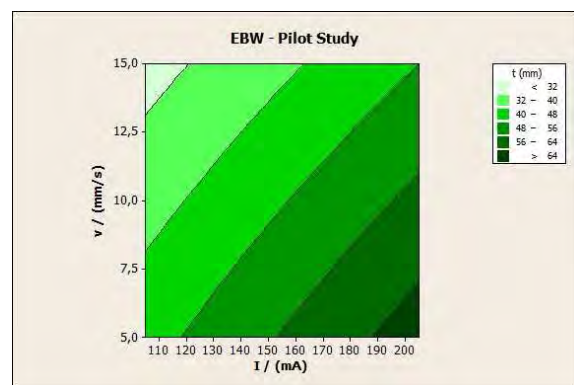


FIGURE 80: CONTOUR PLOT PILOT STUDY

Figure 79 shows two nearly parallel lines, so there is no significant interaction between the welding speed v and the welding current I . The contour plot shows which depth level is reached for which parameter combination. Each shade of green represents a certain penetration depth range.

Using these results, the parameters for the CB2 blind welding study could be defined. The localisation of the parameter box for the following blind welds was done geometrically. The leading parameter here was the 55mm depth line. The blind welding parameter area is located at the lower right in the contour diagram. This was done by reason of an easier setting of the machine at lower beam current. Besides, according to Schultz [29], a lower welding speed for nickel alloys is recommended. Figure 81 shows the inscribed parameter box in central composite design.

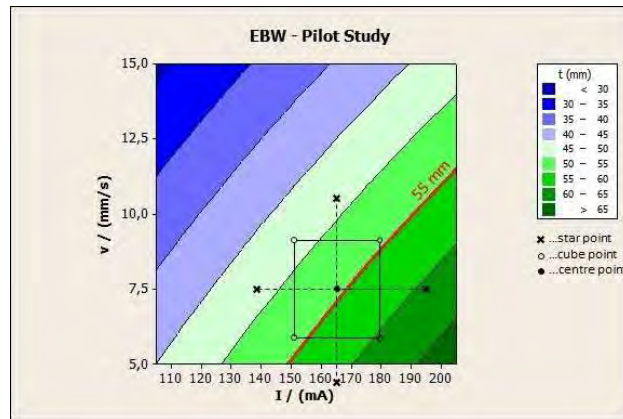


FIGURE 81: INSCRIBED MASTER STUDY BOX

4.1.2 TEMPERATURE MEASUREMENT

The measured temperatures, taken at 5mm and 15mm away from the weld centre line, are shown in the following two figures. Figure 82 shows the first 10 minutes of the measurement duration and Figure 83 displays the detail of the first 80 seconds of the experiment.

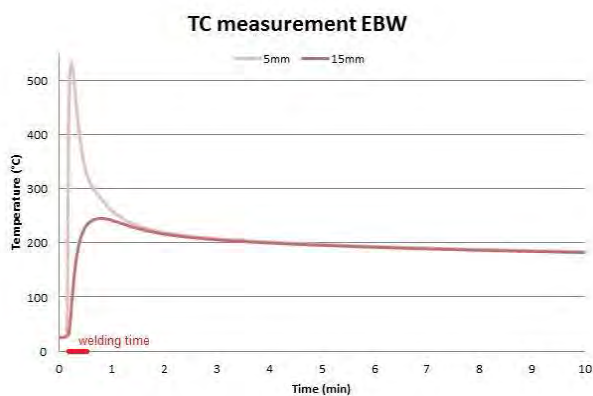


FIGURE 82: TEMPERATURE CURVE, 30 MINUTES

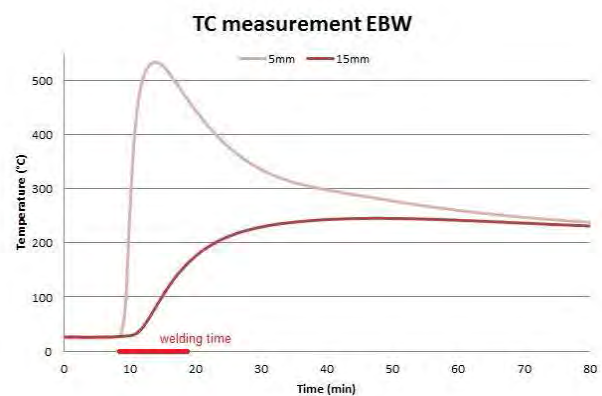


FIGURE 83: TEMPERATURE CURVE, 1 MINUTE

The start temperature of the block was 27°C; eight seconds after starting the measurement the welding started and lasted for ten seconds. The maximum temperature reached 5mm besides the welding was 533°C; it was recorded 1 second after the beam passed the thermocouple. 30 seconds later, the temperature dropped below 300°C. The second thermocouple, 15mm besides the weld, reached its top value of 245°C, 40 seconds after the welding started. About one minute after the experiment both thermocouples show the same temperature level. Then the cooling rate became very small. The last measured value after 30 minutes was 160°C.

This experiment shows clearly the small temperature field of the EBW procedure.

4.1.3 BLIND WELDING CB2

The results of the first two CB2 blocks were not only used to determine the welding depth but also to evaluate the seam geometry or any occurring welding defects.

Table 23 shows the parameters for all trials within this experiment. The target variable is the welding depth (t). The last column contains the calculated energy input per length (E).

#	I / (mA)	v / (mm/s)	fp / (mA)	h / (mm)	t / (mm)	E / (kJ/cm)
1	180	5.50	-30	1.00	64.0	39.27
2	165	7.25	-15	0.75	52.3	27.31
3	180	5.50	-30	0.50	68.0	39.27
4	180	9.00	-30	1.00	51.0	24.00
5	150	9.00	0	1.00	43.2	20.00
6	150	9.00	0	0.50	46.9	20.00
7	180	9.00	0	1.00	49.6	24.00
8	165	7.25	-15	0.75	55.8	27.31
9	150	5.50	0	0.50	59.0	32.73
10	165	7.25	-15	0.75	55.9	27.31
11	180	9.00	0	0.50	53.7	24.00
12	180	5.50	0	1.00	61.4	39.27
13	150	9.00	-30	1.00	47.6	20.00
14	150	5.50	-30	0.50	66.0	32.73
15	180	9.00	-30	0.50	59.2	24.00
16	150	5.50	-30	1.00	66.2	32.73
17	180	5.50	0	0.50	66.9	39.27
18	150	5.50	0	1.00	56.8	32.73
19	150	9.00	-30	0.50	53.9	20.00
20	165	7.25	-15	0.75	55.7	27.31
21	165	7.25	-15	0.25	57.6	27.31
22	165	7.25	-45	0.75	57.2	27.31
23	165	3.75	-15	0.75	72.7	52.80
24	195	7.25	-15	0.75	65.3	32.28
25	135	7.25	-15	0.75	48.7	22.34
26	165	7.25	15	0.75	48.6	27.31
27	165	7.25	-15	1.25	55.0	27.31
28	165	7.25	-15	0.75	58.35	27.31
29	165	10.75	-15	0.75	50.8	18.42
30	165	7.25	-15	0.75	58.5	27.31

TABLE 23: PARAMETERS BLIND WELDING CB2, BLOCK 1 & 2

Figure 84 and Figure 85 show the first two cut and etched CB2 blocks. The welding seams are labelled with their number (# column, in the table). Weld shape and depth are documented for each experiment. The welds show a dendritic structure perpendicular to the beam. Several kinds of welding defects, visible to the naked eye, can be observed (cracks, cavities and irregular seam shape).



FIGURE 84: CROSS SECTION OF CB2 BLIND WELDING, BLOCK 1

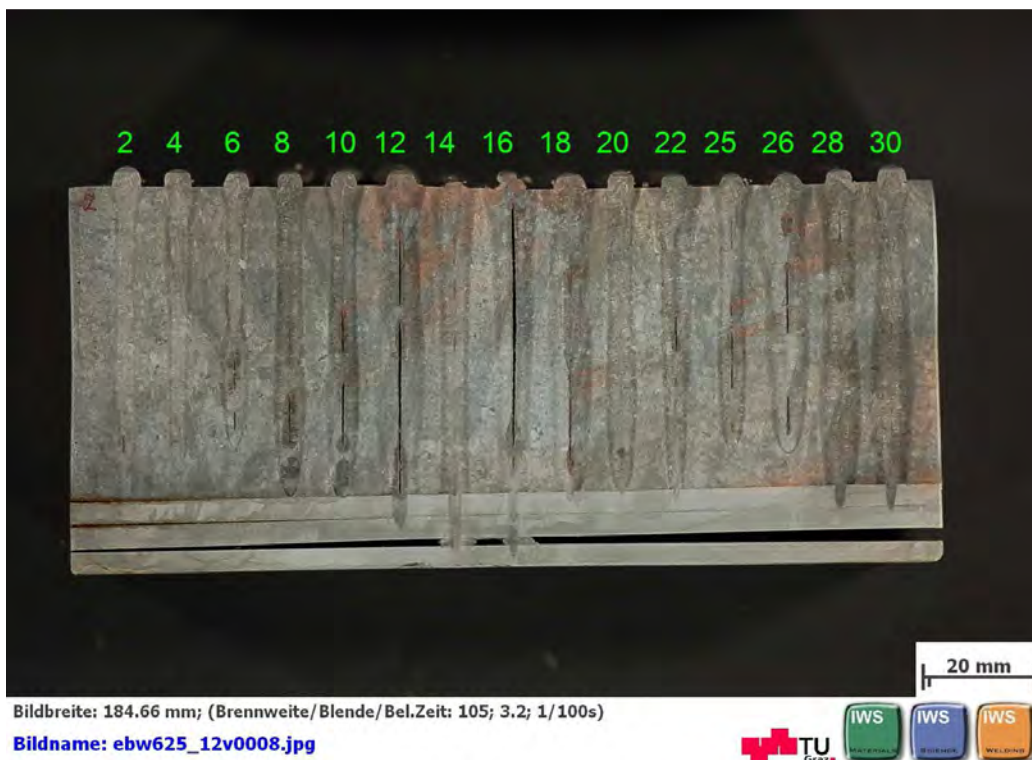


FIGURE 85: CROSS SECTION OF CB2 BLIND WELDING, BLOCK 2

The first and most important analysis was to measure the depth t of every weld. The welding depth was imported to the Minitab software to complete the data for the analysis procedure. Welding #23 was not suitable for analysing because the beam broke through and the molten metal drained out.

The main effect plot (Figure 86) compares the relative strength of the welding parameters I , v , fp and h on the target variable t . The horizontal line in every plot represents the mean value of this effect.

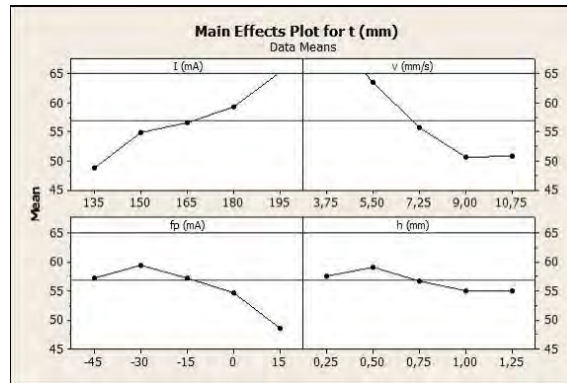


FIGURE 86: MAIN EFFECT PLOT BLIND WELDING CB2, BLOCK 1 & 2

The beam current I , the welding speed v and the focus position fp show a clear effect on the welding depth. The effect of I and v is quite linear; however, the effect of the welding speed nearly vanishes between 9 and 10.75mm/s. The focal point has a strong effect at positive values (the welding depth decreases). The maximum impact of fp is at approximately -30mA, here the maximum depth was reached. For a circular beam figure its amplitude h shows just a slight influence on the penetration depth.

The following contour plots (Figure 87 till Figure 90) link certain penetration levels (shaded in green and blue) to their parameter combinations. Due to the fact that during this experiment four variable parameters were used, several contour plots are required to display the process behaviour. Figure 87 shows the penetration depth t , expressed as a contour plot of the welding speed v over the welding current I , at middle settings of the other two parameters (focus fp and oscillating amplitude h). Figure 88 contains the same information for higher values of focus and oscillation amplitude.

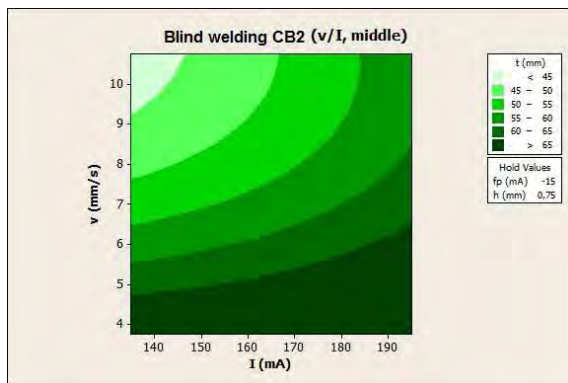


FIGURE 87: CONTOUR PLOT CB2 (V/I, M)

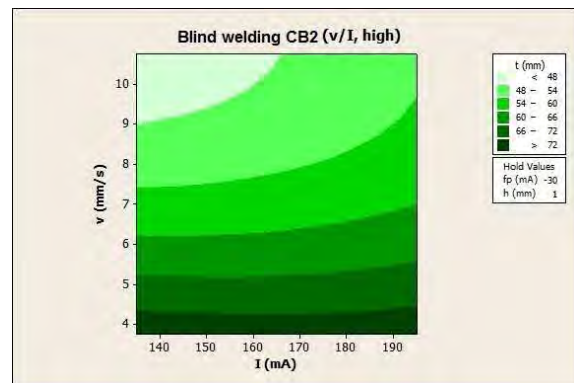


FIGURE 88: CONTOUR PLOT CB2 (V/I, M)

Figure 89 and Figure 90 show the penetration depth t , expressed as contour plot of oscillation amplitude h , over focal position fp at constant settings of I and v . Varying the oscillation amplitude at this small range (0mm up to 1.25mm) at middle settings of I and v (Figure 89), h has nearly no effect on the penetration depth unlike to the focal position. Setting the focal point below the surface of the workpiece (negative values), a higher penetration can be reached.

At a higher level of the holding parameters, this effect has its inflexion point between -30mA and -20mA (Figure 90) and also h get influence on t (t decrease when h increase).

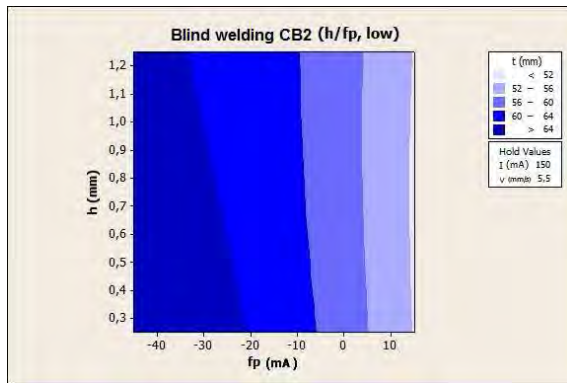


FIGURE 89: CONTOUR PLOT CB2 (H/FP)

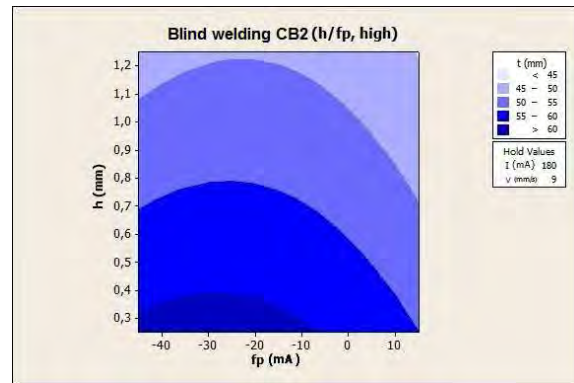


FIGURE 90: CONTOUR PLOT CB2 (H/FP)

Owing to the many welding factors a pivot table in Excel was made to sort the welding seams by two additional attributes: crack and waist. “Crack” indicates a crack in the seam. “Waist” was used to mark the weld if it has an inaccurate geometry (no homogenous nail shape). Welding #9 and welding #17 in Figure 85 show such a failure. By sorting the seams after their different attributes, it turned out that the focal position is very important for the welding geometry; when using a focal point under the welding surface (at least -15mA), no waist has developed in the seam. The oscillation amplitude also has an effect on waist developing; using a high oscillating amplitude ($h=1\text{mm}$), the developing waist can be suppressed.

The inaccurate geometry of some welds (“waist-shape”) can be ascribed to a wrong focal point. For further experiments the best evaluated value (-30mA) was kept constant. These welding results also showed that at higher oscillating amplitudes, the failure rate for the CB2 decreases.

Since no obvious connection between the used parameters and the occurred cracks could be found, an additional crack investigation had to be made.

4.1.3.1 CRACK INVESTIGATION

In Figure 91 the two testing positions for the crack investigation are displayed. Welding #11 shows a cavity with a crack; #27 shows a straight sharp vertical crack in the middle of the fusion zone.

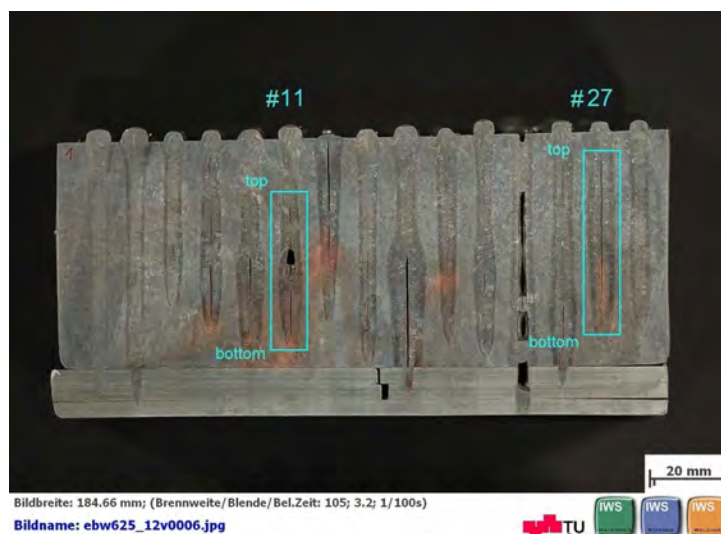


FIGURE 91: CRACK INVESTIGATION, SPECIMEN POSITIONS

All cracked surfaces show the same topography; a fine grained surface with no asperities. The surface shows typical annealing colours, the area of the forced brittle fracture is metallic silver coloured.

Figure 92 and Figure 93 show welding #11. The crack surface can be clearly differed from the cavity surface. The cavity surface has a smoother surface and features several solidification lines.



FIGURE 92: #11; CAVITY, MACRO VIEW



FIGURE 93: #11; CAVITY, MICRO VIEW

Figure 94 till Figure 104 show the crack in welding #27. Figure 94 shows the macroscopic picture.



FIGURE 94: #27; CRACK SURFACE OVERVIEW

The macroscopic pictures of the crack show coloured surfaces despite no annealing colours can occur in vacuum. Therefore the hot crack surface had contact with air after flooding the chamber.

Figure 95 shows the top area viewed through a stereo microscope. A crystalline surface is recognisable. A further examination was done with the SEM. Figure 96 shows an overview of the same area. On Figure 97 and Figure 98 a small zone is imaged with higher magnification.



FIGURE 95: #27; TOP AREA, SM

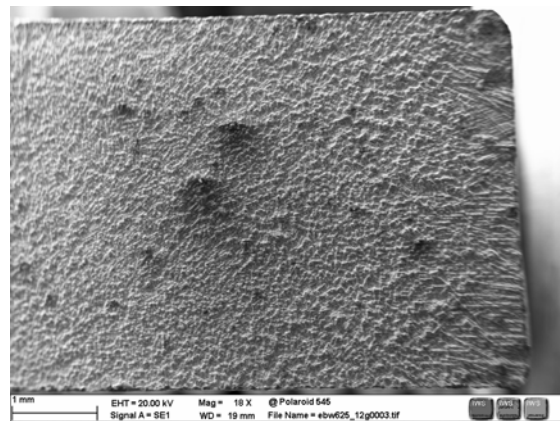


FIGURE 96: #27; TOP AREA, SEM_1

The surface has no sharp edges or tips. Especially in Figure 98, viewed at high magnification, the smooth randomized structure is well visible. This is characteristic for failures in the presence of liquid.

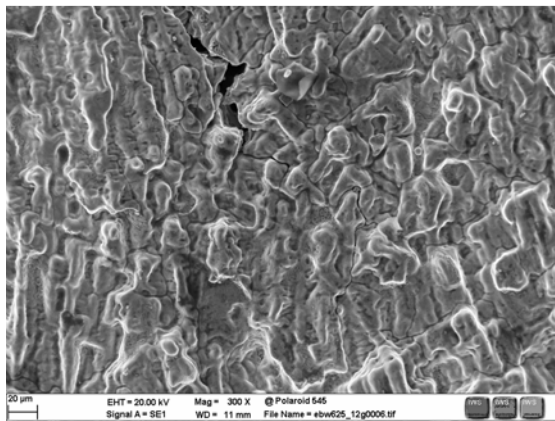


FIGURE 97: #27; TOP AREA, SEM_2

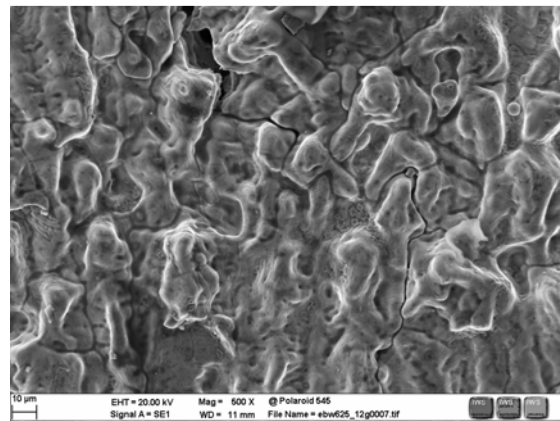


FIGURE 98: #27, TOP AREA, SEM_3

The following pictures (Figure 99 till Figure 102) show the surface structure of the bottom side of the crack (left area in Figure 94 on page 58). This structure exhibits a more dendritic structure. Despite the diverse topography compared to the top area of the crack the surface is also smooth, which is an indicator for hot cracking.

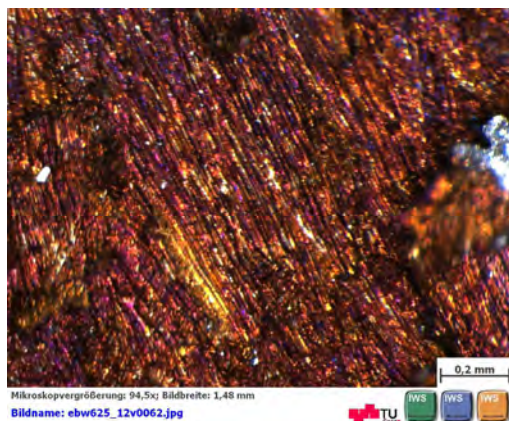


FIGURE 99: #27; BOTTOM AREA, SM

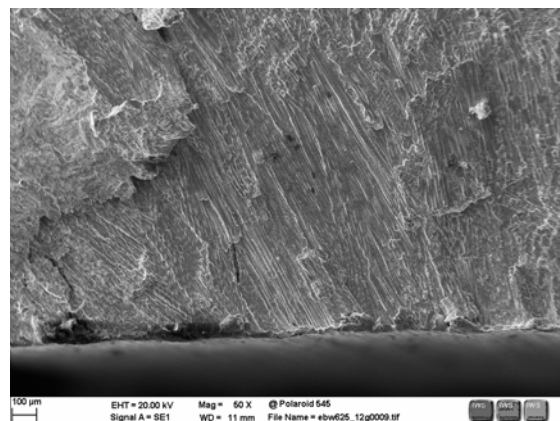


FIGURE 100: #27; BOTTOM AREA, SEM_1

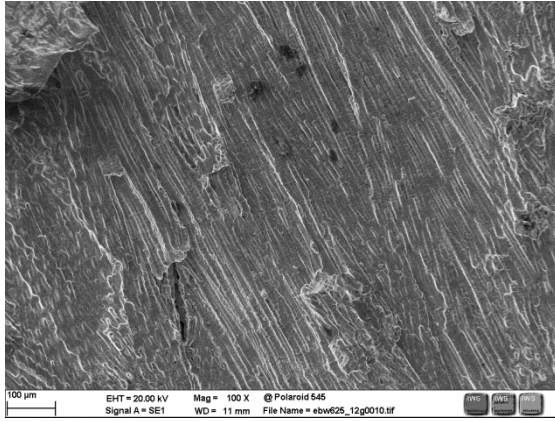


FIGURE 101: #27; BOTTOM AREA, SEM_2

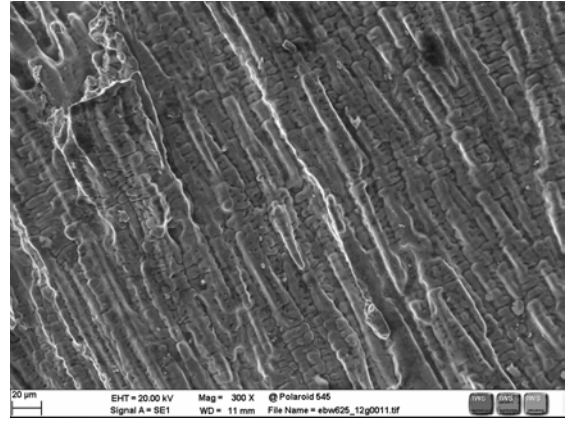


FIGURE 102: #27; BOTTOM AREA, SEM_3

For comparison, the brittle fracture surface (the small metallic silver coloured island seen in Figure 94) was also investigated. This surface, illustrated in the next two pictures below, is clearly different to the previous once. The surface looks transcrySTALLINE with evident edges.

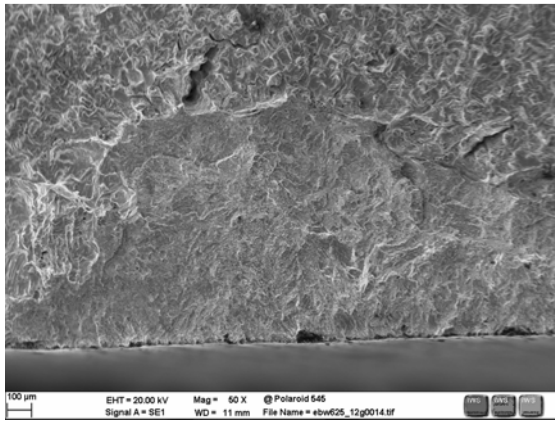


FIGURE 103: #27; BRITTLE FRACTURE, SEM_1

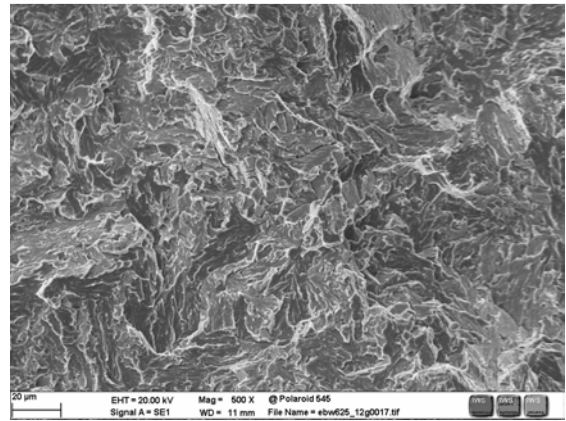


FIGURE 104: #27; BRITTLE FRACTURE, SEM_2

For the second two blocks the same test piece geometry was used for much less trials. This ensures no influence between the welding seams in a way of heat input and thermal stresses. Additionally, longer breaks between welding were made to get nearly the same starting temperature for every welding. In Table 24, all performed trials are listed. A double x marks a failed welding.

#	$I / (\text{mA})$	$v / (\text{mm/s})$	$h / (\text{mm})$	$t / (\text{mm})$	$E / (\text{kJ/cm})$
1	150	8.00	0.50	51.0	22.5
2	160	8.75	0.50	52.5	21.9
3	170	8.50	0.75	54.0	24.0
4	160	8.00	0.75	54.3	24.0
5	150	7.50	0.75	51.5	24.0
6	180	6.75	1.00	xx	32.0
7	165	6.50	1.00	xx	30.5
8	150	6.25	1.00	55.9	28.8

TABLE 24: PARAMETERS BLIND WELDING CB2, BLOCK 3 & 4

Welding #6 and #7 failed completely. The beam broke through the backing batten; welding #3 has a 1mm long crack in the root. All other welds were successful. Figure 105 shows a cross section of block three. In Figure 106, welding #8 etched with Adler etchant is shown.



FIGURE 105: BLIND WELDING CB2, BLOCK 3



FIGURE 106: BLIND WELDING CB2, BLOCK 4, ETCHED

To affirm that the whole welding was done without failures, cross sections at three different positions in both blocks were investigated (Figure 107). No other welding defects could be observed.

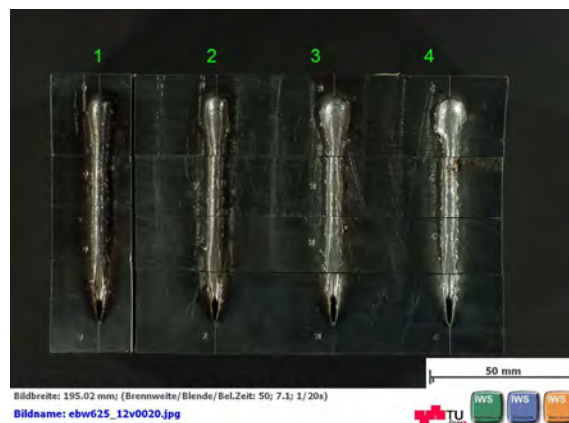


FIGURE 107: BLIND WELDING CB2, BLOCK 3, TOP VIEW 1

Furthermore, the penetration for every weld was measured on every cutting surface to detect a possible spiking. The depth varies only within 1.5mm, no distinctive spiking occurred. The welding seams show a very regular seam top face (Figure 107).

The statistical evaluation in central composite design worked quite well. The expected depth of welds in the third block correlated with the predicted results of the Minitab Software.

RÉSUMÉ CRACK INVESTIGATION

On the pictures of the first two welded blocks (Figure 84 and Figure 85) a lot of cracks in the fusion zone are visible. In accordance with the Schäffler-diagram [72] the CB2 tend to hardening cracks (see Figure 108).

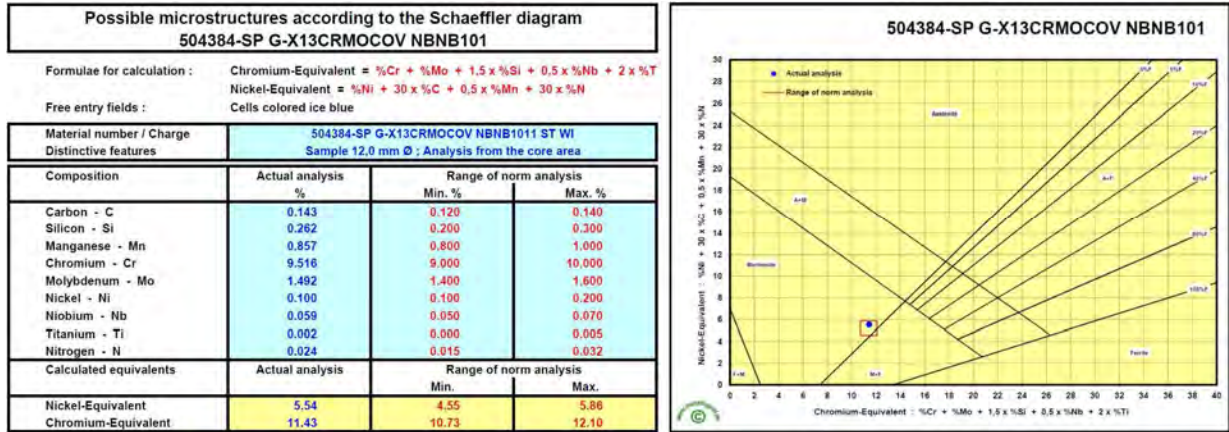


FIGURE 108: SCHÄFFLER DIAGRAMM CB2 [72]

However, the SEM investigation (Figure 97, Figure 98, Figure 101 and Figure 102) showed a smooth surface which is typically for *hot cracks*. Figure 103 and Figure 104 clearly show the difference to a brittle crack surface.

4.1.4 BLIND WELDING A625

This study of the A625 has the same goals as the CB2 blind welding study, namely, to find out how deep the penetration of the beam is and how the seam geometry develop with different parameter combinations. Due to the results received from CB2 blind welding trials, the focus position was kept constant at -30mA. In Table 25 the parameters for the trials can be found. The measured depth (*t*) is printed in bold letters; a double x marks a failed welding.

#	I / (mA)	v / (mm/s)	h / (mm)	t / (mm)	E / (kJ/cm)
1	165	7.5	0.5	62.5	26.4
2	150	5.0	0.5	64.0	36.0
3	165	7.5	0.5	63.0	26.4
4	180	5.0	0.5	xx	43.2
5	165	5.0	0	xx	39.6
6	165	10	0	55.0	19.8
7	180	7.5	0	62.4	28.8
8	180	7.5	1.0	63.5	28.8
9	165	10.0	1.0	49.0	19.8
10	165	5.0	1.0	61.0	39.6
11	150	7.5	1.0	54.5	24.0
12	150	7.5	0	53.3	24.0
13	150	10.0	0.5	55.0	18.0
14	180	10.0	0.5	56.5	21.6

TABLE 25: PARAMETER BLIND WELDING A625, BLOCK 1 & 2

The welding seams are labelled with their number (# column in the table) and can be seen in Figure 109 and Figure 110. Welding #5 and #4 are not used for evaluation.

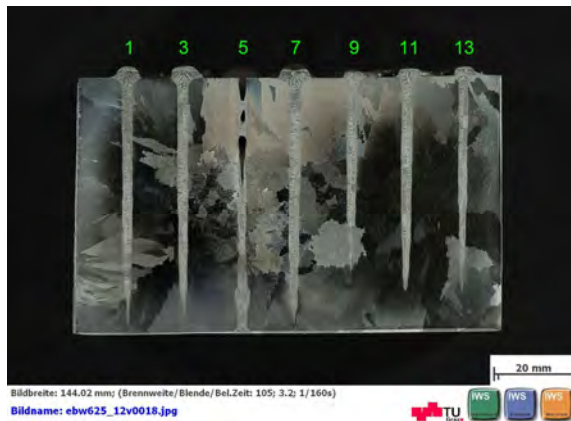


FIGURE 109: BLIND WELDING A625; BLOCK 1



FIGURE 110: BLIND WELDING A625; BLOCK 2

After the macroscopic preparation all welds with feasible parameters appear without failures and a clean seam shape. The different seam widths can be directly related to the different oscillation amplitudes.

The welding process itself looked very turbulent, especially by using higher oscillation amplitudes, the welding pool was agitated and weld spatter escaped from the weld pool. Figure 111 and Figure 112 confirm this point. All welds done with an amplitude of $h=1$ mm have an inhomogeneous seam top face (#8, #9, #10 and #11). However, this did not cause any failure in the seam itself.



FIGURE 111: BLIND WELDING A625, BLOCK 1, TOP VIEW 1

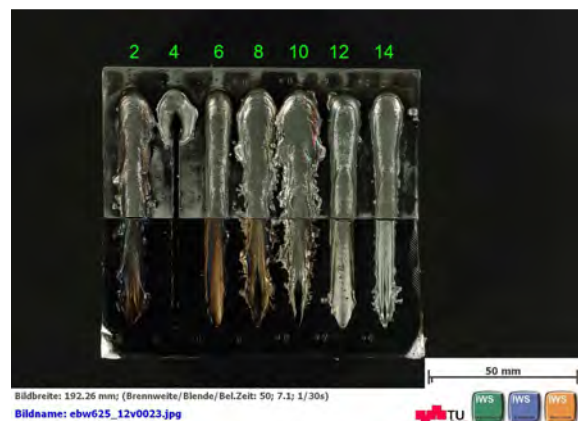


FIGURE 112: BLIND WELDING A625, BLOCK 2, TOP VIEW 2

The main effects plot in Figure 113, shows pretty much the same results as the plot for the CB2 (Figure 86). There is an obvious effect of the beam current and the welding speed. Strangely, a maximum beam penetration is shown at the oscillating amplitude of 0.5mm. This can be considered as the best oscillation amplitude to form a steady and stable keyhole in the A625.

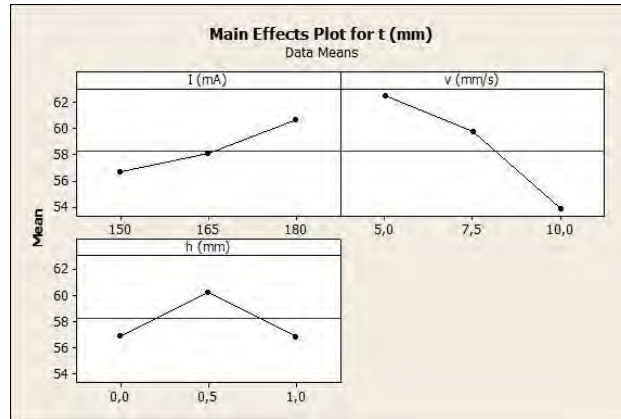


FIGURE 113: MAIN EFFECT PLOT BLIND WELDINGS A625, BLOCK 1 & 2

Another graphical representation of the results is shown in the two contour plots in Figure 114 and Figure 115. They connect the penetration values to the varied parameters. The different developments of the penetration curves in the plot, declining trend of the depth curves in the A625 plot (Figure 114) and the inclining trend of the depth curves in the CB2 plot (Figure 87) do not have to be attributed to the different materials. This distinction can be related to the distinct DOE, the BBD trials do not cover a check of the adequacy of the quadratic model of the experiment.

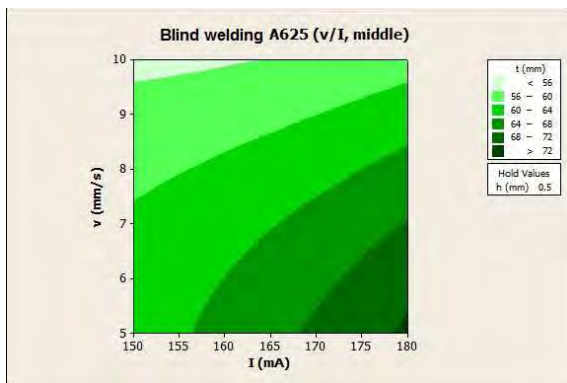


FIGURE 114: CONTOUR PLOT (V/I) A625, BLOCK 1 & 2

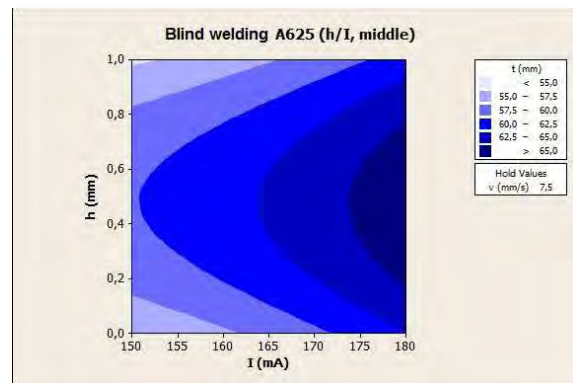


FIGURE 115: CONTOUR PLOT (H/I) A625, BLOCK 1 & 2

For the following experiments the parameter was also drawn in contour plot. In Figure 116, the inscribed box on the upper left marks the parameter window for the experiments with the third nickel based alloy block.

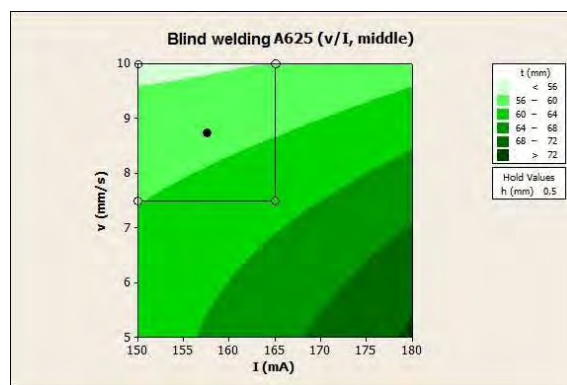


FIGURE 116: PARAMETER BOX FOR A625, BLOCK 3

This third A625 block, which measures 50mm in thickness, was supported with a mild steel backing plate. The welds were made with the parameters listed up in Table 26; here the oscillation amplitude was also kept constant at 0.5mm.

#	I / (mA)	v / (mm/s)	t / (mm)	E / (kJ/cm)
1	150.0	10.00	49.7	18.0
2	150.0	7.50	53.8	24.0
3	157.5	8.75	53.6	21.6
4	165.0	10.00	54.5	19.8
5	165.0	7.50	57.9	26.4

TABLE 26: PARAMETERS A625, BLOCK 3

The welded block was cut twice to investigate the welds on these four cutting surfaces. No welding failures could be detected but the penetration depth was found to be very inconsistent. Table 27 shows the values of the depth measurement with the calculated mean and the maximum divergence Δt .

Measuring	Welding seam				
	1	2	3	4	5
1	49.7	54.9	51.2	50.6	57.8
2	47.1	52.3	55.2	56.3	58.9
3	48.0	56.1	52.9	55.6	59.4
4	54.0	52.0	55.0	55.4	55.4
<i>Mean</i>	<i>49.7</i>	<i>53.8</i>	<i>53.6</i>	<i>54.5</i>	<i>57.9</i>
<i>Δt</i>	<i>6.9</i>	<i>4.1</i>	<i>4.0</i>	<i>5.7</i>	<i>4.0</i>

TABLE 27: ARITHMETIC MEAN PENETRATION DEPTH SIMILAR WELDING A625, BLOCK 3

The variation of the penetration depth is quite high, despite the measuring surfaces one and two and furthermore three and four are only 3mm distanced (cut width of the saw). A distinctive spiking effect is observed in this test. This cognition is in line with the unstable weld pool.

Figure 117 shows the contour plot of this, in FFD performed study in the third A625 block. As input data for Minitab® the mean values of the depth were used.

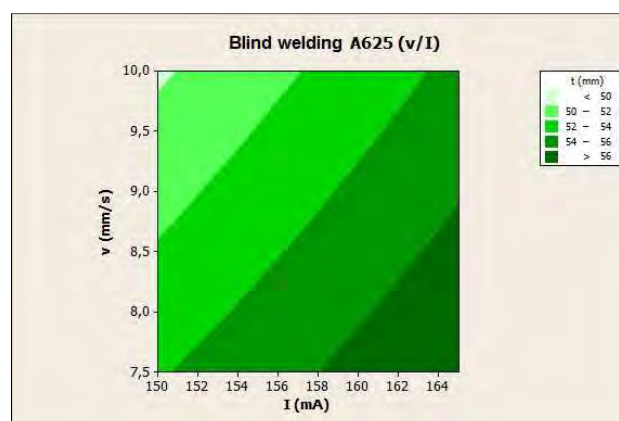


FIGURE 117: CONTOUR PLOT (V/I) A625, BLOCK 3

After cutting and etching the welded block was left for several days to give the mild steel time to oxidise. Oxidation took place under atmosphere; the etched surface accelerated this process. After oxidation, the macroscopic pictures displayed in Figure 118 and Figure 119 reveal the material mixing between the block and the backing plate in the root of the weld.



FIGURE 118: A625 BLOCK 3, MATERIAL FUSION (1)



FIGURE 119: A625 BLOCK 3, MATERIAL FUSION (2)

RÉSUMÉ BLIND WELDING

To sum up the results of the blind welding studies, it has to be said that proper working parameters for each material could be found. Admittedly, both materials show disparities in the preferred welding power to reach a welding depth of 55mm. Compared to the CB2 steel, the nickel based material needs less welding energy. Also a contrary reaction on the used oscillation amplitude could be observed; the CB2 prefers a high oscillation, the A625 in contrast becomes even more turbulent with increasing oscillation amplitude.

To achieve a successful joint in dissimilar welding a compromise for the varying parameter has to be found.

4.2 JOINT WELDING

This chapter contains the results of phase three (joint welding) and four (pWPS test) of the welding experiments. All welds were performed with joint samples (see Figure 64). Here not only the geometry of the seams was investigated but also their microstructure and furthermore mechanical properties were evaluated.

4.2.1 SIMILAR WELDING A625

Here, the results of the similar joint welding are presented. Table 28 lists up the reached welding depth together with the parameters of all A625 similar joint trials.

#	ID	I / (mA)	v / (mm/s)	h / (mm)	t / (mm)	E / (kJ/cm)
1	S14/15	165	10.0	0.5	59	19.8
2	S27/28	165	10.0	0.5	59	19.8
3	S16/17	165	7.5	0.5	xx	26.4
4	SS29/30	165	7.5	0.5	xx	26.4
5	S7/8	150	9.0	0.5	55	20.0
6	S3/4	165	11.0	0.5	56	18.0
7	S1/6	180	15.0	0.5	49	14.4
8	S9/10	165	100	1.0	51	19.8
9	SS26/31	185	11.0	0.5	59	20.2
10	S6/10B	165	10.5	0.5	54	18.9
11	S11/12B	165	100	0.5	60	19.8

TABLE 28: SIMILAR JOINT WELDING PARAMETERS

Trial one and two show a high penetration compared to the blind welding experiments; trial three and four failed because of too high energy input. For the same energy input the reached penetration depth is different; the small gap between the parts could be the reason for this, so the beam energy in joint welding had to be reduced. After readjusting the parameters, the welding procedure was without any problems.

The observed spiking in the A625 blind welding study was not a problem in the joint welding experiments. With the use of a 10mm backing batten the joint was welded completely and no root failures could be found.

4.2.1.1 MICROSTRUCTURE

In none of the performed joint welds cavities or cracks were observed. Figure 120 shows one representative cross section macro etching of a similar joint. The shape of the seam is steady and the finer grain in the fusion zone is visible with the naked eye. Figure 121 shows the fusion zone in higher magnification; the dendritic structure is clearly visible.



FIGURE 120: A625, MACRO; S14/15



FIGURE 121: A625 BM / FZ; S14/15 (1)

In Figure 122 and Figure 123 the area next to the fusion zone is displayed. The fusion zone is clearly different compared to the base material; no distinctive heat affected zone is visible. But in Figure 123 a grain boundary can be observed which extends into the fusion zone. Looking again at Figure 122 in the area where the boundary enters the FZ (green rectangular), a small (approx. 50 μ m wide) layer can be observed with a slight differ microstructure compared to the FZ.



FIGURE 122: A625 BM / FZ; S14/15 (2)

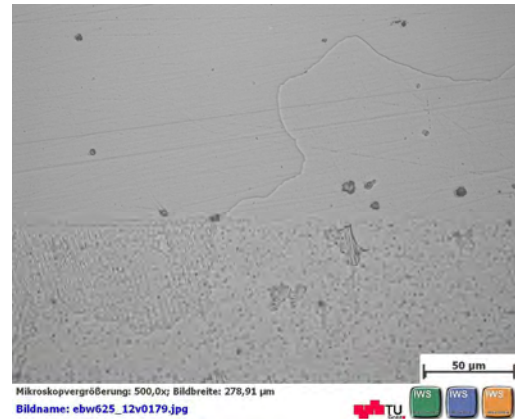


FIGURE 123: A625 BM / FZ; S14/15 (3)

To identify the solidification process, aqua regia was used as etchant. Figure 124 (seam top) and Figure 125 (near the seam root) show the now visible solidification lines. These lines result from varying solidification rates [29].



FIGURE 124: CROSS SECTION, TOP; S27/28



FIGURE 125: CROSS SECTION, CENTRE; S27/28

Solidification takes place perpendicular to the beam (see dendrites orientation in Figure 121), this leads to a clash of opposite solidification directions in the centre of the seam. In a horizontal section (top view) through the seam, these circumstances appear as periodic rings (Figure 126). Choosing a welding speed, which is too high, makes these solidification irregularities gather in the seam centre and leads to a loss of strength of the joint. Such a welding failure is illustrated in Figure 127 (horizontal section, $v=30\text{mm/s}$) where a crest has developed in the middle of the seam.



FIGURE 126: HORIZONTAL SECTION; S3/4

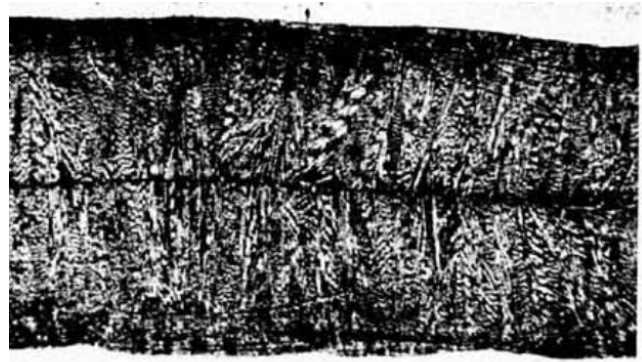


FIGURE 127: HORIZONTAL SECTION WITH DISCONTINUITY [29]

To ensure that the seam centre is free from defects another cross section was investigated with the light microscope (Figure 128 and Figure 129). In both pictures no flaws were detected.



FIGURE 128: CENTRE LINE FUSION ZONE; S3/4 (1)



FIGURE 129: CENTRE LINE FUSION ZONE; S3/4 (2)

4.2.1.2 HARDNESS

Several hardness lines (Vickers procedure) in different positions were performed. The base material shows hardness around 160HV10. From about 2mm from the fusion zone, the hardness progressively increases to reach a maximum of about 220HV in the fusion zone (Figure 130 and Figure 131). This hardness peak is developed more explicitly near the root of the welding (see Figure 132).

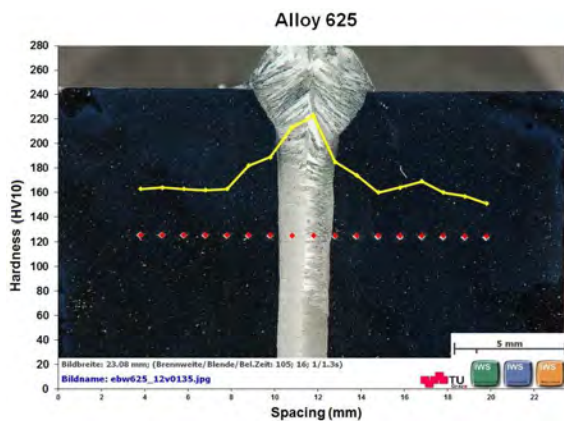


FIGURE 130: HARDNESS LINE HV10, TOP; S14/15



FIGURE 131: HARDNESS LINE HV10, CENTRE; S26/31

Figure 132 and Figure 133 show a refined measurement with lower load (HV1). The absolute values compared to HV10 are higher (up to 258HV1) but the evolution of the hardness is the same and no critical value (above 350HV) is reached. The increase of the hardness in the seam can be explained by the grain refinement.

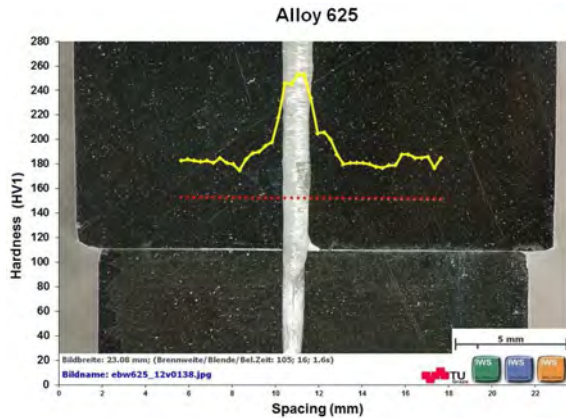


FIGURE 132: HARDNESS LINE HV1, ROOT; S14/15

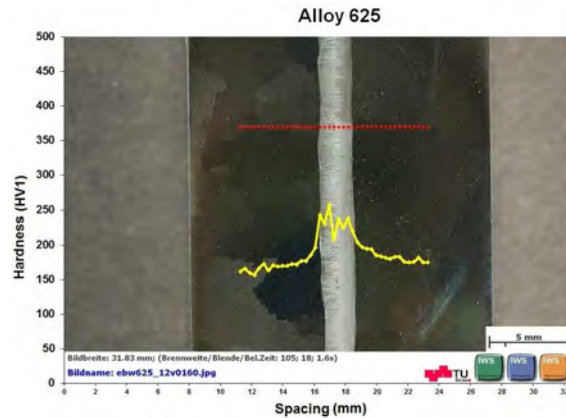


FIGURE 133: HARDNESS LINE HV1, CENTRE; S26/31

4.2.1.3 MECHANICAL TESTING

The **tensile tests** of the similar welds exhibit clearly the behavior of a very coarse grained material. A homogenous elongation does not exist due to large grain size. The former round shaped tensile probe becomes elliptic. A flaky and stepped surface shows the deformation inside one grain along the gliding planes due to the shear strength.

All tested specimen broke in the base material. Figure 134 shows three specimens after the test.



FIGURE 134: TENSILE TEST PIECES, A625 SIMILAR; S3/4

In Table 29 the measured values are listed (Figure 135 shows the related tensile curves). The average fracture of strain is above 50% and the average tensile strength is 490MPa. The tensile strength values of the welded joints are in the range of the base material's values and always higher than the nominal value ($R_{m, nom}=400\text{MPa}$; $R_{m, act}=475\text{MPa}$; see Table 6 on page 34).

Legend	Nr	Labelling	R _m MPa	F _m kN	L ₀ mm	S ₀ mm ²	A _{manuell} %	d ₀ mm
■	1	S3/4_DL	492	38.65	50.00	78.54	66.0	10
■	2	S3/4_ML	525	41.24	50.00	78.54	66.0	10
■	3	S3/4_WL	498	39.12	50.00	78.54	55.0	10
■	4	S7/8_DL	473	37.13	50.00	78.54	48.0	10
■	5	S7/8_ML	483	37.95	50.00	78.54	54.0	10
■	6	S7/8_WL	495	38.89	50.00	78.54	46.0	10
■	7	S27/28_DL	522	40.99	50.00	78.54	45.2	10
■	8	S27/28_ML	472	37.03	50.00	78.54	50.6	10
■	9	S27/28_WL	449	35.23	50.00	78.54	35.6	10

TABLE 29: TENSILE RESULTS OF A625 SIMILAR JOINTS

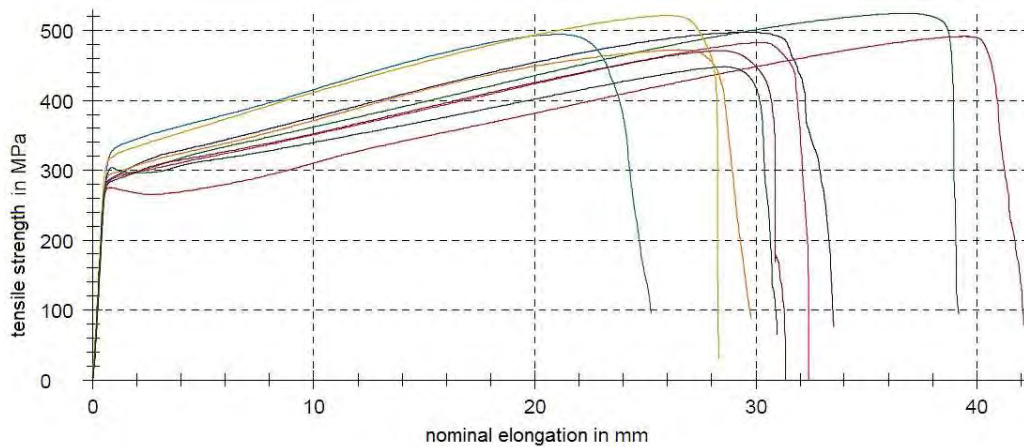


FIGURE 135: TENSILE CURVES OF A625 SIMILAR JOINTS

The next mechanical test was the **Charpy-V test**. Due to the high ductility of the A625 material, just a small percentage of tested pieces broke and delivered valid results. For the tests with the notch next to the fusion zone none of the test specimens broke; moreover, about one third even stopped the swing hammer at the counter bearing (Figure 136). The test pieces with the notch in the FZ mostly did not break (Figure 137) but some values could be collected. Table 30 shows the mean values of the received usable values of this test. All values are higher than the requested impact work (see Table 6 on page 34).



FIGURE 136: STUCK CHARPY TEST SPECIMEN; S7/8



FIGURE 137: CHARPY TEST SPECIMEN; S26/31

	FZ	HAZ
AW	217 J	~300 J

TABLE 30: CHARPY RESULTS, SIMILAR WELDS, AVERAGE VALUE

The last examination, the *side bend test*, was performed with two test specimens without problems. Both were bent to 180° and no cracks occurred in the welding or in the base material.

4.2.2 DISSIMILAR WELDING A625 / CB2

Here, the results of the dissimilar joint welds are presented. Table 28 lists the reached welding depth together with the used parameters within this experiment.

#	ID	<i>I</i> / (mA)	<i>v</i> / (mm/s)	<i>h</i> / (mm)	<i>t</i> / (mm)	<i>E</i> / (kJ/mm)
1	D2/2	165	10.0	0.5	54	19.8
2	D11/12	150	9.0	0.5	53	20.0
3	D5/11	180	15.0	0.5	45	14.4
4	D10/24	170	11.0	1.0	54	18.5
5	D4/11	175	10.0	0.5	57	21.0
6	D3/23	160	9.0	0.5	56	21.3
7	D17/25	185	11.0	0.5	53	20.2
8	D13/18	170	10.0	0.5	53	20.4
9	D15/17	180	10.0	0.5	56	21.6
10	D9/22	210	12.0	0.5	56	21.0
11	D6/37	170	10.0	0.5	54	20.4
12	D9/5B	180	10.0	0.5	55	21.6
13	D5/6B	165	10.5	0.5	48	18.9
14	D7/7B	175	10.0	0.5	53	21.0

TABLE 31: A625 JOINT WELDING PARAMETERS

As in the similar joint welding experiments, the reached depth for the same energy input is higher than in the blind welding study. This confirms the assumption that this is caused by the gap between the welded parts. The welding procedure itself was stable and spiking occurred in a range less than 2mm. A good working parameters compromise for the dissimilar joints could be found. Beam deflection was not observed, all parts were properly demagnetized.

4.2.2.1 MICROSTRUCTURE

In the microstructural investigation of the dissimilar welded parts, the very different reaction of the two materials on etchants made it necessary to use four different etchants. Figure 138 and Figure 139 show a weld etched with a hydrogen peroxide etching agent (see Table 18 on page 46). The A625 is hardly attacked and the fusion zone is barely visible; in contrast the CB2 is totally over-etched (Figure 139). The pictures show that the fusion line is well defined on the CB2 side whereas the border to the A625 appears more diffuse and becomes visible only after a long etching time.



FIGURE 138: DISSIMILAR JOINT , MACRO; D13/18



FIGURE 139: DISSIMILAR JOINT, FZ;D13/18 (1)



FIGURE 140: DISSIMILAR JOINT, FZ; D13/18 (2)



FIGURE 141: DISSIMILAR JOINT, FZ; D13/18 (3)

Under the light microscope the microstructure of the fusion zone looks analogous to the similar joints. Like in the study of similar welds, solidification lines and dendrites are visible. An EDX analysis gives information about the composition in this zone (see Figure 142)

With a line scan, the qualitative composition of the welded materials and the welded zone can be evaluated. Figure 142 shows an overview of the seam, A625 appears light grey, CB2 in dark grey (different density of the materials). The yellow line marks the scanned line. Figure 143 shows the evolution of the amount of the selected elements: Iron (Fe), Nickel (Ni), Chromium (Cr) and Molybdenum (Mo) across the fusion zone.



FIGURE 142: SCAN OVERVIEW; D15/17

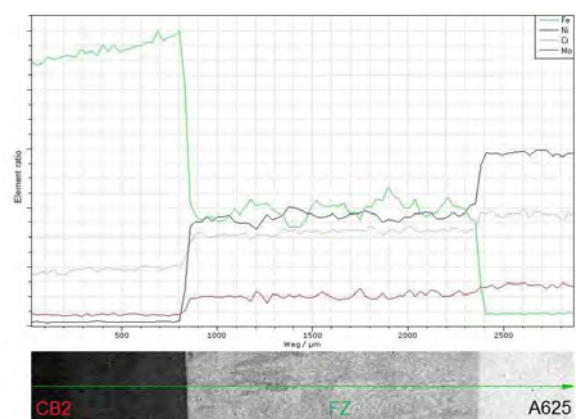


FIGURE 143: LINE SCAN, FZ; D15/17

Starting from the CB2 side, iron (Fe) is strongly reduced in the fusion zone, while the percentage of all other elements (Ni, Cr & Mo) is increased. The composition shifts towards A625. This correlates with the observations from the microstructure analysis, where the fusion zone is almost as acid resistant as the nickel base alloy. Within the fusion zone the element distribution is more or less constant.

Additionally, element mappings were carried out to see the distribution of these elements throughout the weld. Figure 144 illustrates Iron and Figure 145 Nickel. As shown in the line scan, the Ni and the Fe have the majority in the fusion zone. Both elements are just located in its base material and in the fusion zone.

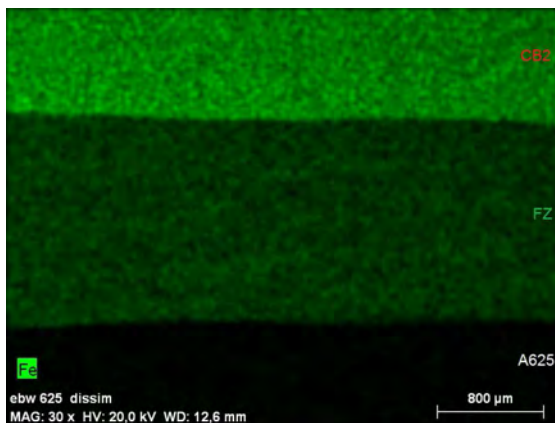


FIGURE 144: FE & NI MAPPING; D15/17

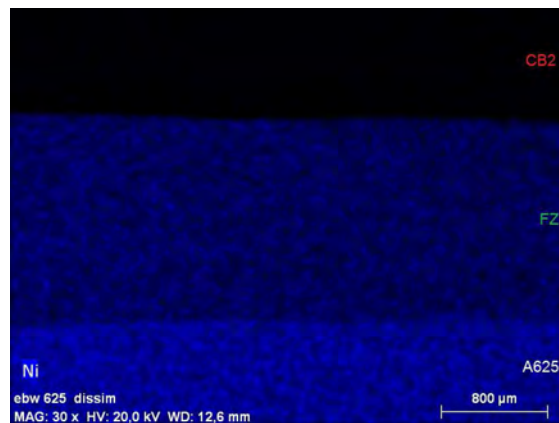


FIGURE 145: NI MAPPING; D15/17

The next mappings (Figure 146 and Figure 147) show elements which are part in the composition of both materials but in higher proportion in the A625; Chromium and Molybdenum. Both pictures offer a clear composition borderline (color saturation) to the CB2; the difference between the fusion zone and the A625 is more difficult to detect.

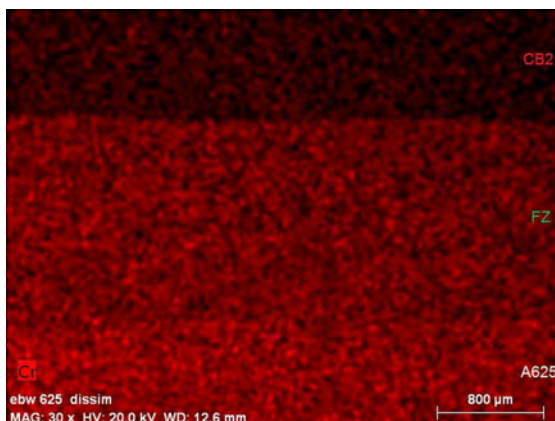


FIGURE 146: CR MAPPING; D15/17

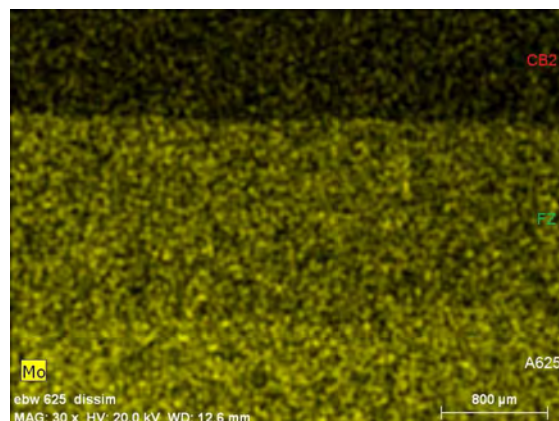


FIGURE 147: MO MAPPING; D15/17

The following figures (Figure 148 till Figure 151) show the heat affected zone on the CB2 side. The etching was done with the Modified Lichtenegger & Bloech II agent (see Table 18 on page 46). The first figure of this row shows that about 1mm besides the fusion line, the structure of the base material remained. Near the FZ a very finely striped new formed Martensite is visible (Figure 149). A coarse grained zone was not detectable in the CB2 heat affected zone.



FIGURE 148: DISSIMILAR JOINT, HAZ; D4/11 (1)



FIGURE 149: DISSIMILAR JOINT, HAZ; D4/11 (2)

With a higher magnification, an approx. 20µm wide area besides the fusion line can be observed where bigger grains, colored in cobalt blue, appear (Figure 150 and Figure 151).



FIGURE 150: DISSIMILAR JOINT, HAZ; D4/11 (3)



FIGURE 151: DISSIMILAR JOINT, HAZ; D4/11 (4)

In this area a rapid solidification from high temperatures takes place; therefore it can be assumed that these bigger grains are δ -ferrite. To confirm this theory a micro hardness inspection (HV0.020) was done.

4.2.2.2 HARDNESS

Several measurements in the matrix (martensite) and the supposed δ -ferrite grains were made. As shown in Figure 152 and in Figure 153, the measurements in the matrix (480HV0.020) show significant higher values compared to the cobalt blue grains (295HV0.020); the latter value is typically in the range of δ -ferrite values [9].

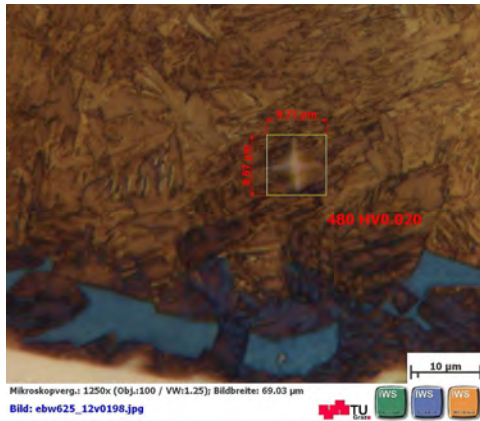


FIGURE 152: MICROHARDNESS CB2 HAZ; D4/11 (1)

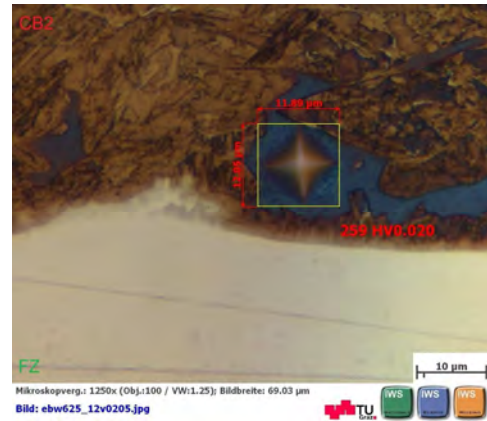


FIGURE 153: MICROHARDNESS CB2 HAZ; D4/11 (2)

Previous studies ([24], [36], [52], [53]) have shown that the EBW process, applied to martensitic chromium steel can cause layers with extremely high values in hardness due the high cooling rate. The measured micro hardness values attend to confirm this point.

In Figure 154, the evolution of hardness across a dissimilar joint is shown. The evolution of hardness in the A625 is equal to what was observed in the similar welding (Chapter 4.2.1). In the fusion zone, the hardness increase is also unproblematic, although, close to the fusion line on the CB2 side a peak value of 430HV10 is reached which drops down to the hardness of the CB2 base material (240HV10) within 1mm. The more tight HV1 line shows the same results (Figure 155).

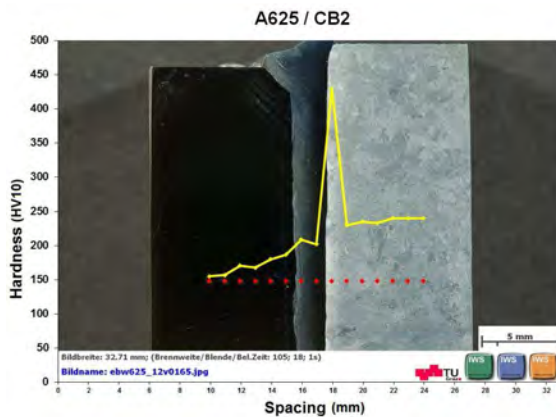


FIGURE 154: : HARDNESS LINE DISSIM, HV10; D4/11

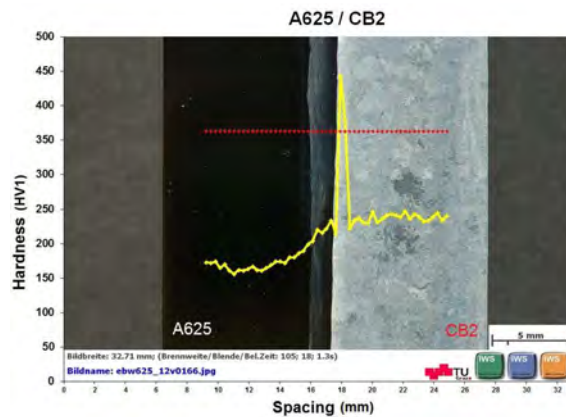


FIGURE 155: : HARDNESS LINE DISSIM, HV1; D4/11

To confirm this high hardness is only present in the CB2, one similar welding with this material was done and investigated (Figure 156 and Figure 157; U=120kV, I=165mA, v=7.25mm/s, fp=-30, t=50mm). Here too a very strong rise and fall of hardness in the HAZ is shown. The peak values are quite equal to the dissimilar joint (440HV10).

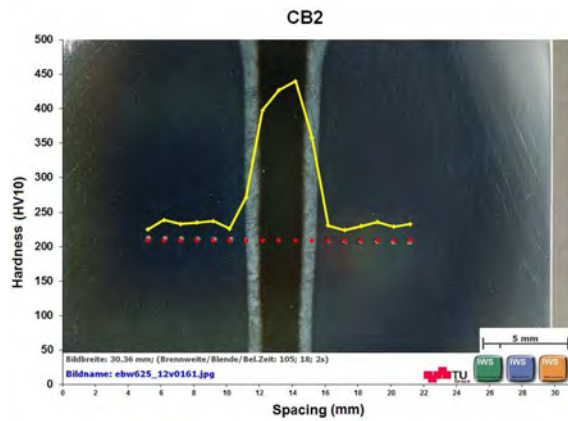


FIGURE 156: HARDNESS LINE CB2, HV10

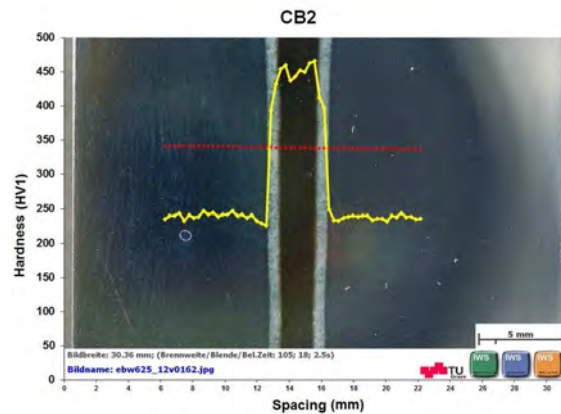


FIGURE 157: HARDNESS LINE CB2, HV1

According to the standard (EN ISO 15614-1 Table 2. [61] and ISO/TR 15608, material group 9.1 [62]), the hardness for the CB2 must not be higher than 350HV10 in as welded condition and 300HV10 in PWHT condition. Hence, the obtained values are not in accordance with the standard: a post weld heat treatment is required.

4.2.2.3 POST WELD HEAT TREATMENT

The PWHT was performed at 700°C in an ambient furnace for 60 minutes. As it could be expected during a PWHT at 700°C [73], LOM investigations did not reveal any changes in the microstructure of the A625. The microstructure in the HAZ of the CB2 now shows tempered martensite (Figure 158 and Figure 159). Close to the fusion line the δ -ferrite grains are recognizable.



FIGURE 158: DISSIMILAR JOINT, TEMPERED; D3/23 (1)



FIGURE 159: DISSIMILAR JOINT, TEMPERED; D3/23 (2)

The micro hardness measurement (Figure 160 and Figure 161) of the matrix and the δ -ferrite grains (with this etching, they appear colored in brown as the matrix) show lower values than in as welded conditions: 367HV0.020 for the matrix and 219HV0.020 for the δ -ferrite grains after PWHT compared to 480HV0.020 for the matrix and 259HV0.020 for the δ -ferrite grains in as welded conditions (see Figure 152 and Figure 153 on page76).

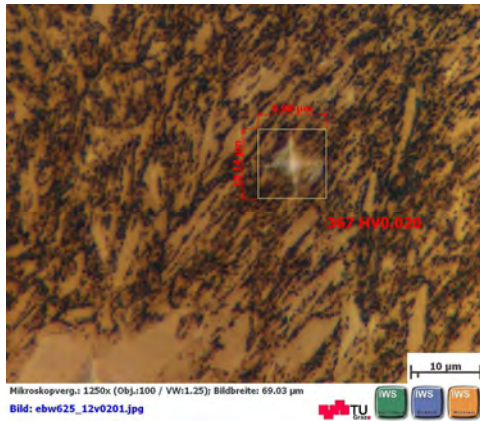


FIGURE 160: MICROHARDNESS DISSIM. JOINT, TEMPERED, D3/23 (1)

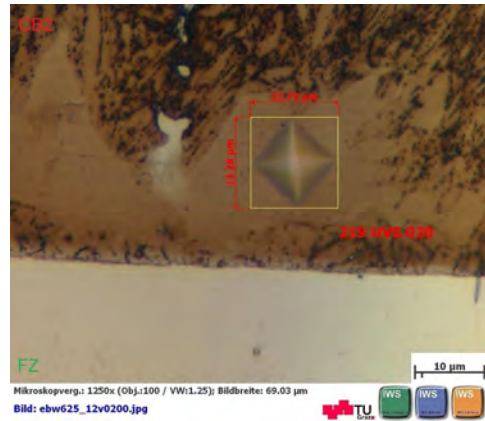


FIGURE 161: MICROHARDNESS DISSIM. JOINT, TEMPERED; D3/23 (2)

To get quantitative values corresponding with the standard, hardness lines with HV10 were carried out on the tempered specimens. Figure 162 and Figure 163 illustrate the results.

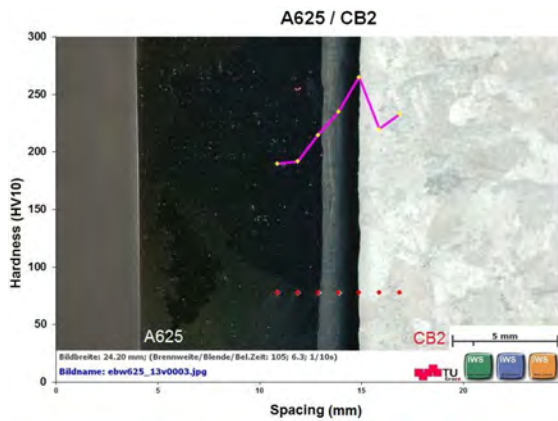


FIGURE 162: HARDNESS DISSIM. JOINT, TEMPERED; D3/23 (1)

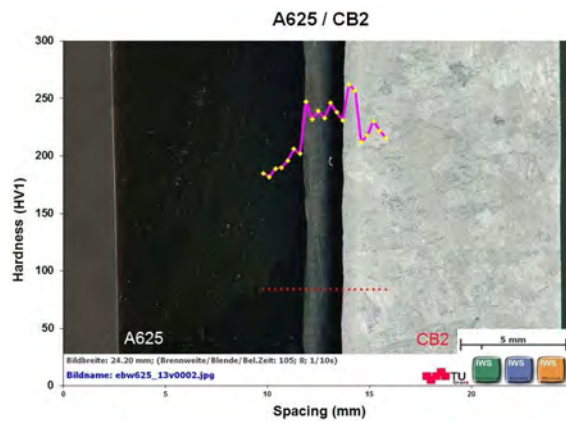


FIGURE 163: HZARDNESS DISSIM. JOINT, TEMPERED; D3/23 (2)

The hardness decreases to 265HV10, which is under the requested maximum in the standard.

4.2.2.4 MECHANICAL TESTING

The **tensile tests** of the dissimilar welds reveal that deformation only occurs on the A625 side. The measured yield strength of the CB2 is about 20% higher than the tensile strength of the A625 (see Table 4 on page 33 and Table 6 on page34). The tensile test samples broke in the A625 base material (Figure 164).



FIGURE 164: TENSILE TEST PIECES DISSIMILAR; D11/12

In Table 32, the measured values for the dissimilar joints are listed and Figure 165 shows the corresponding curves. The PWHT test pieces are marked with red numbers in the table and with red dots in the figure. The tensile strength values for every test are higher than the nominal value for the A625 ($R_{m\text{ nom}}=400\text{MPa}$; $R_{m\text{ act}}=475\text{MPa}$; see Table 6 on page 34). In Table 33 an overview of the average values are given.

Legend	Nr	Labelling	R_m MPa	F_m kN	L_0 mm	S_0 mm ²	A_{manuell} %	d_0 mm
	10	D9/22_DL	482	37.88	50.00	78.54	29.2	10
	11	D9/22_ML	520	40.82	50.00	78.54	33.6	10
	12	D9/22_WL	570	44.78	50.00	78.54	30.8	10
	13	D3/23_DL	455	35.71	50.00	78.54	32.0	10
	14	D3/23_ML	559	43.87	50.00	78.54	26.8	10
	15	D3/23_WL	559	43.87	50.00	78.54	33.2	10
	16	D11/12_DL	467	36.66	50.00	78.54	22.0	10
	17	D11/12_ML	565	44.38	50.00	78.54	22.4	10
	18	D11/12_WL	575	45.18	50.00	78.54	27.6	10
	19	D15/17_DL	576	45.24	50.00	78.54	21.2	10
	20	D15/17_ML	644	50.60	50.00	78.54	20.8	10
	21	D15/17_WL	574	45.09	50.00	78.54	25.0	10

TABLE 32: TENSILE TESTS DISSIMILAR

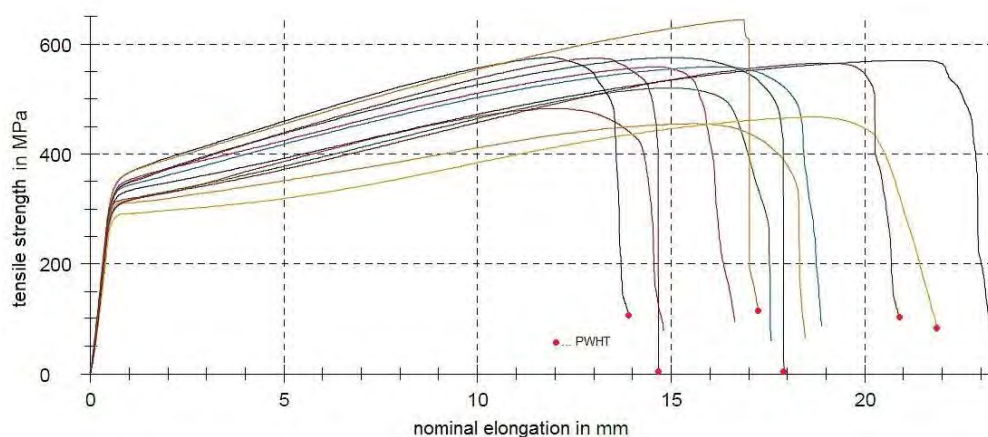


FIGURE 165: TENSILE TESTS DISSIMILAR

	R_m
AW	524 MPa
PWHT	551 Mpa

TABLE 33: OVERVIEW TENSILE VALUES, DISSIMILAR, AVERAGE VALUES

As it can be seen in the graphs and the table, there is one outlier; the tensile strength value of piece number 20 is higher than all others (644MPa). The rupture of this test piece was located near the fusion zone (Figure 166). To identify the exact position of the rupture, the CB2 side of the tensile specimen (left part in Figure 166) was cut lengthwise and a microscopic investigation was made (Figure 167)



FIGURE 166: TENSILE TEST SAMPLE 20; D15/17

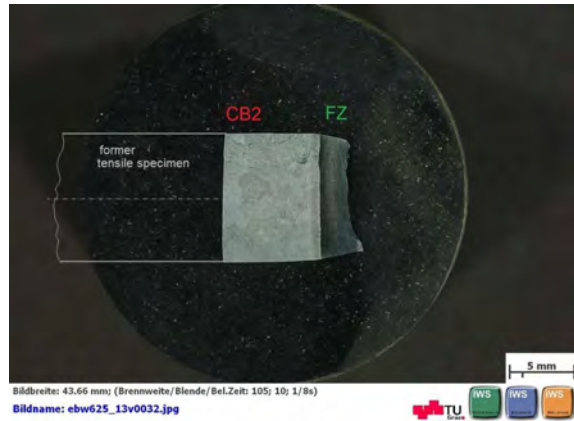


FIGURE 167: EMBEDDED & ETCHED PIECE OF TENSILE SAMPLE; D15/17

Figure 168 shows the whole seam with the rupture very close to the fusion line. At a higher magnification (Figure 169 and Figure 170) the dendritic structure of the fusion zone touches the rupture zone, so the crack occurred in the fusion zone of the welding.



FIGURE 168: TENSILE RUPTURE; D15/17 (1)



FIGURE 169: TENSILE RUPTURE, D15/17 (2)

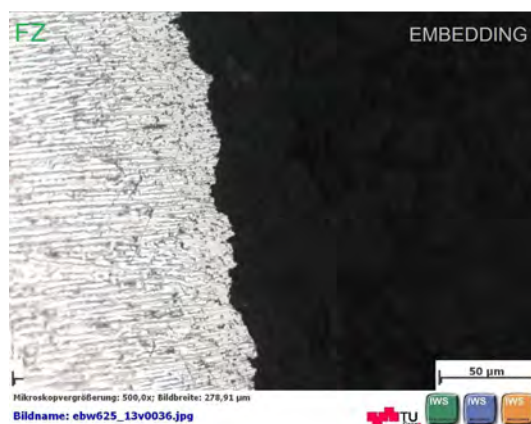


FIGURE 170: TENSILE RUPTURE; D15/17 (3)

Furthermore, the fracture surface of this specimen was compared with a fracture surface obtained with a specimen that broke in the base material. Figure 171 and Figure 172 show pictures of a rupture in the A625 base material.

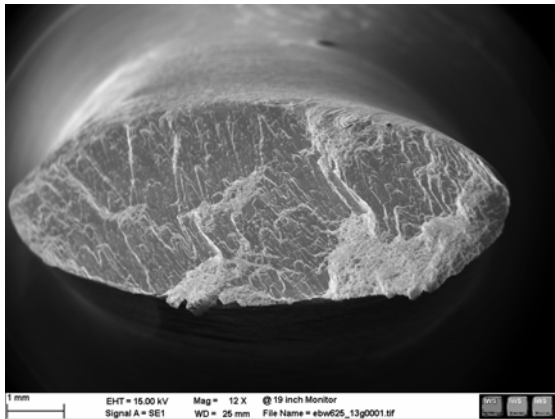


FIGURE 171: FRACTURE SURFACE, A625 BM; D11/12 (1)

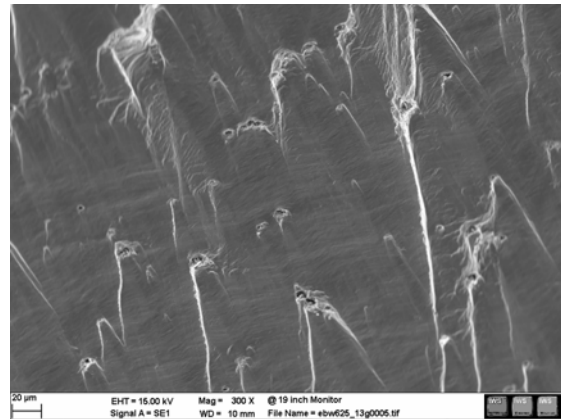


FIGURE 172: FRACTURE SURFACE, A625 BM; D11/12 (2)

In Figure 173 and Figure 174 the fracture surface of test specimen number 20 is displayed. A completely ductile fracture can be recognised with typically formed dimples (Figure 174). The ruptured cross section remained in circular shape.

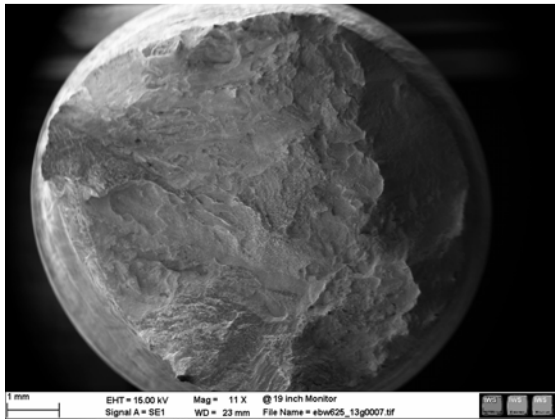


FIGURE 173: FRACTURE SURFACE, A625 FZ; D15/17 (1)

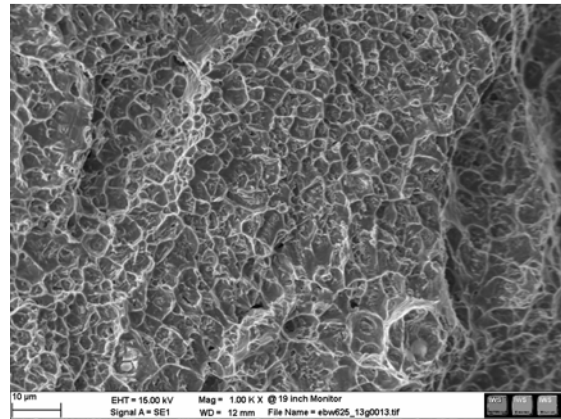


FIGURE 174: FRACTURE SURFACE, A625 FZ; D15/17 (2)

These investigations show that test specimen 20 broke in the fusion zone. However, the tensile strength of this specimen (644MPa) was 161% higher than the nominal tensile strength of the A625 base material (400MPa).

The next step was the **Charpy-V test**. For the dissimilar welds there are three points of interest: First the HAZ of the A625, second, the fusion zone and third, the HAZ of the CB2. The following bar chart shows the impact energies for the different notch positions and conditions.

Charpy Test

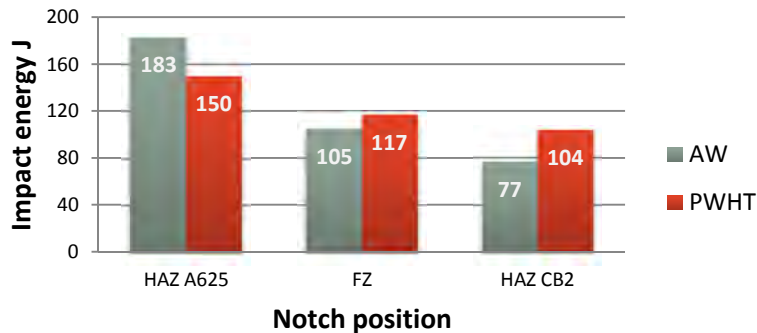


FIGURE 175: IMPACT ENERGY, DISIMILAR JOINTS, AVERAGE VALUES

The lowest energy was consumed in the HAZ of the CB2 and the highest in the HAZ of the A625; the fusion zone exhibits intermediate values. After the PWHT, increased values can be detected in the FZ and in the HAZ of the CB2 whereas in the HAZ A625 reduced values are found. In relation to these results it has to be noted that proper notch location is difficult due to the very small distinct areas. Additionally, for each value for the HAZ of the A625 (AW and PWHT) just three test specimens were tested.

The last performed mechanical test was the *side bend test*. Despite using a conventional side bend test device the experienced staff of the *voestalpine Stahl Linz* could handle the dissimilar test pieces to get reliable results. Both test pieces, one AW and one PWHT, were tested nearly without a shifting during the procedure. No cracks at all occurred in the fusion zone or nearby, but both test pieces show cracks in the CB2 base material (Figure 176 and Figure 177).



FIGURE 176: SIDE BEND SPECIMEN, AW, CB2 BM; D9/5



FIGURE 177: SIDE BEND SPECIMEN, PWHT, CB2 BM; D9/5

4.2.3 STANDARD WELDING PROCEDURE SPECIFICATION (WPS)

After welding the specimen for the WPS, the joined specimen specified according the EN ISO15614-11 [63] standard at the *VAGT*. First, a full inspection of the weld with non-destructive tests was taken: ultrasonic, x-ray and penetration testing. None of these testing procedures showed a welding failure. Next the machining of the test pieces and the heat treatment (700°C, 60min) were carried out. The following mechanical testing, (except the side bend test) was also performed in Traisen. The microscopy and the hardness test were done at the *TU Graz*.

This *final welding* was done with the best parameter combination found in the previous performed welding trials.

Beam current I / (mA)	Welding speed v / (mm/s)	Focal point fp / (mA)	Figure amplitude h / (mm)	Welding time in seconds
180	10	-30	0.5	35

TABLE 34: PARAMETERS EN STANDART TEST

4.2.3.1 MICROSCOPY

The macroscopic picture (Figure 178) of the pWPS welding shows a well-shaped, complete joint with no visual defects. In the CB2 base material some pores can be detected (green arrow).



FIGURE 178: MACRO PWPS SPECIMEN

Also the microscopic pictures show no imperfections in the fusion zone. The solidification lines are steady and do not form a crest in the seam centre (Figure 179). The dendritic structure in the fusion zone (Figure 180) looks as in the former welded joints.



FIGURE 179: MICROSTRUCTURE WPS SPECIMEN



FIGURE 180: MICROSTRUCTURE WPS SPECIMEN, FZ

Because the crucial zone of this joint is in the HAZ on the CB2 side, a further etching was done. The following two microscopic pictures of the CB2 HAZ (Figure 181 and Figure 182) show the same results as presented in Figure 158 and Figure 159 on page 77: The microstructure shows tempered martensite and close to the fusion line the δ -ferrite grains are recognizable.



FIGURE 181: HAZ CB2, WPS SPECIMEN (1)



FIGURE 182: HAZ CB2, WPS SPECIMEN (2)

4.2.3.2 HARDNESS

The hardness (Figure 183 and Figure 184) measurement shows no conspicuities or disparities. Figure 183 shows the standard line with a top value of (268HV10) in the HAZ of the CB2. In Figure 184 the HV1 row is shown (top value 287HV1). All values are below the maximum allowed value (300HV10) according to the standard.

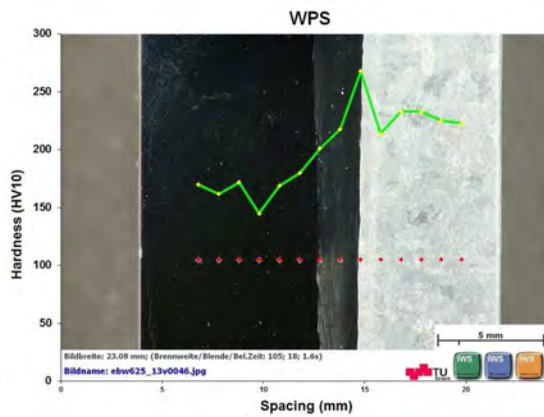


FIGURE 183: HARDNESS LINE WPS, HV10

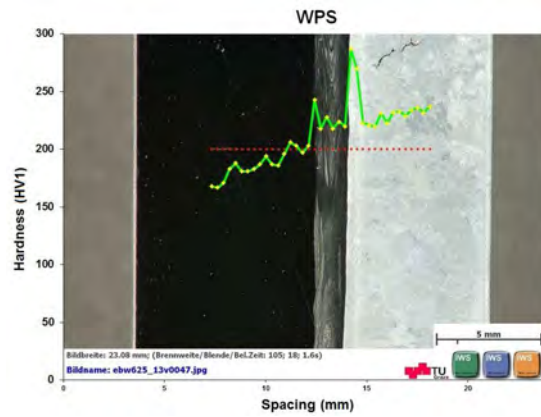


FIGURE 184: HARDNESS LINE WPS, HV1

The results of the hardness measurement of the WPS joint correspond with the former measuring taken on the PWHT dissimilar joints (Figure 154 and Figure 155 on page 76).

MECHANICAL TESTING

The **tensile tests** of the WPS standard delivered equivalent results as the test pieces in the dissimilar joint welding study. All tensile test pieces pass this test, according to the pWPS standard. Values and graphs are shown below (Table 35 and Figure 185).

	R_m
PWHT	513 MPa

TABLE 35: TENSILE VALUES, PWPS, AVERAGE VALUE

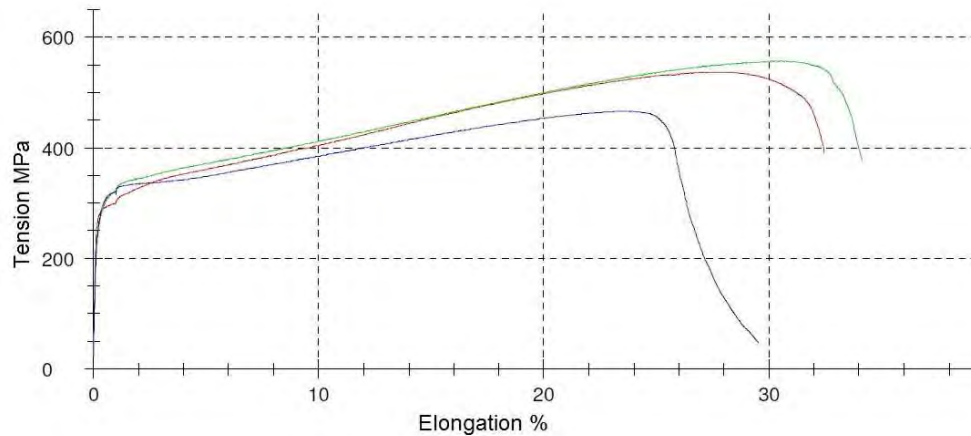


FIGURE 185: TENSILE DIAGRAM, PWPS

For the following Charpy test, the test pieces were only notched in the fusion zone. The values measured from the VAGT differ strongly to the values measured at the TU Graz (FZ, PWHT:117J).

	FZ
PWHT	78 J

TABLE 36: CHARPY VALUE, PWPS, AVERAGE VALUE

The impact energy for the fusion zone (PWHT) is around one third less but is still high enough to pass the pWPS requirements. Due to the simple and stable testing procedure this deviation can be attributed to difficulties of positioning the notch in the very small HAZ. Furthermore, the geometry of the notch and the notch ground can influence the result; at the TU Graz the notch was milled with a notch miller; the notches for the WPS test specimens were made with a broach.

The last mechanical test was the *side bend test*. From the EN ISO joint specimen five test pieces were taken, two were tested in as welded state and the other three were post weld heat treated before testing. A slight shifting to the A625 happened in all tests (Figure 186) but the seam stays in a proper test position every time. Table 37 lists up the results for the bending test evaluated from the *voest alpine* inspection personnel.



FIGURE 186: SIDE BEND SPECIMEN; SB4

ID	Condition	Angle	Result
SB1	PWHT	180°	o.B. (*)
SB2	PWHT	180°	o.B. (+)
SB3	PWHT	180°	(#)
SB4	AW	180°	o.B.
SB5	AW	180°	o.B. (*)

Caption

o.B. ... without objections
 (*) ... crack < 3mm in weld metal
 (#) ... crack > 3mm in weld metal
 (+) ... crack > 3mm in base metal CB2

TABLE 37: RESULTS BENDING TEST

Figure 187 and Figure 188 show test piece SB1 with three small defects in the left and right fusion line. Some cracks in the CB 2 base material occurred.



FIGURE 187: SB1(*) (1)



FIGURE 188: SB1(*) (2)

Figure 189 and Figure 190 show the only test piece that failed, SB3. The crack starts on the A625 fusion line and runs diagonal along the seam.



FIGURE 189: SB3(#) (1)

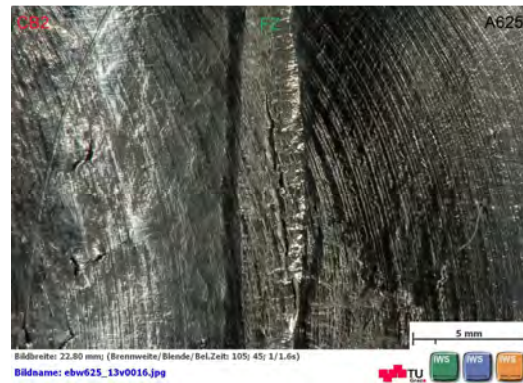


FIGURE 190: SB3(#) (2)

In test piece SB5 one small defect in the A625 fusion line could be detected.



FIGURE 191: SB5(*) (1)



FIGURE 192:SB5(*) (2)



FIGURE 193: SB2(+)

As expected, the side bending test is the most crucial one. One test piece failed the others show some small defects near the fusion line. In all test specimens cracks were located in the CB2 base material.

It should be considered that the wire eroded test pieces do not show defects in or besides the fusion line in contrast to the milled ones. Due to the different hardness near the seam, the milling tool tends to swing and it is not possible to produce the same accurate surface in this area as the eroded one. These circumstances may be the reason for the small defects in the milled parts.

However, the most important insight from this test is that the high hardness layer in the CB2 side did not cause a fracture during the bending test or the tensile test.

RÉSUMÉ JOINT WELDING

The joint welding process with the electron beam has its crucial point in the preparing of the joint. A well machined surface and a good positioning of the gap is most important for the result. The process is done very stable with properly chosen parameters. For both, dissimilar and similar welding the microstructure and the geometry of the weld was good and no problems occurred during the mechanical tests.

5 SUMMARY & CONCLUSION

This chapter sums up the experimental workload and gives an overview about the collected results.

5.1 SUMMARY

The scope of this thesis was to ascertain the weldability of cast nickel base Alloy 625 with cast martensitic 9% chromium steel COST CB2 using electron beam welding. This thesis was continuative to the thesis of Bernhard Berger „*Dissimilar Schweißen von Guss-Stücken (Konstruktionsschweißungen) NIBAS 625 mit warmfestem Cr- Stahl COST CB2*“ where the weldability of the same materials, using manual arc welding, was investigated.

The experimental tasks started with evaluating the EBW process parameters and their effect on the weld. Thereafter blind welds in both materials were performed and metallographically investigated. Next, similar (A625) and dissimilar (A625 to CB2) joint welding experiments, were carried out. Then the microstructures of these joints were analysed and mechanical tests were performed. Analysing and testing of the specimens were done in as welded as well as in post weld heat treated condition. Finally, a welding experiment according to the standard preliminary welding procedure specification (pWPS) was carried out. The mechanical characterisation of this specimen was made at the *voestalpine Gießerei Traisen (VAGT)*.

The results of this work showed that the energy per length unit, controlled with the beam current I and the welding speed v , are the most significant parameters for the welding depth. The focal point fp is very important to get a well-shaped seam without defects. The oscillation amplitude h was highly influencing the stability of the keyhole. It has to be considered that for joint welding the beam energy has to be slightly reduced compared to blind welding because of the gap between the parts.

The metallographic investigations showed that the microstructure of the small fusion zone has a fine grained dendritic structure and the chemical composition of this zone is a homogenous mixture of the base materials. A heat affected zone in the A625 is barely noticeable. In the HAZ on the CB2 steel side a 0.5mm wide layer with new formed martensite and very high hardness values (430HV10) was found; no coarse grain zone could be observed. Directly next to the fusion zone, a 20 μ m wide area was discovered where soft δ -ferrite grains appeared.

The performed mechanical tests (tensile, Charpy and side bend test) for the similar joints revealed no imperfections of this welds. The dissimilar joints could successfully pass these tests; both, the post weld heat treated specimens as well as the as welded specimens. The small layer, with high hardness present in the dissimilar as welded joint, seemed to have no significant negative impact on the mechanical properties of the joint. It has to be noted that during all dissimilar side bend tests cracks in the CB2 base material appeared.

However, two outliers could be found during the mechanical testing: one tensile specimen (dissimilar, PWHT) with a very high tensile strength value (644MPa) broke within the seam and another of the side bend test pieces (dissimilar PWHT) also failed within the seam.

5.2 CONCLUSION

For similar and dissimilar welding appropriate parameters could be found. The work pieces were completely welded and the joints exhibit good mechanical properties.

The main effort in EBW is to determine the correct welding parameter for the respective task, but then EBW is a reliable and well reproducible process.

The greatest advantage of the EBW process, in this studied area of applications, is an economical one. It is possible to weld thick parts in a very short time without using filler material. If the whole manufacturing process is fitted to this technique the huge potential of the electron beam can be used not only to do welding jobs very efficiently, but also to perform further electron beam operations (heat treating, surface treatment, engraving, ...). The main problem of EBW is the need of vacuum, so a limitation in part dimensions and cycle time has to be considered.

6 OUTLOOK

This thesis and the related experiments were the first work at the TUG using EBW. Due to the fact that the IWS had no existing experience with EBW and the time to familiarize with the new machine was very limited, this present work does not claim to provide the optimum method to join these materials. It was rather a first step to work with EBW and to evaluate how much effort is required to find out the right parameters to produce a proper weld.

In order to find optimized welding parameters, further welding experiments would be necessary; some parameters which were left constant in this thesis could be varied. Moreover, the evolution of the mechanical values with a variation of the welding parameter could be investigated.

For a later usage of EBW in this case, further investigation of the creep behavior of the welded joint has to be carried out. Particularly, the fine grained fusion zone and the presence of δ -ferrite in the HAZ of CB2 could be unfavorable for the creep behavior. Furthermore, the evolution of the microstructure during exposure to high temperature must be investigated. The effect of the high hardness layer in the CB2 HAZ on the fatigue strength should be investigated as well.

Another unanswered question is the appearance of hot cracks in the CB2 steel during the blind welding study (heat input during welding, shrinkage during welding, thermal stress).

Finally, it can be said that there is a lot of space for further EBW investigation in the area of basic research as well as for special applications.

7 LIST OF FIGURES

Figure 1: Efficiency over temperature [3]	1
Figure 2: Material arrangement for a 700°C turbine [12]	2
Figure 3: Comparison EBW to MAW with rod-electrode (50mm)	3
Figure 4: CB2 microstructure [14]	4
Figure 5: Reference numbers of welding processes, ISO 40 63	6
Figure 6: Coulomb force [28].....	8
Figure 7: Lorentz force [28]	8
Figure 8: EB reflection	9
Figure 9: Grade of efficiency beam welding [28]	9
Figure 10: EBW machine modules [31]	9
Figure 11: EB generator [28]	10
Figure 12: Emission current density over cathod temperatur [29].....	11
Figure 13: Triode system [29].....	11
Figure 14: Centering coil [28]	12
Figure 15: Stigmator [28].....	12
Figure 16: Electromagnetic lens [28].....	13
Figure 17: Beam density [28]	13
Figure 18: Operating distance & focal position [29]	14
Figure 19: Different focal positions [29].....	14
Figure 20: Influence of focal position [19]	15
Figure 21: Oscillation figures, top view [40].....	16
Figure 22: Oscillation figures, section view [36].....	16
Figure 23: Welding speed over seam thickness [29].....	17
Figure 24: Power density [19]	17
Figure 25: Deep welding effect [13]	18
Figure 26: Moving keyhole, top view [26].....	18
Figure 27: Moving keyhole, 3D [27]	18
Figure 28: Forces in the keyhole [13]	19
Figure 29: Isothermal lines EBW [13]	19
Figure 30: Temperature gradient [13].....	19
Figure 31: Specific heat input of welding techniques [42].....	19
Figure 32: Steel, EB weld depth 35mm	20
Figure 33: basic EBW joint assemblies [44].....	20
Figure 34: Hidden joint [44]	20
Figure 35: Surface preparing [28], [44]	21
Figure 36: Multi capillary welding [45].....	21
Figure 37: Cross section multi pool welding [47]	22
Figure 38: Top view multi pool welding [47].....	22
Figure 39: Pores in cast iron [47].....	22
Figure 40: Multi process welding [46]	22
Figure 41: Stress reducing by heating spots [48]	23
Figure 42: Comparison EBW and SMAW [23]	24
Figure 43: Spiking [29]	24

Figure 44: Thermoelectric effect [24].....	26
Figure 45: Beam deflection in dissimilar welding [27]	26
Figure 46: 2-factor-to-level design [54].....	27
Figure 47: Fully factorial design table [54]	27
Figure 48: Central composite design [54]	28
Figure 49: Box-Behnken design [54], [55]	28
Figure 50: Effects of A and B [54]	29
Figure 51: Interaction of A and B [54]	29
Figure 52: Main effects plot [55]	29
Figure 53: contour plot and Responce surface model [55].....	30
Figure 54: Experimental Workflow.....	32
Figure 55: CB2 blanks	33
Figure 56: A625 blanks	33
Figure 57: CB2 micro structure.....	34
Figure 58: A625 micro structure.....	35
Figure 59: A625 precipitattes	35
Figure 60: EBW-M @ TU Graz	35
Figure 61: Build -up chamber machine	35
Figure 62: Pre-test specimens	36
Figure 63: Temperature measurement set up	38
Figure 64: Welding setup standard	40
Figure 65: EN standart part	42
Figure 66: Flow of test material	43
Figure 67: Samples for mechanical testing	43
Figure 68: Specimen layout	44
Figure 69: Specimen layout side bend	44
Figure 70: Wire eroded joint sample.....	44
Figure 71: Welded EN standard part.....	44
Figure 72: Specimen layout EN Standart part	44
Figure 73: Tensile test piece [68]	48
Figure 74: Charpy test pieces, a) notch in the FZ, B) notch in the HAZ.....	48
Figure 75: Etched Charpy test pieces	49
Figure 76: Side bend test piece	50
Figure 77: Supported side bend test	50
Figure 78: Pilot study, mild steel	52
Figure 79:Factor plot pilot study	52
Figure 80: contour plot pilot study.....	52
Figure 81: Inscribed master study box	53
Figure 82: Temperature curve, 30 minutes.....	53
Figure 83: Temperature curve, 1 minute	53
Figure 84: Cross section of CB2 blind welding, block 1	55
Figure 85: Cross section of CB2 blind welding, block 2	55
Figure 86: Main effect plot blind welding CB2, block 1 & 2	56
Figure 87: Contour plot CB2 (v/i, m)	56
Figure 88: Contour plot CB2 (v/i, m)	56
Figure 89: Contour plot CB2 (h/fp).....	57

Figure 90: Contour plot CB2 (h/fp).....	57
Figure 91: Crack investigation, specimen positions	57
Figure 92: #11; cavity, macro view.....	58
Figure 93: #11; cavity, Micro view.....	58
Figure 94: #27; crack surface overview	58
Figure 95: #27; top area, SM	59
Figure 96: #27; top area, SEM_1	59
Figure 97: #27; top area, SEM_2	59
Figure 98: #27, top area, SEM_3	59
Figure 99: #27; bottom area, SM	59
Figure 100: #27; bottom area, SEM_1	59
Figure 101: #27; bottom area, SEM_2	60
Figure 102: #27; bottom area, SEM_3.....	60
Figure 103: #27; brittle fracture, SEM_1.....	60
Figure 104: #27; brittle fracture, SEM_2.....	60
Figure 105: Blind welding CB2, block 3	61
Figure 106: Blind Welding CB2, block 4, Etched.....	61
Figure 107: Blind welding CB2, block 3, top View 1	61
Figure 108: Schäffler diagramm CB2 [72].....	62
Figure 109: Blind welding A625; block 1	63
Figure 110: Blind welding A625; block 2	63
Figure 111: Blind welding A625, block 1, top view 1.....	63
Figure 112: Blind welding A625, block 2, top view 2.....	63
Figure 113: Main effect plot blind weldings A625, block 1 & 2	64
Figure 114: Contour plot (v/l) A625, block 1 & 2	64
Figure 115: Contour plot (h/l) A625, block 1 & 2	64
Figure 116: parameter box for A625, block 3.....	64
Figure 117: Contour plot (V/l) A625, block 3	65
Figure 118: A625 block 3, material fusion (1)	66
Figure 119: A625 Block 3, material fusion (2)	66
Figure 120: A625, macro; S14/15.....	67
Figure 121: A625 BM / FZ; S14/15 (1)	67
Figure 122: A625 BM / FZ; S14/15 (2)	68
Figure 123: A625 BM / FZ; S14/15 (3)	68
Figure 124: cross section, top; S27/28	68
Figure 125: Cross section, centre; S27/28.....	68
Figure 126: Horizontal section; S3/4	69
Figure 127: Horizontal section with discontinuity [29]	69
Figure 128: Centre line fusion zone; S3/4 (1).....	69
Figure 129: Centre line fusion zone; S3/4 (2).....	69
Figure 130: Hardness line HV10, top; S14/15	69
Figure 131: Hardness line HV10, centre; S26/31	69
Figure 132: Hardness line HV1, root; S14/15	70
Figure 133: Hardness line HV1, centre; S26/31	70
Figure 134: Tensile test pieces, A625 similar; S3/4.....	70
Figure 135: Tensile curves of A625 similar joints.....	71

Figure 136: Stuck charpy test specimen; S7/8	71
Figure 137: Charpy test specimen; S26/31	71
Figure 138: Dissimilar joint , macro; D13/18.....	73
Figure 139: Dissimilar joint, FZ;D13/18 (1).....	73
Figure 140: Dissimilar joint, FZ; D13/18 (2).....	73
Figure 141: Dissimilar joint, FZ; D13/18 (3).....	73
Figure 142: Scan overview; D15/17.....	73
Figure 143: Line scan, FZ; D15/17	73
Figure 144: Fe & Ni mapping; D15/17	74
Figure 145: Ni mapping; D15/17	74
Figure 146: Cr mapping; D15/17	74
Figure 147: Mo mapping; D15/17	74
Figure 148: Dissimilar joint, HAZ; D4/11 (1).....	75
Figure 149: Dissimilar joint, HAZ; D4/11 (2).....	75
Figure 150: Dissimilar joint, HAZ; D4/11 (3).....	75
Figure 151: Dissimilar joint, HAZ; D4/11 (4).....	75
Figure 152: Microhardness CB2 HAZ; D4/11 (1).....	76
Figure 153: Microhardness CB2 HAZ; D4/11 (2).....	76
Figure 154: : Hardness line dissim, HV10; D4/11	76
Figure 155: : Hardness line dissim, HV1; D4/11	76
Figure 156: Hardness line CB2, HV10	77
Figure 157: Hardness line CB2, HV1	77
Figure 158: Dissimilar joint, tempered; D3/23 (1)	77
Figure 159: Dissimilar joint, tempered; D3/23 (2)	77
Figure 160: Microhardness dissim. joint, tempered, D3/23 (1).....	78
Figure 161: Microhardness dissim. joint, tempered; D3/23 (2).....	78
Figure 162: Hardness dissim. joint, tempered; D3/23 (1).....	78
Figure 163: HZardness dissim. joint, tempered; D3/23 (2).....	78
Figure 164: Tensile test pieces dissimilar; D11/12.....	78
Figure 165: Tensile tests dissimilar	79
Figure 166: Tensile test sample 20; D15/17.....	80
Figure 167: Embedded & etched piece of Tensile sample; D15/17	80
Figure 168: Tensile rupture; D15/17 (1).....	80
Figure 169: Tensile rupture, D15/17 (2).....	80
Figure 170: Tensile rupture; D15/17 (3).....	80
Figure 171: fracture surface, A625 BM; D11/12 (1).....	81
Figure 172: fracture surface, A625 BM; D11/12 (2).....	81
Figure 173: fracture surface, A625 FZ; D15/17 (1).....	81
Figure 174: fracture surface, A625 FZ; D15/17 (2).....	81
Figure 175: Impact energy, disimilar joints, average values	82
Figure 176: Side bend specimen, AW, CB2 BM; D9/5	82
Figure 177 Side bend specimen, PWHT, CB2 BM; D9/5.....	82
Figure 178: Macro pWPS specimen.....	83
Figure 179: Microstructure WPS specimen.....	83
Figure 180: Microstructure WPS specimen, FZ	83
Figure 181: HAZ CB2, WPS specimen (1).....	84

Figure 182: HAZ CB2, WPS specimen (2)	84
Figure 183: Hardenss line WPS, HV10	84
Figure 184: Hardenss line WPS, HV1	84
Figure 185: Tensile diagram, pWPS.....	85
Figure 186: Side bend specimen; SB4	85
Figure 187: SB1(*) (1)	86
Figure 188: SB1(*) (2)	86
Figure 189: SB3(#) (1)	86
Figure 190: SB3(#) (2)	86
Figure 191: SB5(*) (1)	87
Figure 192:SB5(*) (2).....	87
Figure 193: SB2(+)	87

8 LIST OF TABLES

Table 1: Classification of EBW techniques	23
Table 2: Testing schedule	31
Table 3: Nominal and actual chemical composition of CB2 steel [56].....	33
Table 4: Mechanical properties of CB2 material[56]	33
Table 5: Nominal and actual chemical composition of A625 (weight percent) [57].....	34
Table 6: Mechanical properties of A625 in solution annealed condition [58].....	34
Table 7: benchmarking data EB-machine.....	35
Table 8: Factor combinations pilot study.....	37
Table 9: Parameters blind welding CB2, block 1 & 2.....	38
Table 10: Parameters blind welding CB2, block 3 & 4.....	39
Table 11: Parameters A625, block 1 & 2	39
Table 12: Parameters A625, block 3.....	39
Table 13: Parameters for A625 similar joints.....	41
Table 14: Parameters dissimilar joints	41
Table 15: Parameter set for welding specimen to be tested according EN ISO 15614-1	42
Table 16: Mechanical test matrixsamples.....	43
Table 17: Macro etchant	45
Table 18: Overview etchants.....	46
Table 19: Tensile test pieces	48
Table 20: Charpy test pieces	49
Table 21: Side bend test pieces.....	50
Table 22: Parameters pilot study	51
Table 23: Parameters blind welding CB2, block 1 & 2.....	54
Table 24: Parameters blind Welding CB2, block 3 & 4.....	60
Table 25: Parameter blind welding A625, block 1 & 2	62
Table 26: Parameters A625, block 3.....	65
Table 27: Arithmetic mean penetration depth similar welding A625, block 3	65
Table 28: Similar joint welding parameters	67
Table 29: Tensile results of A625 similar joints.....	71
Table 30: Charpy results, similar welds, average value.....	71
Table 31: A625 joint welding parameters	72
Table 32: Tensile tests dissimilar.....	79
Table 33: Overview tensile values, dissimilar, average values.....	79
Table 34: Parameters EN standart test	83
Table 35: Tensile values, pWPS, average value.....	84
Table 36: Charpy value, pWPS, average value	85
Table 37: Results bending test	86

9 LIST OF EQUATIONS

Equation 1: Recrystallisation temperature [6]	2
Equation 2: Kinetic energy	8
Equation 3: Schonland equation	8
Equation 4: Electric charge [32]	11
Equation 5: Electric current [32]	12
Equation 6: Electric power [32]	12
Equation 7: Effect A and B [54]	27
Equation 8: Interaction effect AB [54].....	27
Equation 9: Energy input per length	51

10 REFERENCES

- [1] OECD and IEA, "International Energy Agency - Prospect of limiting the global increase in temperature to 2°C is getting bleaker," 2012. [Online]. Available: http://www.iea.org/index_info.asp?id=1959. [Accessed: 14-Jun-2012].
- [2] P. Ploumen, G. Stienstra, and H. Kamphuis, "Reduction of CO₂ emissions of coal fired power plants by optimizing steam water cycle," *Energy Procedia*, vol. 4, pp. 2074–2081, Jan. 2011.
- [3] H. Tschaffon, J. Ewers, and C. Stolzenberger, "COMTES700 – auf dem Weg zum 700 ° C Kraftwerk
Notwendigkeit der Kraftwerkserneuerung in Europa," 2005.
- [4] EON AG, "Wir arbeiten mit Hochdruck am Kraftwerk der Zukunft," *Technologische Herausforderungen*, 2012. [Online]. Available: <http://www.eon.com/de/geschaeftsfelder/stromerzeugung/kohle/hocheffiziente-kohleerzeugung/technologische-herausforderungen.html>. [Accessed: 14-Jun-2012].
- [5] W. Weißbach, *Werkstoffkunde und Werkstoffprüfung*, 12th ed. Wießbaden: Vieweg, 1988.
- [6] R. Ehlers, "Oxidation von ferritischen 9-12% Cr-Stählen in wasserdampfhaltigen Atmosphären bei 550 bis 650°C," Rheinisch-Westfälischen Technischen Hochschule Aachen, 2000.
- [7] V. Kocks and S. Zimmermann, "Stahlrohre für Kraftwerksanwendungen - Werkstoffanforderungen und Auslegungspraxis," 22. *Oldenburger*, pp. 196–201, 2008.
- [8] A. Göcmen, "Grundrisse der Gefügeausbildung und der Zeitstandeigenschaften martensitischer 9-12% Chromstähle," ETH Zürich, 1997.
- [9] B. Berger, "Dissimilar Schweißen von Guss-Stücken (Konstruktionsschweißungen) NIBAS 625 mit warmfestem Cr- Stahl COST CB2," Technische Universität Graz, 2011.
- [10] Special Metals Co., "INCONEL alloy 625." Huntington, US, 2006.
- [11] K. Wieghardt, "Siemens Steam Turbine Design for AD700 Power Plants (AD700 financed activities)," Milan, 2005.
- [12] Saarschmiede, "Saarschmiede - forging vision," 700°C - *Kraftwerke*. [Online]. Available: <http://www.saarschmiede.com/64.html>. [Accessed: 15-Jun-2012].
- [13] N. Swoboda, "Schweißgerät der Superlative," *Kleine Zeitung Steiermark*, Graz, pp. 26–27, 2013.
- [14] I. Holzer, "Modelling and Simulation of Strengthening in Complex Martensitic 9-12% Cr and a Binary Fe-Cu Alloy," Graz University of Technology, 2010.
- [15] B. Sonderegger, "Charakterisierung der Substruktur in modernen Kraftwerkswerkstoffen mittels der EBSD- Methode," Graz University of Technology, 2005.
- [16] P. Mayr, "Evolution of microstructure and mechanical properties of the heat affected zone in B-containing 9% chromium steels," Graz University of Technology, 2007.
- [17] S. K. Rai, A. Kumar, V. Shankar, T. Jayakumar, K. Bhanu Sankara Rao, and B. Raj, "Characterization of microstructures in Inconel 625 using X-ray diffraction peak broadening and lattice parameter measurements," *Scripta Materialia*, vol. 51, no. 1, pp. 59–63, Jul. 2004.

- [18] ThyssenKrupp, "Microfer 6020 hMo - alloy 625," no. 4118. Werdohl, Germany, 2007.
- [19] B. Berger, "Literatur study on electron beam welding of martensitic Cr-steel and nickle base alloy," Graz, 2011.
- [20] V. Shankar, K. Bhanu Sankara Rao, and S. . Mannan, "Microstructure and mechanical properties of Inconel 625 superalloy," *Journal of Nuclear Materials*, vol. 288, no. 2–3, pp. 222–232, Feb. 2001.
- [21] D. Dobeneck v., *Elektronenstrahlschweißen - Anwendungsbeispiele aus 30 Jahren Lohnschweißpraxis*, 2. Auflage. Burg, Germany: pro-beam AG & Co. KGaA, 2007.
- [22] D. Dobeneck v., K. H. Steigerwald, S. G., B. R., D. Powers, O. K. Nazarenko, W. A. Dietrich, H. Irie, and D. Wyatt, *An International History of Electron Beam Welding*. Burg, Germany: pro-beam AG & Co. KGaA, 2007.
- [23] Steigerwald Strahltechnik SST, "Geschichte der EB-Technik," 2012. [Online]. Available: http://www.steigerwald-eb.de/de/infocenter_eb_geschichte.php. [Accessed: 25-Jun-2012].
- [24] M. Dobner, "Untersuchungen zum Elektronenstrahlschweißen dickwandiger Bauteile," Technische Hochschule Aachen, 1996.
- [25] Y. Hu, X. He, G. Yu, Z. Ge, C. Zheng, and W. Ning, "Heat and mass transfer in laser dissimilar welding of stainless steel and nickel," *Applied Surface Science*, vol. 258, no. 15, Mar. 2012.
- [26] Y. Luo, J. Liu, C. Du, H. Xu, and C. Li, "The evaporation effect of front keyhole wall in penetration welding with an electron beam," *Materials Science Forum*, vol. 686, pp. 355–360, 2011.
- [27] M. Ziolkowski and H. Brauer, "Modelling of Seebeck effect in electron beam deep welding of dissimilar metals," *COMPEL: The International Journal for Computation and Mathematics in Electrical and Electronic Engineering*, vol. 28, no. 1, pp. 140–153, 2009.
- [28] V. Adam, U. Clauß, D. Dobeneck v., T. Krüssel, and T. Löwer, *Electron beam welding - The fundamentals of a fascinating technology*, 1st ed. Burg, Germany: pro-beam AG & Co. KGaA, 2011.
- [29] H. Schultz, *Elektronenstrahlschweißen*, 2nd ed. Düsseldorf: DVS-Verlag GmbH, 2000.
- [30] G. Spur and T. Stöferle, *Handbuch der Fertigungstechnik - Band 4/1 Abtragen & Beschichten*. Wien: Hanser Verlag, 1987.
- [31] U. Reisgen, S. Olschok, and S. Jakobs, "International Electron Beam Welding Conference," in *A comparison of electron beam welding with laser beam welding in vacuum*, 2012, pp. 119–127.
- [32] K. R. Schulze, "Immer dasselbe und doch jedes Mal anders," *DVS Schweißen und Schneiden*, vol. 7, no. Elektronenstrahlschweißen, pp. 392–397, 2011.
- [33] W. Plaßmann, D. Schulz, D. Conrads, H. Gierens, R. Von Liebenstein, A. Kemnitz, H. Steffen, G. Wellenreuther, and D. Zastrow, *Handbuch Elektrotechnik: Grundlagen und Anwendungen für Elektrotechniker*. Vieweg+Teubner Verlag, 2008.
- [34] ISO, "ÖNORM EN 1011-7 - Schweißen - Empfehlungen zum Schweißen metallischer Werkstoffe Teil 7: Elektronenstrahlschweißen." Wien, 2004.
- [35] ISO, "ÖNORM EN ISO 15609-3 - Anforderung und Qualifizierung von Schweißverfahren für metallische Werkstoffe- Schweißanweisung Teil 3: Elektronenstrahlschweißen." Wien, 2004.

- [36] G. Schubert, "Electron Beam Welding – Process , Applications and Equipment," *PTR-Precision Technologies Inc.* [Online]. Available: http://www.ptreb.com/Customer-Content/WWW/CMS/files/Electron_Beam_Welding_Process_Applications_and_Equipment.pdf. [Accessed: 28-Sep-2012].
- [37] D. Dobeneck v., T. Löwer, and V. Adam, *Elektronenstrahlschweißen - Das Verfahren und seine industrielle Anwendung für höchste Produktivität*. Burg, Germany: Verlag moderne Industrie, 2001.
- [38] U. Dilthey, A. Goumeniouk, S. Böhm, and T. Welters, "Electron beam diagnostics: a new release of the diabeam system," *Vacuum*, vol. 62, pp. 77–85, 2001.
- [39] axiaACT, "diaBEAM - Electron Beam Products," 2012. [Online]. Available: http://www.aixacct.com/html/prod/ebeamprods_diabeam.php. [Accessed: 12-Jan-2012].
- [40] U. Reisgen and S. Olschok, "Elektronenstrahlschweißen in Zwangspositionen," *DVS Schweißen und Schneiden*, vol. 7, pp. 365–373, 2011.
- [41] N. Olshanskii, *Movement of molten Metal during EB-Welding Welding Production - Band 23*, 2nd ed. Düsseldorf: DVS Media, 1974.
- [42] K. R. Schulze, "Durch dick und dünn - Elektronen strahlschweißen - Verfahren und Technologien," *Schweissen und Schneiden*, vol. 63, no. 6, pp. 320–325, 2011.
- [43] K. H. Steigerwald and D. König, "Neue Ergebnisse auf den Gebieten der Werkstoffbearbeitung und Behandlung mit Elektronenstrahlen," Düsseldorf, 1971.
- [44] DVS, "DVS Merkblatt 3201 - Grundsätze für das Konstruieren von Bauteilen für das Elektronenstrahlschweißen im Fein- und Hochvakuum DVS Merkblatt DVS." Düsseldorf, 2000.
- [45] U. Clauß, "International Electron Beam Welding Conference," in *Industrial electron beam applications*, 2012, pp. 10–13.
- [46] P. Fu, Z. Mao, W. Yu, S. Gong, and Z. Tang, "International Electron Beam Welding Conference," in *Microstructure and properties of simultaneous EBW and heat treatment with multi-pools for near α titanium alloy*, 2012, pp. 72–76.
- [47] K. Rührich and R. Zenker, "International Electron Beam Welding Conference," in *Characteristics and prospects of process integrated thermal field heat treatment for electron beam welding of cast iron*, 2012, pp. 83–87.
- [48] U. Reisgen, S. Olschok, A. Backhaus, M. Rethmeier, A. Gumenyuk, and F. Tölle, "International Electron Beam Welding Conference," in *Reduction of weld residual stresses with the electron beam*, 2012, pp. 128–132.
- [49] C. Börner, H. Pries, and K. Dilger, "International Electron Beam Welding Conference," in *Use of the multiple-focus technology for an influence on weld seam geometry and hot cracking of nickel-based super alloys*, 2012, pp. 77–82.
- [50] W. Behr, "Wettbewerbsfähige Lösungen für die Fügetechnik," *DVS-Aktuell: „Elektronenstrahlschweißen“*, 2009.
- [51] U. Dilthey, *Schweißtechnische Fertigungsverfahren 1 Schweiß- und Schneidtechnologien*, 3. Auflage. Berlin- Heidelberg: Springer Verlag, 2006, pp. 157–172.

- [52] Z. Sun and R. Karppi, "The application of electron beam welding for the joining of dissimilar metals: an overview," *Journal of Materials Processing Technology*, vol. 59, no. 3, pp. 257–267, May 1996.
- [53] K. Woeste, "Elektronenstrahlschweißen metallischer Werkstoffkombinationen," Reinisch-Westfälische Technische Hochschule Aachen, 2005.
- [54] W. Kleppmann, *Taschenbuch Versuchsplanung*, 4th ed., vol. 3. München, Wien: Hanser Verlag, 2003.
- [55] Minitab Inc, "Minitab Manual," *Quality*. Minitab inc, 2009.
- [56] Voestalpine Gießerei Traisen, "Werkstoffprüfung GX13CrMoCoVNbNB10-1-1." Traisen, 2009.
- [57] Verlag Stahlschlüssel Wegst GmbH, "Stahlschlüssel." Verlag Stahlschlüssel Wegst GmbH, Marbach, GER, 2010.
- [58] Voestalpine Gießerei Traisen, "Werkstoffdatenblatt NiCr22Mo9Nb; 2.4856." Traisen, 2007.
- [59] M. Stockinger, "Mikrostrukturelle Simulation des Gesenkschmiedens von Nickelbasis- Legierungen," Graz University of Technology, 2003.
- [60] T. Seliga, "Untersuchungen der Strukturstabilität von Ni-(Fe)-Basislegierungen für Rotorwellen in Dampfturbinen mit Arbeitstemperaturen über 700° C," *Schriften des Forschungszentrums Jülich, Reihe Energietechnik*, vol. 38, 2005.
- [61] ISO, "ÖNORM EN ISO 15614-1 - Anforderung und Qualifizierung von Schweißverfahren für metallische Werkstoffe - Schweißverfahrensprüfung." Wien, 2004.
- [62] ON Österreichisches Normungsinstitut, "Schweißen – Richtlinie für die Gruppeneinteilung von metallischen Werkstoffen (ISO/TR 15608:2005)." Wien, 2006.
- [63] ISO, "ÖNORM EN ISO 15614-11 - Anforderung und Qualifizierung von Schweißverfahren für metallische Werkstoffe - Schweißverfahrensprüfung Teil 11: Elektronen- und Laserstrahlschweißen," vol. 2002. Wien, 2002.
- [64] J. Goldstein, *Scanning Electron Microscopy and X-Ray Microanalysis*, 3rd ed. Springer Verlag, 2003.
- [65] University of California Riverside, "Introduction to Energy Dispersive X-ray Spectrometry (EDS)," 2013. [Online]. Available: <http://micron.ucr.edu/public/manuals/EDS-intro.pdf>. [Accessed: 29-Jan-2013].
- [66] ISO, "ÖNORM EN 1043-2 - Zerstörende Prüfung von Schweißverbindungen an metallischen Werkstoffen Härteprüfung Teil 2: Mikrohärtprüfung an Schweißverbindungen." Wien, 1996.
- [67] ISO, "ÖNORM EN 1043-1 - Zerstörende Prüfung an Schweißnähten an metallischen Werkstoffen; Härteprüfung Teil 1: Härteprüfung für Lichtbogenschweißverbindungen." Wien, 1996.
- [68] DIN, "DIN 50120 - Prüfung metallischer Werkstoffe - Zugproben." Berlin, 2004.
- [69] EN, "ÖNORM EN 10045-1 - Metallische Werkstoffe Kerbschlagbiegeversuch nach Charpy Prüfverfahren," no. 0222. Wien, 1991.
- [70] ISO, "ÖNORM EN 910 - Zerstörende Prüfungen von Schweißnähten an metallischen Werkstoffen; Biegeprüfung." Wien, 1996.
- [71] ISO, "EN ISO 5173 - Zerstörende Prüfung von Schweißverbindungen an metallischen Werkstoffen - Querzugversuch." Brüssel, 2009.

- [72] D. Loeber, "Modified Schöffler Diagramm." www.metallograph.de, 2013.
- [73] M. Cortial, J. M. Corrieu, and C. Vernot-Loier, "Influence of heat treatments on microstructure, mechanical properties, and corrosion resistance of weld alloy 625," *Metallurgical and Materials Transactions A*, vol. 26, no. 5, pp. 1273–1286, 1995.